OCT 21 1957

UNIVERSITY OF MICHIGAN
OCT 23 1957
PHYSICS LIBRARY

Journal of Research

of the

National Bureau of Standards

OCTOBER 1957

VOLUME 59 NUMBER 4

U. S. DEPARTMENT OF COMMERCE
Sinclair Weeks, Secretary
NATIONAL BUREAU OF STANDARDS
A. V. Astin, Director

OCTOBER • 19
VOLUME • 5
NUMBER • 4

JOURNAL OF RESEARCH

of the

NATIONAL BUREAU OF STANDARDS

The National Bureau of Standards

Functions and Activities

The functions of the National Bureau of Standards are set forth in the Act of Congress, March 3, 1901, as amended by Congress in Public Law 619, 1950. These include the development and maintenance of the national standards of measurement and the provision of means and methods for making measurements consistent with these standards; the determination of physical constants and properties of materials; the development of methods and instruments for testing materials, devices, and structures; advisory services to Government Agencies on scientific and technical problems; invention and development of devices to serve special needs of the Government; and the development of standard practices, codes, and specifications. The work includes basic and applied research, development, engineering, instrumentation, testing, evaluation, calibration services, and various consultation and information services. A major portion of the Bureau's work is performed for other Government Agencies, particularly the Department of Defense and the Atomic Energy Commission. The scope of activities is suggested by the listing of divisions and sections on the inside of the back cover.

Publications

The results of the Bureau's work take the form of either actual equipment and devices or published papers. These papers appear either in the Bureau's own series of publications or in the journals of professional and scientific societies. The Bureau itself publishes three monthly periodicals, available from the Government Printing Office: The Journal of Research, which presents complete papers reporting technical investigations; the Technical News Bulletin, which presents summary and preliminary reports on work in progress; and Basic Radio Propagation Predictions, which provides data for determining the best frequencies to use for radio communications throughout the world. There are also five series of nonperiodical publications: The Applied Mathematics Series, Circulars, Handbooks, Building Materials and Structures Reports, and Miscellaneous Publications.

Information on the Bureau's publications can be found in NBS Circular 460, Publications of the National Bureau of Standards ($1.25) and its Supplement ($0.75), available from the Superintendent of Documents, Government Printing Office, Washington 25, D. C.

Order all publications from the Superintendent of Documents
U. S. Government Printing Office, Washington 25, D. C.

Use of funds for printing this publication approved by the Director of the Bureau of the Budget (May 14, 1956)

Journal of Research of the National Bureau of Standards Vol. 59, No. 4, October 1957 Research Paper 2792

Formulas for Inverse Osculatory Interpolation in the Complex Plane

Herbert E. Salzer[1]

Improved formulas for inverse osculatory interpolation in the complex plane are obtained by inversion of Hermite's formula and the use of appropriate grid point configurations. They cover the cases for $n=2(1)7$, where n is the number of points required in direct osculatory interpolation. The formulas provide an improved means for inverse interpolation in the complex plane where the first derivative is either tabulated alongside the function or is easily obtained.

Formulas for n-point inverse osculatory interpolation for finding $x=x_0+ph$ from $f(x)$ in terms of $f_k \equiv f(x_k)$ and $f'_k \equiv f'(x_k)$, where the $x_k \equiv x_0+kh$, the k ranging from $-[(n-1)/2]$ to $[n/2]$, are equally spaced at intervals of h, have been obtained previously by the author [1][2] through the inversion of the Hermite osculatory interpolation formula [2,3]. Those formulas are still applicable to analytic functions when x is replaced by a complex variable $z=z_0+Ph$, and $z_k \equiv z_0+kh$ are equally spaced upon any line in the z-plane at interval h, which may be any suitably chosen complex number. But for many analytic functions that are given with their first derivatives over a Cartesian grid of length h in the complex plane (so that now h is a positive number), the accuracy of inverse osculatory interpolation is considerably greater when the points z_k are chosen as grid points that lie much closer to each other, no longer in a straight line beyond the 2-point case.

Improved formulas for inverse osculatory interpolation, which utilize the Cartesian grid, will be particularly useful in connection with such tables for complex arguments as (1) $\log \Gamma(z)$, together with its derivative the psi function, (2) Bessel functions of the first or second kind giving $J_0(z)$ and $J_1(z)=-J'_0(z)$, $Y_0(z)$ and $Y_1(z)=-Y'_0(z)$, or linear combinations of them, (3) probability integral $\int_0^z e^{-u^2}du$ with its integrand e^{-z^2} [4,8], (4) miscellaneous tables of integrals of the more elementary functions where the first derivative or the integrand, although not tabulated, is easy to calculate, viz., the function $\int_z^\infty (e^{-u}/u)du$ [5], and (5) tables of solutions of important linear differential equations, together with the first derivative [6]. In all such tables and in many others, the user will find the inverse interpolation formulas that are given below to be particularly convenient, especially in those cases where grid length h is too large for sufficiently accurate complex inverse interpolation, using the formulas in terms of only the functional values f_i [7].

In accordance with the choice of grid points that has been employed consistently in earlier papers of the author on complex interpolation, for n ranging from 2 to 7, the n-point formulas in this present article are based upon the values of $f(z_k)$ and $f'(z_k)$ for z_k in the following configurations:

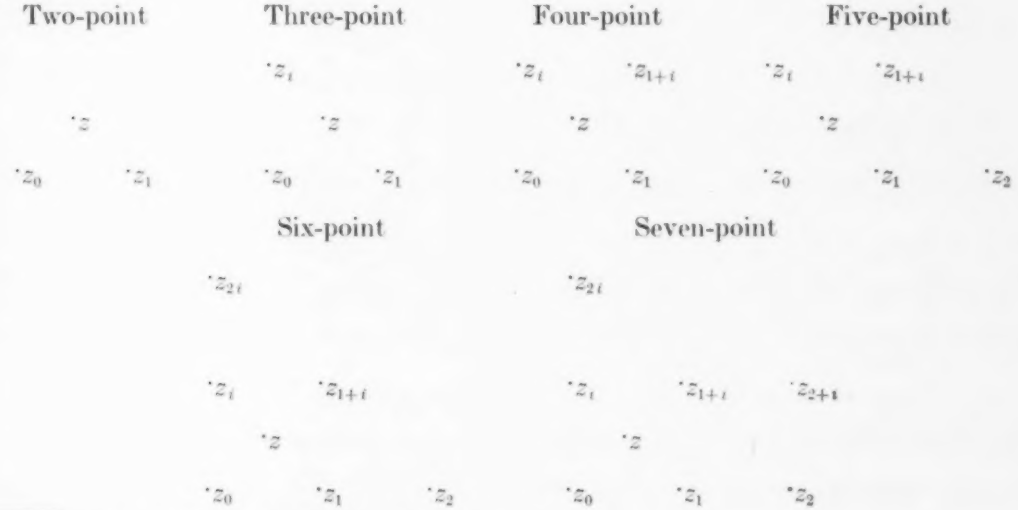

[1] Present address, Convair Astronautics, San Diego, Calif.
[2] Figures in brackets indicate the literature references at the end of this paper.

These formulas enable one to find $z=z_0+Ph$ by expressing P in terms of $f(z_0+Ph)\equiv f$, $f(z_k)\equiv f_k$, and $f'(z_k)\equiv f'_k$, for $z_k\equiv z_0+kh$, where k ranges over the points of the selected n-point configuration, the choice of n depending upon the number of points required in direct osculatory interpolation. Although the direct interpolation formula for $n=6$ and $n=7$ is of the 11th- and 13th-degree accuracy, respectively, (recalling that the n-point direct osculatory interpolation formula is of $(2n-1)$th-degree accuracy), the inversion formula for P given below does not go beyond the 10th-degree terms. In fact, most practical problems will require only the first few terms, and it is very rarely that one would need this inversion series up to the 10th-degree terms. Thus in this paper we do not use the coefficient of P^{11} in the 6-point Hermite formula, nor the coefficient of P^{11}, P^{12}, and P^{13} in the 7-point Hermite formula.

For every n we define $r=(f-f_0)/hf'_0$, and corresponding to each of the above n-point configurations, where $n=2(1)7$, quantities s, t, u, v, w, x, y, z, and $\bar{z}$ are defined as follows:

Two-point

$$s=(-3\{f_0-f_1\}-h\{2f'_0+f'_1\})/hf'_0,$$

$$t=(2\{f_0-f_1\}+h\{f'_0+f'_1\})/hf'_0,$$

$$u=v=w=x=y=z=\bar{z}=0.$$

Three-point

$$s=\tfrac{1}{2}(8if_0+(1-4i)f_1-(1+4i)f_i+h\{-(4-4i)f'_0+if'_1-f'_i\})/hf'_0,$$

$$t=\tfrac{1}{2}(-(12+12i)f_0+(7+5i)f_1+(5+7i)f_i+h\{-8if'_0-(2+i)f'_1+(2-i)f'_i\})/hf'_0,$$

$$u=\tfrac{1}{2}(14f_0-(7-2i)f_1-(7+2i)f_i+h\{(4+4i)f'_0+(2-i)f'_1-(1-2i)f'_i\})/hf'_0,$$

$$v=\tfrac{1}{2}(-(4-4i)f_0+(1-3i)f_1+(3-i)f_i+h\{-2f'_0+if'_1-if'_i\})/hf'_0,$$

$$w=x=y=z=\bar{z}=0.$$

Four-point

$$s=\tfrac{1}{2}(19if_0-(8+6i)f_1+(8-6i)f_i-7if_{1+i}+h\{-(6-6i)f'_0+2f'_1-2if'_i-(1-i)f'_{1+i}\})/hf'_0,$$

$$t=\tfrac{1}{2}(-(37+37i)f_0+(32-12i)f_1-(12-32i)f_i+(17+17i)f_{1+i}+h\{-17if'_0-(4-6i)f'_1+(4+6i)f'_i$$
$$-5if'_{1+i}\})/hf'_0,$$

$$u=\tfrac{1}{2}(70f_0-(15-50i)f_1-(15+50i)f_i-40f_{1+i}+h\{(14+14i)f'_0-(4+11i)f'_1-(11+4i)f'_i$$
$$+(6+6i)f'_{1+i}\})/hf'_0,$$

$$v=\tfrac{1}{2}(-(38-38i)f_0-(25+37i)f_1+(37+25i)f_i+(26-26i)f_{1+i}+h\{-14f'_0+(10+3i)f'_1$$
$$+(10-3i)f'_i-8f'_{1+i}\})/hf'_0,$$

$$w=\tfrac{1}{2}(-23if_0+(21+2i)f_1-(21-2i)f_i+19if_{1+i}+h\{(4-4i)f'_0-(4-3i)f'_1-(3-4i)f'_i$$
$$+(3-3i)f'_{1+i}\})/hf'_0,$$

$$x=\tfrac{1}{2}((3+3i)f_0-(3-3i)f_1+(3-3i)f_i-(3+3i)f_{1+i}+h\{if'_0-if'_1-if'_i+if'_{1+i}\})/hf'_0,$$

$$y=z=\bar{z}=0.$$

Five-point

$$s=(\tfrac{1}{300}\{-(1875-6250i)f_0-(4000+6000i)f_1+(103+254i)f_2+(2272+496i)f_i$$
$$+(3500-1000i)f_{1+i}\}+\tfrac{h}{300}\{-(200-150i)f'_0+200f'_1-(3+4i)f'_2+(32-24i)f'_i$$
$$-(50+50i)f'_{1+i}\})/hf'_0,$$

$$t=(\tfrac{1}{1000}\{-(1525+3950i)f_0+(5600+1200i)f_1-(223+114i)f_2-(1952-464i)f_i$$
$$-(1900-2400i)f_{1+i}\}+\tfrac{h}{200}\{(65-230i)f'_0-(240-240i)f'_1+(9+2i)f'_2-(32-64i)f'_i$$
$$+(120+20i)f'_{1+i}\})/hf'_0,$$

$$u=(\tfrac{1}{10000}\{(59750+37125i)f_0-(96000-53000i)f_1+(5284-1313i)f_2+(29216-26312i)f_i$$
$$+(1750-62500i)f_{1+i}\}+\tfrac{h}{1000}\{(625+1625i)f'_0+(100-3400i)f'_1-(89-48i)f'_2-(24+732i)f'_i$$
$$-(1125-575i)f'_{1+i}\})/hf'_0,$$

$$v=(\tfrac{1}{10000}\{-(72625-5250i)f_0+(48000-118000i)f_1-(4103-5746i)f_2-(14272-43504i)f_i$$
$$+(43000+63500i)f_{1+i}\}+\tfrac{h}{2000}\{-(2800+1825i)f'_0+(5200+6200i)f'_1+(96-247i)f'_2$$
$$+(896+1528i)f'_i+(1450-2800i)f'_{1+i}\})/hf'_0,$$

$$w=(\tfrac{1}{1000}\{(3850-3075i)f_0+(2450+9200i)f_1-(42+581i)f_2-(658+3344i)f_i-(5600+2200i)f_{1+i}\}$$
$$+\tfrac{h}{200}\{(215-5i)f'_0-(600+110i)f'_1+(7+21i)f'_2-(114+72i)f'_i+(30+250i)f'_{1+i}\})/hf'_0,$$

$$x=(\tfrac{1}{5000}\{-(3500-10125i)f_0-(17250+14750i)f_1+(1022+1121i)f_2+(4978+6254i)f_i$$
$$+(14750-2750i)f_{1+i}\}+\tfrac{h}{1000}\{-(375-250i)f'_0+(1300-650i)f'_1-(49+32i)f'_2+(316+38i)f'_i$$
$$-(400+500i)f'_{1+i}\})/hf'_0,$$

$$y=(\tfrac{1}{10000}\{-(1000+5375i)f_0+(12500+2000i)f_1-(898+189i)f_2-(3852+1936i)f_i$$
$$-(6750-5500i)f_{1+i}\}+\tfrac{h}{1000}\{(50-100i)f'_0-(200-350i)f'_1+(18-i)f'_2-(82-24i)f'_i$$
$$+(175+75i)f'_{1+i}\})/hf'_0,$$

$$z=(\tfrac{1}{10000}\{(375+500i)f_0-(1500-500i)f_1+(117-44i)f_2+(508+44i)f_i+(500-1000i)f_{1+i}\}$$
$$+\tfrac{h}{2000}\{25if'_0-100if'_1-(4-3i)f'_2+(16-12i)f'_i-50f'_{1+i}\})/hf'_0,$$

$\overline{z}=0.$

Six-point

$$s=(\tfrac{1}{10000}\{16500if_0-(14336+1152i)f_1+(289-98i)f_2+(14336-1152i)f_i-14000if_{1+i}$$
$$-(289+98i)f_{2i}\}+\tfrac{h}{1000}\{-(400-400i)f'_0+(192-256i)f'_1-(4-3i)f'_2+(256-192i)f'_i$$
$$-(200-200i)f'_{1+i}-(3-4i)f'_{2i}\})/hf'_0,$$

$$t=(\tfrac{1}{20000}\{-(86500+86500i)f_0+(91392-102656i)f_1-(1219-2983i)f_2-(102656-91392i)f_i$$
$$+(96000+96000i)f_{1+i}+(2983-1219i)f_{2i}\}+\tfrac{h}{2000}\{-3100if'_0+(896+3072i)f'_1+(4-53i)f'_2$$
$$-(896-3072i)f'_i-2800if'_{1+i}-(4+53i)f'_{2i}\})/hf'_0,$$

$$u=(\tfrac{1}{8000}\{95150f_0+(18688+124416i)f_1-(1463+2934i)f_2+(18688-124416i)f_i-129600f_{1+i}$$
$$-(1463-2934i)f_{2i}\}+\tfrac{h}{800}\{(1500+1500i)f'_0-(2816+1152i)f'_1+(38+39i)f'_2-(1152+2816i)f'_i$$
$$+(1920+1920i)f'_{1+i}+(39+38i)f'_{2i}\})/hf'_0,$$

$$v=(\tfrac{1}{16000}\{-(169500-169500i)f_0-(301824+192768i)f_1+(9957+2601i)f_2+(192768+301824i)f_i$$
$$+(271200-271200i)f_{1+i}-(2601+9957i)f_{2i}\}+\tfrac{h}{1600}\{-4970f'_0+(7808-4224i)f'_1-(172-9i)f'_2$$
$$+(7808+4224i)f'_i-8160f'_{1+i}-(172+9i)f'_{2i}\})/hf'_0,$$

$$w=(\tfrac{1}{8000}\{-1047750if_0+(1662976-466368i)f_1-(44774-30743i)f_2-(1662976+466368i)f_i$$
$$+1919000if_{1+i}+(44774+30743i)f_{2i}\}+\tfrac{h}{8000}\{(14650-14650i)f'_0-(8672-42496i)f'_1$$
$$+(564-723i)f'_2-(42496-8672i)f'_i+(29300-29300i)f'_{1+i}+(723-564i)f'_{2i}\})/hf'_0,$$
$$x=(\tfrac{1}{16000}\{(919000+919000i)f_0-(1038592-2080256i)f_1+(8369-79033i)f_2$$
$$+(2080256-1038592i)f_i-(1890000+1890000i)f_{1+i}-(79033-8369i)f_{2i}\}+\tfrac{h}{16000}\{24850if'_0$$
$$-(36096+46272i)f'_1+(271+1328i)f'_2+(36096-46272i)f'_i+58600if'_{1+i}$$
$$-(271-1328i)f'_{2i}\})/hf'_0,$$
$$y=(\tfrac{1}{8000}\{-28450f_0-(19568+50976i)f_1+(1393+1449i)f_2-(19568-50976i)f_i+64800f_{1+i}$$
$$+(1393-1449i)f_{2i}\}+\tfrac{h}{1600}\{-(750+750i)f'_0+(2752+144i)f'_1-(61+33i)f'_2+(144+2752i)f'_i$$
$$-(2040+2040i)f'_{1+i}-(33+61i)f'_{2i}\})/hf'_0,$$
$$z=(\tfrac{1}{16000}\{(12000-12000i)f_0+(32224+12768i)f_1-(1357-99i)f_2-(12768+32224i)f_i$$
$$-(30000-30000i)f_{1+i}-(99-1357i)f_{2i}\}+\tfrac{h}{1600}\{310f'_0-(608-624i)f'_1+(22-9i)f'_2$$
$$-(608+624i)f'_i+960f'_{1+i}+(22+9i)f'_{2i}\})/hf'_0,$$
$$\overline{z}=(\tfrac{1}{8000}\{15750if_0-(30688-14784i)f_1+(812-1159i)f_2+(30688+14784i)f_i-43000if_{1+i}$$
$$-(812+1159i)f_{2i}\}+\tfrac{h}{8000}\{-(200-200i)f'_0-(64+848i)f'_1-(7-24i)f'_2+(848+64i)f'_i$$
$$-(700-700i)f'_{1+i}-(24-7i)f'_{2i}\})/hf'_0.$$

Seven-point

$$s=(\tfrac{1}{10000}\{-(1960-21780i)f_0-(38400-11200i)f_1-(1119+1342i)f_2+(15744+14592i)f_i$$
$$+(28000-46000i)f_{1+i}-(2432-64i)f_{2+i}+(167-294i)f_{2i}\}+\tfrac{h}{1000}\{-(480-440i)f'_0$$
$$-800if'_1+(24+7i)f'_2+(384+112i)f'_i-(1400+200i)f'_{1+i}+(32+16i)f'_{2+i}-(3+4i)f'_{2i}\})/hf'_0,$$
$$t=(\tfrac{1}{20000}\{-(113316+147012i)f_0+(193280-407040i)f_1+(21313+1659i)f_2-(242688+30784i)f_i$$
$$+(120000+600000i)f_{1+i}+(20736-20928i)f_{2+i}+(675+4105i)f_{2i}\}+\tfrac{h}{2000}\{(344-4092i)f'_0$$
$$+(7040+6080i)f'_1-(268-151i)f'_2-(4448-1536i)f'_i+(13600-9200i)f'_{1+i}-(416-128i)f'_{2+i}$$
$$+(60+15i)f'_{2i}\})/hf'_0,$$
$$u=(\tfrac{1}{40000}\{(825894+140208i)f_0+(898176+2284032i)f_1-(94875-83250i)f_2$$
$$+(1152000-672000i)f_i-(2760000+1992000i)f_{1+i}-(2688-172800i)f_{2+i}$$
$$-(18507+16290i)f_{2i}\}+\tfrac{h}{4000}\{(10044+12908i)f'_0-(51392-6656i)f'_1+(470-1765i)f'_2$$
$$+(14880-21760i)f'_i-(21600-90400i)f'_{1+i}+(1248-2240i)f'_{2+i}-(333-158i)f'_{2i}\})/hf'_0,$$
$$v=(\tfrac{1}{80000}\{-(2094204-1361372i)f_0-(7780992+3228544i)f_1+(24441-466387i)f_2$$
$$-(1650816-4256512i)f_i+(11844000-1460000i)f_{1+i}-(433920+466304i)f_{2+i}$$
$$+(91491+3351i)f_{2i}\}+\tfrac{h}{8000}\{-(44834+7488i)f'_0+(103744-147392i)f'_1+(3484+5837i)f'_2$$
$$+(4704+91872i)f'_i-(160800+289600i)f'_{1+i}+(2400+9184i)f'_{2+i}+(588-1245i)f'_{2i}\})/hf'_0,$$

$$w=(\tfrac{1}{8000}\{(662260-2573430i)f_0+(9236480-3900640i)f_1+(404714+437677i)f_2$$
$$-(1662464+5151552i)f_i-(9358000-11071000i)f_{1+i}+(810752+46496i)f_{2+i}$$
$$-(93742-70449i)f_{2i}\}+\tfrac{h}{8000}\{(38730-25190i)f_0'+(43840+211280i)f_1'-(8494+2017i)f_2'$$
$$-(71904+83672i)f_i'+(387500+130100i)f_{1+i}'-(10352+6376i)f_{2+i}'+(423+1724i)f_{2i}'\})/hf_0',$$
$$x=(\tfrac{1}{16000}\{(1955376+3684432i)f_0-(6505920-15994560i)f_1-(1095693+27999i)f_2$$
$$+(7805568+5022624i)f_i-(1074000+25434000i)f_{1+i}-(1139136-969888i)f_{2+i}$$
$$+(53805-209505i)f_{2i}\}+\tfrac{h}{16000}\{-(17684-67962i)f_0'-(315360+197120i)f_1'$$
$$+(13623-8686i)f_2'+(186528+37104i)f_i'-(667600-293000i)f_{1+i}'+(22016-4688i)f_{2+i}'$$
$$-(2615+2010i)f_{2i}'\})/hf_0',$$
$$y=(\tfrac{1}{8000}\{-(1149156+414642i)f_0-(2086704+5056128i)f_1+(264015-257730i)f_2$$
$$-(2906640-342480i)f_i+(5796000+5823000i)f_{1+i}+(52992-503760i)f_{2+i}$$
$$+(29493+66780i)f_{2i}\}+\tfrac{h}{8000}\{-(9306+17792i)f_0'+(114168-27824i)f_1'-(1095-5365i)f_2'$$
$$-(53460-27320i)f_i'+(98100-217900i)f_{1+i}'-(4332-6320i)f_{2+i}'+(1122-12i)f_{2i}'\})/hf_0',$$
$$z=(\tfrac{1}{16000}\{(985056-400808i)f_0+(4675648+2023936i)f_1+(221+363403i)f_2$$
$$+(1877904-1958528i)f_i-(7782000+394000i)f_{1+i}+(306480+400256i)f_{2+i}$$
$$-(63309+34259i)f_{2i}\}+\tfrac{h}{16000}\{(16076+5982i)f_0'-(56336-93248i)f_1'-(3071+4478i)f_2'$$
$$+(23024-50568i)f_i'+(69600+219400i)f_{1+i}'-(1200+7576i)f_{2+i}'-(877-690i)f_{2i}'\})/hf_0',$$
$$\bar{z}=(\tfrac{1}{8000}\{-(74180-150990i)f_0-(802080-297440i)f_1-(45912+44891i)f_2-(35088-452016i)f_i$$
$$+(1034000-839000i)f_{1+i}-(89296+14608i)f_{2+i}+(12556-1947i)f_{2i}\}+\tfrac{h}{8000}\{-(2490-970i)f_0'$$
$$-(4240+17680i)f_1'+(952+161i)f_2'+(2232+8976i)f_i'-(34300+20500i)f_{1+i}'+(1096+848i)f_{2+i}'$$
$$+(51-192i)f_{2i}'\})/hf_0'.$$

For every n, P is given by the following formula:

$$P=r-r^2s+r^3(2s^2-t)+r^4(-5s^3+5st-u)+r^5(14s^4-21s^2t+3t^2+6su-v)+r^6(-42s^5+84s^3t-28st^2$$
$$-28s^2u+7tu+7sv-w)+r^7(132s^6-330s^4t+180s^2t^2+120s^3u-12t^3-72stu-36s^2v+4u^2+8tv$$
$$+8sw-x)+r^8(-429s^7+1287s^5t-990s^3t^2-495s^4u+495s^2tu+165st^3+165s^3v-45t^2u-45su^2$$
$$-90stv-45s^2w+9uv+9tw+9sx-y)+r^9(1430s^8-5005s^6t+5005s^4t^2+2002s^5u-1430s^2t^3$$
$$-2860s^3tu-715s^4v+55t^4+660st^2u+330s^2u^2+660s^2tv+220s^3w-55tu^2-55t^2v-110suv$$
$$-110stw-55s^2x+5v^2+10uw+10tx+10sy-z)+r^{10}(-4862s^9+19448s^7t-24024s^5t^2-8008s^6u$$
$$+10010s^3t^3+15015s^4tu+3003s^5v-1001st^4-6006s^2t^2u-2002s^3u^2-4004s^3tv-1001s^4w$$
$$+286t^3u+858stu^2+858s^2tw+858st^2v+858s^2uv+286s^3x-22u^3-132tuv-66t^2w-66sv^2$$
$$-132suw-132stx-66s^2y+11vw+11ux+11ty+11sz-\bar{z})+\ldots.$$

[1] H. E. Salzer, Formulas for inverse osculatory interpolation, J. Research NBS **56**, 51 (1956) RP2647.
[2] T. Fort, Finite differences, p. 85 (Clarendon Press, Oxford, England, 1948).
[3] J. F. Steffensen, Interpolation, p. 33 (Williams & Wilkins, Baltimore, Md., 1927).
[4] V. N. Faddeeva and N. M. Terent'ev, Tables of values of the function $w(z)=e^{-z^2}(1+(2i/\sqrt{\pi})\int_0^z e^{t^2}dt)$ for complex arguments (Gosudarstv. Izdat. Tehn.-Teor. Lit., Moscow, 1954).
[5] National Bureau of Standards, Tables of exponential integrals for complex arguments (in preparation).
[6] Harvard Computation Laboratory, Tables of the modified Hankel functions of order one-third and of their derivatives (Harvard University Press, Cambridge, Mass., 1945).
[7] H. E. Salzer, Coefficients for complex quartic, quintic, and sextic interpolation within a square grid, J. Math. Phys. **27**, 138 (1948).
[8] K. A. Karpov, Tables of the function $w(z)=e^{-z^2}\int_0^z e^{x^2}dx$ in complex regions (M., Izdat. AN SSSR, Moscow, 1954).

WASHINGTON, February 7, 1957.

Journal of Research of the National Bureau of Standards Vol. 59, No. 4, October 1957 Research Paper 2793

An X-ray Study of Textural Stresses in Two-Phase Alloys

C. J. Newton and H. C. Vacher

Internal or residual stresses of the textural stress class are discussed, with special attention to that type resulting from a difference in thermal expansion of two phases present in an alloy. X-ray stress measurements were made on various brasses and steels, and the results were found to be in reasonable agreement with the quantitative theory of F. László.

1. Introduction

The term "textural stress" will be used in this study in the sense adopted by E. Orowan in a symposium of the Institute of Metals in 1948 [1].[1] His most inclusive term, internal stress, is defined to be a stress existing in a body upon which no external force is acting. (Some writers use the term "residual stress" in this wide sense.) This field is divided into two classes. One class consists of body stresses, which arise when an external factor has affected different macroscopic parts of a body differently, even though the material of the body may have been quite homogeneous. The other class consists of textural stresses, which result from inhomogeneities of the material, even though the activating external influence may have itself been homogeneous. Under ordinary circumstances, where the grain size is small compared to the macroscopic dimensions of the body, these classes are closely equivalent to the widely used terms, macrostress and microstress, respectively. The former implies a stress system constant over many contiguous grains in a body, balanced by opposing stresses in other grains at some distance; the latter implies a stress system that varies from grain to grain or within a grain, and is balanced over short ranges.

The most detailed and quantitative theoretical analysis of textural stresses arising from the presence of two phases in an alloy is to be found in a series of four articles between 1943 and 1945 by F. László [2]. The four articles were reviewed in a nonmathematical manner by F. R. N. Nabarro in 1948 [3].

László discussed textural stresses arising from various sources, such as anisotropy of the grains and differences in thermal or mechanical properties, and the effect of external stress on the textural stress. Much numerical detail was presented with regard to iron alloys. The greater part of the work dealt with an involved mathematical analysis of textural stresses caused by the difference of coefficients of thermal expansion of two phases present in various proportions, and with various grain shapes. The solution was only approximate, of course, because of the simplifications that were necessarily made. In particular, three types of idealized grain shapes were assumed: Lamellar, with alternating layers of the two constituents, and compound spheres and compound cylinders, with coverings and cores of the two different phases. These compound blocks were assumed to have surfaces free of normal stress and to pack together to form the body of material, although strictly speaking only prismatic or polyhedral shapes could do so. The formulas for the approximate values of the principal stresses in these units presented in part I were used in this study. In Lász'ó's article, part II, the ideas were extended to other special cases, such as capped cylinders, and the physical rigor was somewhat enhanced; but the results there were presented in the form of systems of simultaneous equations of high order, and the value of the much more difficult solutions of these equations was questionable in the light of the experimental margin of error anticipated in the study at hand.

László suggested four technological effects in which such textural stresses might be of importance. Yield, the formation of cracks, fatigue, and corrosion, the last three of which are most likely to be significantly influenced by such stresses. Although the mathematical erudition and the extensive calculations from theory displayed in these articles were very impressive, no attempt at verification by X-ray measurements was made. On the contrary, it was specifically stated by László, in part I, that these stresses could not be revealed by X-ray diffraction. In spite of this opinion, one might observe some stress with X-rays for the following reasons: X-ray diffraction is a highly selective process, one aspect of which is the sorting out of diffractions from crystals of the different phases at different Bragg angles. An averaging of the triaxial stress state over many grains of one phase within the material would result in a pseudohydrostatic stress. The relaxation of the component normal to a free surface, however, would result in a biaxial state of stress, the average value of which would be measurable by the two-exposure X-ray method described later. Even if the sensitivity of this method, which depends on the observation of very small shifts in the diffraction line, were not sufficiently high for application, thermally induced textural stresses might be indicated by line broadening. In fact, broadening from this source was observed in a qualitative degree with duplex aluminum-silicon alloys by J. P. Nielsen and W. R. Hibbard in 1950 [4].

If the experimental technique is skillful enough, however, actual net shifts of the line can be measured; such methods have been used by several investigators to study textural stresses due to differences in mechanical properties of two phases in plastically

[1] Figures in brackets indicate the literature references at the end of this paper.

deformed specimens. One of the earliest of these was D. V. Wilson [5], who in 1950 attempted measurements on the ferrite and cementite constituents in 1.26 percent carbon steel compressed 90 percent. Although his sensitivity of measurement of the cementite lines was very poor, he found a definite indication of opposing stresses in the two phases. In 1955 L. Reimer [6] published the results of work with iron and steel specimens deformed plastically by bending. He showed the influence of textural constraints between the ferrite matrix and imbedded cementite. There was some indication that the residual stresses were proportional to carbon content by volume. In the same year, V. Hauk [7] made a study of plastically extended specimens of some two-phase alloys, not only steel but also a copper-aluminum alloy. He observed that not only an orientation dependence, but also the difference in elastic limits of the matrix and the intermetallic phase, contributed to the resulting stress system.

In view of the success in detecting by X-ray diffraction textural stresses arising, as above, from differences in mechanical constants in plastically deformed two-phase alloy specimens, it appeared worthwhile to investigate the possibility of observing, in annealed specimens, thermally induced textural stresses arising from differences of coefficients of thermal expansion. It has been previously observed at the X-ray metallographic laboratory of the Bureau that textural stresses are not completely relaxed by sectioning procedures [8]. For this reason it was hoped that the usual method of X-ray stress analysis on a free surface would permit detection of the strain resulting from a biaxial stress condition in the surface, which was set up when the quasi-hydrostatic system of textural stresses in the two phases was sectioned. This is to say that, rather than the qualitative and somewhat ambiguous line broadening observed by some, the effect to be looked for was a small but definite line shift, which would indicate a nonzero net change in the lattice parameter of a given phase. The materials chosen were a two-phase brass and a 1.05 percent carbon steel.

2. Stresses in Brasses

Two types of brass were studied; one was a two-phase alpha beta brass, and the other was a single-phase alpha brass. By adding a sufficient amount of zinc to molten cartridge brass, a two-phase alloy was produced, containing 58 percent of copper and 42 percent of zinc. This alloy consisted of approximately equal volumes of the alpha and the beta phases.

After a procedure of heating and rolling, small pieces of the proper size for mounting were cut from this material, and a heat treatment to give an apparent optimum combination of small grain size and minimum of preferred orientation of grains was determined. This was found to be ½ hr at 900° F in air, followed by cooling in the furnace tube removed from the heating coils.

The single-phase alpha brass material, cartridge brass, contained 70 percent of copper and 30 percent of zinc. The absence of the beta phase was confirmed by metallographic examination and X-ray diffraction. An optimum annealing condition for this material, 800° F for ½ hr, was similarly determined.

The technique employed for finishing the surface on the brass specimens consisted of many cycles of alternate mechanical polishing and electropolishing, ending with the latter. The progress of the procedure was followed by the growing sharpness of the diffraction spots on stationary X-ray patterns.

The diffraction patterns were made with X-rays from a cobalt target in the usual manner of the high-angle, or back-reflection, powder technique. To correct for changes of dimensions of the film and to provide a precise value for the specimen-to-film distance, a calibration ring, caused by diffraction from aluminum powder, was put on the film. The Bragg angle for alpha brass, using the (400) diffraction, was about 75°, and for beta brass, using the (310) diffraction, it was about 73°. Two patterns were made with each specimen, one with the X-ray beam normal to the surface of the specimen, and one with the beam making an angle of 30° with the normal. Only the second side emulsion was developed on each film, which resulted in sharper lines and greater contrast than is ordinarily obtained.

Measurements of the patterns were made with a modified traveling microscope calibrated to the order of 0.001 mm by the Shops Division of the National Bureau of Standards. The $K\alpha_1$ and $K\alpha_2$ lines were, in all cases, resolved, and in most cases readings were made on each. Two complete sets of data were taken independently by two different observers, with results in good agreement. Simple precision analysis of the data indicated that the probable error in the average of each setting was less than $\frac{1}{100}$ mm, which, in a typical case, would correspond to 0.00008 A in d-spacing.

From the radii of the diffraction rings and the known Bragg angle of diffraction for the calibration powder, it was possible to calculate the cosine of the complement of the Bragg angle of diffraction from the specimen. From this and the known value of the X-ray wavelength, the lattice spacing was calculated by Bragg's Law. The two values of lattice spacing and the polycrystalline elastic constants enabled one then to calculate the stress by means of the well-known formula:

$$\sigma=\frac{E}{1+\nu}\cdot\frac{1}{\sin^2\psi}\cdot\frac{d_\psi-d_\perp}{d_\perp},$$

where E is Young's modulus, ν is Poisson's ratio, ψ is the angle between the surface normal and the diffraction plane normal, and the d's are the lattice spacings [9].

In connection with this formula, some investigators have found that the ordinary mechanical values of Young's modulus and Poisson's ratio were satisfactory [10]. However, since the values for beta brass were not well established, it was decided to calculate these parameters for the alpha and beta phases from the fundamental single crystal elastic constants [11] by one of the polycrystalline aggre-

gate-averaging procedures. The three principal procedures were discussed in 1955 by H. H. Stadelmaier [12]. One formula, by A. Reuss, is based upon the simplifying assumption of equal stress in all grains; one by W. Voigt assumes equal strains in all grains. Of these two, the former has perhaps been used more, but G. B. Greenough [13] found that an average of the two results was preferable in his X-ray stress measurements. The averaging procedure of A. Huber and E. Schmid [14] makes no assumption except that all grains behave as if they have equal elastic moduli. This procedure, though in best agreement with observed moduli, is seldom used, perhaps because the answer does not proceed from a simple formula but from the numerical evaluation of the leading terms in an infinite series, representing the numerical solution of an integral. Nevertheless, it was this procedure that was used to obtain the values employed in these calculations. These values were, for alpha brass, $E=14.5\times10^6$ lb/in.^{2} and $\nu=0.43$; and for beta brass, $E=9.95\times10^6$ lb/in.^{2} and $\nu=0.29$.

The observed relative lattice changes, $\eta=(d_{\downarrow}-d_{\perp})/d_{\perp}$, and the calculated values of the stresses, σ, are presented in table 1. A positive sign indicates tension and a negative sign indicates compression. This table also shows the probable error in the stress measurement and the theoretical values of the stress calculated for the two-phase brass with the formulas derived by László.

TABLE 1. *Stresses in brass*

Specimen	Alpha brass		Beta brass	
	η	σ	η	σ
		lb/in.^{2}		*lb/in.*^{2}
Two-phase	-2.58×10^{-4}	-5.27×10^3	4.47×10^{-4}	6.53×10^3
Single-phase	-1.39	-2.83	.....	.....
	Theoretical values of stress			
Two-phase	.....	-4.33	.....	5.33

Precision in experimental σ about $\pm3.2\times10^3$ lb/in.^{2}

The value shown for probable error was based upon two sources, an uncertainty in the average of the settings of the traveling microscope on the lines of the pattern of $\pm1\times10^{-2}$ mm, and an estimated uncertainty of the temperature of $\pm3°$ C during each of the two exposures. These estimations were probably somewhat greater than was actually the case. They contributed the same order of magnitude of error, and, when they were combined, the total estimated probable error in stress was $\pm3.2\times10^3$ lb/in.^{2} This is in the neighborhood of the precision ordinarily claimed in X-ray stress measurements. Although the actual error was probably not quite this large, one could not expect great precision because the Bragg angles of diffraction for both brasses were less than 76°.

The theoretical stress values were computed with the aid of the formulas in the first paper of László previously referred to. It is to be expected that the stress revealed by the measurement of lattice spacings in the randomly distributed crystals of the aggregate would be proportional to the cubic dilatation of the grains. If k is the modulus of compression, or bulk modulus, and p is the effective hydrostatic pressure, the cubic dilatation is

$$\Delta=-p/k.$$

But p is related to Θ, the first stress invariant, by

$$p=-\Theta/3,$$

where

$$\Theta=\sigma_1+\sigma_2+\sigma_3,$$

where σ_1, σ_2, and σ_3 are the principal stresses. Therefore

$$\Delta=-(-\Theta/3)/k$$

$$=(1/k)\cdot(\sigma_1+\sigma_2+\sigma_3)/3.$$

That is to say, the dilatation is proportional to the average of the three principal stresses. Therefore, it was this average stress, as calculated from László's formulas and multiplied by a surface relaxation factor, that was compared with the observed value. The relaxation factor referred to is 1 minus Poisson's ratio, according to László, equaling, in most cases, approximately 0.7, which corrects for the increase in stress components in the surface when the normal component is reduced to zero.

The coefficients of linear thermal expansion used in the calculations were, for alpha brass, 22.4×10^{-6}/°C, and for beta brass, 24.7×10^{-6}/°C. These values were calculated from data published by P. D. Merica and L. W. Schad [15]. The temperature change was 455° C. It can be seen in the table that the results of the calculations of stress in the two-phase alloy were well within the experimental margin of error of the observed X-ray stress values, with the beta brass, having the larger coefficient, in tension, and the alpha brass, having the smaller coefficient, in compression.

The value of stress measured for alpha brass was somewhat closer to zero than the estimated probable error, but the authors felt that, since it was carefully checked by both remeasurement and reannealing, this stress was at least qualitatively real. Although no definite second phase with a specifically differing thermal expansion coefficient was present, some thermal stresses could theoretically be caused by small amounts of disordered material of different thermal properties present at or near grain boundaries. It is possible, also, that some small degree of surface preparation distortion might still have been present, thus contributing to the nonzero result.

3. Stresses in Steels

The material from which the steel specimens were prepared contained 1.05 percent carbon, with minor constituents totaling 0.74 percent. Three specimens were prepared with different heat treatments in such a manner that one showed a structure of fine lamellar pearlite, one had a spheroidized structure, and one was decarburized. The decarburized specimen, containing a minute amount of cementite to assure saturation of the ferrite with carbon, was included to provide a specimen of an essentially single-phase alloy having the same composition as the ferrite in the pearlitic and spheroidized steels. Such a specimen should contain no textural stresses ascribable to the presence of a second phase, and might provide a base line for the measurements on the pearlitic and spheroidized steels.

The decarburized specimen was prepared by cutting $\frac{3}{16}$-in.-thick disks from the stock material and decarburizing them with wet hydrogen at 1,650° F. Several attempts were made before a homogenized specimen containing a trace of pearlite was obtained. The heat treatments to obtain the pearlitic and spheroidized conditions were conventional. The decarburized portions were removed and the whole specimens were given a prolonged electropolishing treatment in order to diminish the possibility of body stresses resulting from a carbon concentration gradient. The specimens then were mounted in Bakelite and polished by repeated cycles of light mechanical and electropolishing treatments until the sharpness of the X-ray diffraction indicated that the surfaces were essentially free of cold work.

The same two-exposure method of obtaining X-ray data for surface stress calculations was followed with each of the three types of steel as had been followed with the brass specimens. From the steels, diffraction lines were obtained only from the ferrite and, during the same exposure, from a calibrating powder spread thinly on the surface of the steel. Diffraction from the cementite is not observed in the high angle region from steel with this carbon content. Three pairs of patterns were made from each of the three specimens with three different radiations and slightly varying conditions. In one case, cobalt radiation was used with tungsten as the calibration powder, iron radiation was used with tungsten calibration also, and chromium radiation was used with silver calibration. Subject to the limitations of the specimen holder and Bragg angles, the angles of incidence for the inclined exposures of each pair were 45°, 30°, and 45°, respectively.

The mechanics of getting the patterns, processing the films, reading and averaging the data, etc., were in no way significantly different with the steel specimens than with the brasses. The results, along with the probable errors and the computed theoretical values, are presented in table 2.

When examining this table, one should first notice the variation in the observed probable errors in the stress; this error is nearly three times as large for iron radiation as it is for cobalt. The reason for this lies in the sizes of the Bragg angles given in the table. The stresses measured by cobalt and by chromium radiation at the two larger angles, however, do show the expected trend, which is the same as that in the theoretical values, in the order: pearlitic, spheroidized, and decarburized. The mass absorption coefficients, μ/ρ, of iron for the three radiations are also shown in the table. The cobalt radiation is the most penetrating, and is, therefore, the most reliable, because it reveals by diffraction the condition of the largest number of crystallites in the largest volume and is affected least by any residual surface preparation distortion that might be present. The average values of the stress shown in the table were weighted with respect both to the probable error in observation and the penetration of the radiation.

The theoretical values in this table were computed with the aid of formulas for the specific lamellar and spheroidal cases given in László's first paper. The elastic constants used were those cited by László: $E=30\times10^6$ lb/in.^{2}; $\nu=0.30$, the coefficient of linear thermal expansion of ferrite equals 14.98×10^{-6}/°C, and that of cementite 12.16×10^{-6}/°C. The temperature drop in the calculations was taken to be 680° C. Again, the agreement between the theoretical values and the observed averages was reasonably good.

4. Conclusions and Discussion

In previous investigations involving X-ray stress measurement, it has generally been assumed that carefully annealed material was strain-free. László's theoretical work showed that inequalities of thermal expansion would cause textural (tessellated) stresses in two-phase alloys, but no direct measurement of

TABLE 2. *Stresses in steel*

Specimen			Pearlitic		Spheroidized		Decarburized		Probable error in stress
Radiation	ϑ	μ/ρ	η	σ	η	σ	η	σ	
				lb/in.^{2}		*lb/in.*^{2}		*lb/in.*^{2}	*lb/in.*^{2}
Co	81	54	3.99×10^{-4}	14.12×10^3	1.00×10^{-4}	3.56×10^3	0.16×10^{-4}	0.57×10^3	1.92×10^3
Fe	73	72	1.30	5.57	1.59	6.84	2.45	10.52	5.34
Cr	78	115	4.20	14.38	3.18	10.89	2.72	9.29	2.02
Weighted average				12.74		6.05		4.58	2.53
Theoretical				9.2		6.2			

these stresses had been made. Contrary to the implication in one of László's papers, the results of this work demonstrate that textural stresses of this type can be measured by changes in the lattice constants if sufficient care is taken. The major experimental limitation is the problem of surface preparation, the routine of repeated cycles of light mechanical polishing and light electropolishing apparently being the best method available at present.

In the present investigation, good agreement was obtained between theoretical stress values and those obtained by X-ray diffraction in the case of alpha-beta brass, and at least qualitative agreement in the case of 1.05 percent carbon steels with various microstructures. The experimental precision was, in most cases, thought to be such that the probable error in stress measurement was a few thousand pounds per square inch.

In addition to the quantitative aspect of agreement with theory, these results reveal, by direct measurement, the impossibility of obtaining complete strain relief in a material that contains more than one phase. They will, perhaps, thus serve to emphasize the necessity of considering textural stresses as an ever-present factor in stress corrosion, surface distortion, fatigue, and similar problems. In this manner they may play some part in the very broad field of study relating the internal stress system in a metal specimen to the mechanical and physical properties and behavior of the body.

The authors wish to acknowledge the assistance of many persons in connection with this work. Among them are Hugh Logan, who supplied some of the early experimental brass alloys; personnel of the Naval Gun Factory and the foundry of the Metallurgy Division at the National Bureau of Standards, who were instrumental in providing the ultimate brass material; Nathan Koenig, who did the greater part of the metallographic work; and Harvey Utech, who made an independent set of measurements of the X-ray patterns.

5. References

[1] E. Orowan, Classification and nomenclature of internal stresses, Symposium on internal stresses in metals and alloys, Inst. Metals (London), Monograph and Rep. Ser. No. 5, 47–59 (1948).

[2] F. László, Tessellated stresses, parts I to IV: J. Iron Steel Inst. London **147,** 173–199 (1943); **148,** 137–159 (1943); **150,** 183–207 (1944); **152,** 207–228 (1945).

[3] F. R. N. Nabarro, László's papers on tessellated stresses: A review, Symposium on internal stresses in metals and alloys, Inst. Metals (London), Monograph and Rep. Ser. No. 5, 61–72 (1948).

[4] J. P. Nielsen and W. R. Hibbard, An X-ray study of thermally induced stresses in microconstituents of aluminum-silicon alloys, J. Appl. Phys. **21,** 853–854 (1950).

[5] D. V. Wilson, An X-ray investigation of structural changes in steel due to cold working, J. Iron Steel Inst. (London) **165,** 376–381 (1950).

[6] L. Reimer, X-ray investigation of the influence of carbon content on internal stresses in steel and iron, Z. Metallkunde **46,** 39–42 (1955).

[7] V. Hauk, Concerning residual stresses after plastic deformation in tension, Z. Metallkunde **46,** 33–38 (1955).

[8] C. J. Newton and H. C. Vacher, Residual lattice strains in sectioned bars of plastically deformed iron, J. Metals **7,** 1193–1194 (1955).

[9] C. S. Barrett, Structure of metals, p. 323 (McGraw-Hill Book Co., Inc., New York, N. Y., 1952).

[10] J. T. Norton, X-ray methods in the field of residual stresses, Exptl. Stress Anal. **2,** 157–160 (1944).

[11] W. Boas and F. K. Mackenzie, Anisotropy in metals (B. Chalmers, ed.), Progr. Metal Phys. **2,** 90–120 (1950).

[12] H. H. Stadelmaier, Some notes on the relation between the elastic moduli of anisotropic crystallites and quasi-isotropic polycrystalline aggregates, J. Appl. Math. Phys. **6,** 248–251 (1955).

[13] G. B. Greenough, Residual stresses associated with lattice strains. Residual stresses in metals and metal construction (W. R. Osgood, ed.), p. 285–296 (Reinhold Publishing Corp., 330 W. 42d St., New York, N. Y., 1954).

[14] A. Huber and E. Schmid, Determination of the elastic properties of quasi-isotropic polycrystals by means of approximation to the mean, Helv. Phys. Acta **7,** 620–627 (1934).

[15] P. D. Merica and L. W. Schad, Thermal expansion of alpha and beta brass between 0° and 600° C, Bul. BS 14, p. 571–590 (1918–1919).

WASHINGTON, February 8, 1957.

Journal of Research of the National Bureau of Standards Vol. 59, No. 4, October 1957 Research Paper 2794

Dissociation of 4-Chloro-4′-Aminodiphenylsulfone

Elizabeth E. Sager and Fleur C. Byers

The ultraviolet absorption spectra of 4-chloro-4′-aminodiphenylsulfone has been determined. The dissociation may be considered as the acidic dissociation of the ammonium ion which is formed with the addition to the base of hydrogen ion from an acid such as hydrochloric acid. Spectrophotometric measurements of several concentrations of 4-chloro-4′-aminodiphenylsulfone at various known hydrogen-ion concentrations were made at 25° C, from which the values pK_c, based upon the concentrations, were determined. From these, the value of pK_a was derived. At 25° C, pK_a is 1.38, which corresponds to a value of 0.042 mole per liter for K_a. The activity coefficient terms may be expressed simply as a linear function of the ionic strength. Spectrophotometric measurements were also made at 15°, 20°, 25°, 30°, and 35° C on certain solutions in order to calculate the heat of dissociation. It was found to be 21,000 joules deg^{-1} mole^{-1}. The basic dissociation constant, K_b, is 2.4×10^{-13}, or pK_b is 12.62.

1. Introduction

Derivatives of diphenylsulfone, such as dihydroxydiphenylsulfone and diaminodiphenylsulfone, have attracted attention as intermediates particularly in the synthesis of biocides. Heymann and Fieser have prepared many derivatives of the parent compound 4,4′-diaminodiphenylsulfone in their research studies of antimalarials [1].[1] They kindly supplied us with several compounds which they had prepared and we have used them in our studies of the spectral absorbance of organic compounds. The diphenylsulfones are almost insoluble in water, but solutions of the order of 10^{-4} to 10^{-5}-M may be obtained which are suitable for spectrophotometric measurements. Derivatives of diphenylsulfone absorb in the ultraviolet portion of the spectrum and measurements in this region afford a satisfactory means of observing some aspects of their chemical behavior.

Compounds of similar molecular structure, specifically benzophenone, 4-aminobenzophenone, and 4,4′-diaminobenzophenone have already been studied at the Bureau. Reports have been published including the ultraviolet spectra, dissociation reactions, and the effect of temperatures in the range of 10° to 40° C upon the spectra [2,3,4]. This paper deals specifically with the acidic dissociation of the ammonium ion of 4-chloro-4′-aminodiphenylsulfone at 25° C, and with the effect of temperature upon its dissociation.

2. Experimental Procedure

2.1. Materials

4-Chloro-4′-aminodiphenylsulfone is a white crystalline material that melts at 183 to 187° C [1]. The solubility in water is about 20 mg/liter at 25° C.

Hydrochloric acid of reagent grade was used to adjust the hydrogen-ion concentration of most of the solutions. Standardized sodium hydroxide, free from carbonate, was also employed. Conductivity water was used to prepare the stock solutions and for subsequent dilutions.

[1] Figures in brackets indicate the literature references at the end of this paper.

2.2. Equipment

A model DU Beckman spectrophotometer was equipped with a specially designed cell compartment with sides, bottom, and removable top which were water-jacketed. The temperature within the cell compartment was controlled by circulating water from a water bath controlled by a thermostat.

A commercial glass-electrode assembly was used to make pH measurements of all solutions.

All equipment except the water bath was housed in a constant-temperature room at 25° C. Solutions were prepared and stored in this room.

3. Calculation of Dissociation Constants From Spectral Absorbance Data

3.1. Absorbance Measurements

4-Chloro-4′-aminodiphenysulfone exists as the base in water. When hydrogen ion from an acid such as hydrochloric acid is added, it is transformed to the ionic state, thus

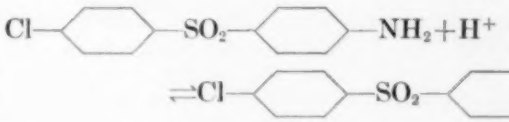

The reaction may be simply represented as the acidic dissociation of the ammonium ion, namely, $RNH_3^+ \rightleftharpoons RNH_2 + H^+$.

According to the law of absorption, at any given wavelength,

$$\text{Molar absorbance} = A/bM \qquad (1)$$

in which A is the absorbance of the sample being measured ($-\log_{10}$ transmittancy), b is the depth of solution in centimeters through which the radiant energy passes, and M is the molar concentration of the absorbing compound. The quantity A/bM is frequently called molecular extinction coefficient, and is represented by the symbol ϵ. Molar absorbance is expressed in liters mole^{-1} cm^{-1}.

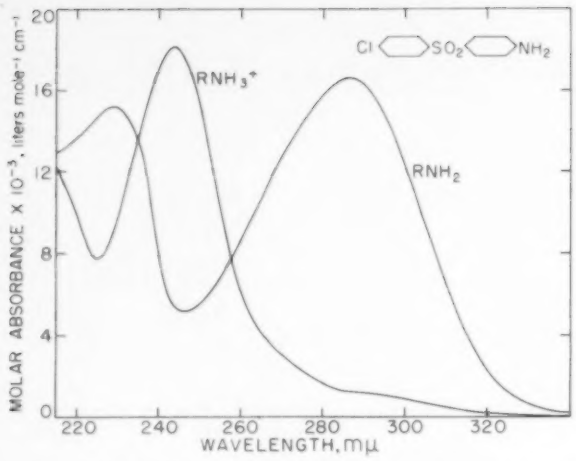

FIGURE 1. *Molar absorbance of 4-chloro-4′-aminodiphenylsulfone in the molecular state* (RNH_2) *and the ionic state* (RNH_3^+).

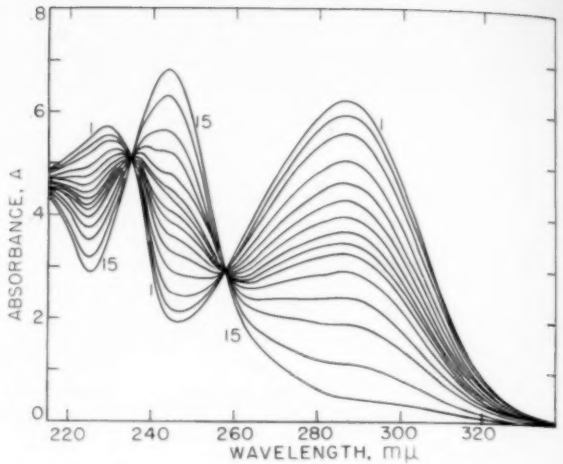

FIGURE 2. *Absorbance values of 4-chloro-4′-aminodiphenylsulfone at various hydrogen-ion concentrations representing its dissociation* (3.75×10^{-5}-*M in 1-cm absorption cells*).

The values of molar absorbance for the molecular and the ionic states of 4-chloro-4′-aminodiphenylsulfone are shown in figure 1. The curve marked RNH_2 shows maximum molar absorbance of about 17,000 liters mole^{-1} cm^{-1} at a wavelength of 286 mμ. The compound is transformed to the ionic state, RNH_3^+, in a solution of hydrochloric acid, 0.05-*M*, and exhibits maximum molar absorbance of about 18,000 liters mole^{-1} cm^{-1} at a wavelength of 244 mμ.

Observations were made on four different series of solutions of 4-chloro-4′-aminodiphenylsulfone at various stages of the dissociation at known hydrogen-ion concentrations. A typical series is shown in figure 2. Absorbance values corresponding to experimental transmittancy values of a 3.75×10^{-5}-*M* solution of the diphenylsulfone in 1-cm absorption cells are plotted as a function of wavelength. Curve 1 represents RNH_2 in water, and curve 15, RNH_3^+ in 0.5-*M* hydrochloric acid. The intermediate stages in the dissociation are shown in curves 2 to 14 inclusive. The two well-defined isosbestic points at 234.8 and 258 mμ not only indicate purity of the compound but show that only one reaction, that of dissociation, is taking place. The amounts of each species of the partially dissociated compound are proportional to their absorbance values (curves 1 and 15). The absorbance data may therefore be used to calculate the percentage dissociated into ions. Let α represent this percentage, which can be calculated from the following equation:

$$\alpha=\frac{A_{RNH_2}-A_a}{A_{RNH_2}-A_{RNH_3^+}}, \tag{2}$$

in which A_{RNH_2} is the absorbance of the molecular species, A_a is the absorbance at any dissociation step, and $A_{RNH_3^+}$ is the absorbance of the ionic species.

3.2. Calculation of Concentration Constants

The concentration constant, K_c, can be calculated according to the equation

$$K_c=\frac{[RNH_2][H^+]}{[RNH_3^+]}, \tag{3}$$

in which $[RNH_2]$, $[H^+]$, and $[RNH_3^+]$ are the concentrations of the free base, hydrogen ion, and the ionic species, respectively. Since α represents the degree of dissociation into ions, $1-\alpha$ is the fraction of the remaining base, and we have the familiar equation

$$K=\frac{(1-\alpha)[H^+]}{\alpha}. \tag{4}$$

It is advisable to observe the resulting α values for variations or trends in the calculated values. In this case it is obvious that best results can be obtained from about 280 to 292 mμ. Calculated α values at nine wavelengths are given in table 1.

Average values of α are used to calculate each ratio of $(1-\alpha)/\alpha$ at the various hydrochloric acid concentrations as shown in table 2. The corrected hydrogen-ion concentration is that of the hydrochloric acid less the amount of hydrogen ion used for the dissociation step corresponding to α. This figure multiplied by the ratio $(1-\alpha)/\alpha$ gives the concentration constant, K_c. The negatives of the logarithms of the constants, or pK_c values, are then found.

3.3. Estimation of pK_a at 25° C

The true thermodynamic constant, K_a, is calculated by eq (5),

TABLE 1. *Absorbance values of 4-chloro-4'-aminodiphenylsulfone (3.747×10^{-5}-M) and calculated values of α at several wave lengths*

Solution	Absorbance and α	Wavelength (mμ)							
		280	282	284	285	286	287	288	290	292
1	A	0.5884	0.6056	0.6162	0.6198	0.6216	0.6216	0.6198	0.6091	0.5935
	α	.000								
2	A	.5654	.5817	.5901	.5943	.5943	.5943	.5918	.5850	.5686
	α	.044	.043	.046	.045	.048	.047	.049	.043	.045
3	A	.5339	.5452	.5544	.5575	.5575	.5575	.5560	.5498	.5331
	α	.104	.110	.109	.109	.112	.111	.111	.105	.110
4	A	.4828	.4948	.5045	.5059	.5072	.5072	.5059	.4962	.4828
	α	.201	.201	.197	.199	.199	.199	.199	.200	.201
5	A	.4443	.4541	.4609	.4622	.4641	.4622	.4609	.4541	.4413
	α	.274	.275	.274	.276	.274	.277	.277	.275	.276
6	A	.4123	.4202	.4260	.4283	.4295	.4295	.4260	.4202	.4078
	α	.335	.337	.336	.335	.335	.334	.338	.335	.337
7	A	.3830	.3893	.3958	.3969	.3969	.3969	.3947	.3893	.3778
	α	.391	.393	.389	.390	.392	.391	.392	.390	.392
8	A	.3575	.3635	.3675	.3686	.3686	.3686	.3675	.3615	.3507
	α	.439	.440	.439	.439	.441	.440	.440	.439	.441
9	A	.3372	.3410	.3458	.3468	.3468	.3468	.3449	.3391	.3298
	α	.478	.481	.478	.478	.479	.478	.479	.478	.479
10	A	.3179	.3224	.3261	.3270	.3270	.3270	.3251	.3188	.3098
	α	.515	.514	.512	.512	.513	.512	.514	.514	.515
11	A	.2848	.2865	.2907	.2916	.2916	.2907	.2890	.2840	.2757
	α	.578	.580	.575	.574	.575	.576	.577	.576	.577
12	A	.2388	.2396	.2411	.2411	.2411	.2403	.2388	.2358	.2284
	α	.665	.665	.663	.663	.663	.663	.664	.662	.663
13	A	.1931	.1904	.1904	.1891	.1891	.1884	.1878	.1844	.1791
	α	.752	.754	.752	.753	.754	.754	.753	.753	.753
14	A	.1209	.1163	.1135	.1124	.1118	.1107	.1096	.1085	.1046
	α	.890	.889	.888	.888	.888	.889	.889	.887	.888
15	A	.0630	.0550	.0501	.0482	.0477	.0467	.0462	.0448	.0429
	α	1.000								

TABLE 2. *Dissociation of 4-chloro-4'-aminodiphenylsulfone (3.747×10^{-5}-M)*

Solution	Average $[R^+]$	$(1-\alpha)/\alpha$ $[R]/[R^+]$	Molar concentration of HCl	Corrected concentration of hydrogen ion $[H^+]$	Concentration constant, K_c	$-\log_{10}K_c$ pK_c	$-\log f=1.0\,\mu$	$pK_a=pK_c-(-\log f)$	f
1	0.000								
2	.046	20.739	2.002×10^{-3}	2.000×10^{-3}	4.148×10^{-2}	1.382	0.002	1.380	1.005
3	.109	8.174	5.005	5.001	4.088	1.388	.005	1.383	1.012
4	.200	4.000	10.010	10.003	4.001	1.398	.010	1.388	1.024
5	.276	2.623	15.015	15.005	3.936	1.405	.015	1.390	1.035
6	.336	1.976	20.020	20.007	3.953	1.403	.020	1.383	1.048
7	.391	1.557	25.025	25.010	3.894	1.410	.025	1.385	1.059
8	.440	1.273	30.030	30.014	3.820	1.418	.030	1.388	1.072
9	.479	1.087	35.035	35.017	3.806	1.420	.035	1.385	1.084
10	.513	0.949	40.040	40.021	3.798	1.421	.040	1.381	1.097
11	.576	.736	50.050	50.028	3.682	1.434	.050	1.384	1.109
12	.663	.508	70.000	69.975	3.555	1.449	.070	1.379	1.175
13	.753	.328	100.000	99.972	3.279	1.484	.100	1.384	1.259
14	.888	.127	200.000	199.967	2.540	1.595	.200	1.395	1.585
15	1.000	.000	500.000						

$$K_a=K_c\frac{f_{H^+}f_{RNH_2}}{f_{RNH_3^+}}, \tag{5}$$

in which the activity coefficients are identified with appropriate subscripts. For simplicity this combined term will henceforth be referred to as f. Then

$$pK_a=pK_c-\log f. \tag{6}$$

When the values of pK_c are plotted as a function of the ionic strength, μ, a satisfactory extrapolation to the value of pK_a can be made. The slope of the line is about 1.0, as shown in figure 3. Therefore $-\log f$ may be considered equal to 1.0 μ. The values of $-\log f$ may be subtracted from the experimental pK_c values to obtain individual pK_a values that can be averaged. By this method of calculation pK_a is found to be 1.38, with an estimated uncertainty of

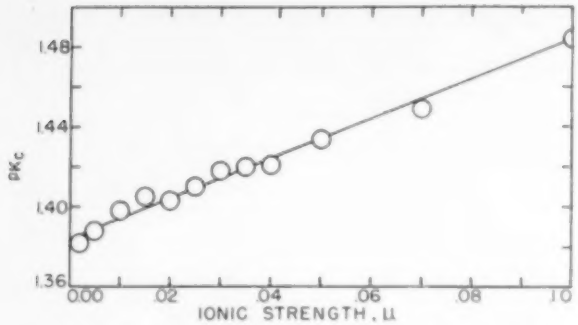

FIGURE 3. *pK_c values plotted as a function of the ionic strength for extrapolation to pK_a.*

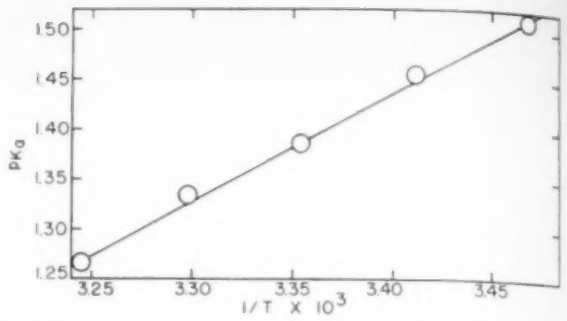

FIGURE 4. *pK_a values at temperatures from 15° to 35° C plotted as a function of $1/T$.*

TABLE 3. *Calculation of pK_a from absorbance data at 15° to 35° C*

Temperature	Absorbance at 286 mμ				0.015-*M* HCl				0.035-*M* HCl			
°C	A_{RNH_2}	$A_{RNH_3^+}$	$A_{.015HCl}$	$A_{.035HCl}$	$(1-\alpha)/\alpha$	K_c	pK_c	pK_a	$(1-\alpha)/\alpha$	K_c	pK_c	pK_a
15	0.5809	0.0366	0.3968	0.2831	1.957	0.0294	1.532	1.517	0.828	0.0290	1.538	1.503
20	.5793	.0410	.4134	.3001	2.245	.0337	1.472	1.457	.928	.0325	1.488	1.453
25	.5767	.0453	.4300	.3224	2.623	.0393	1.406	1.391	1.090	.0382	1.417	1.382
30	.5725	.0520	.4407	.3400	2.949	.0442	1.355	1.340	1.239	.0434	1.363	1.328
35	.5654	.0575	.4522	.3560	3.487	.0523	1.281	1.266	1.426	.0499	1.302	1.267

± 0.01 at 25° C. Values of f corresponding to each value of the ionic strength in this series are shown in the last column of the table.

3.4. Heat of Dissociation

The heat of dissociation is calculated from the equation

$$d \log K/dT = \Delta H/2.303RT^2, \quad (7)$$

in which ΔH represents the change of molar heat content for the dissociation, R is the gas constant (8.3144 joules deg^{-1} mole^{-1}), and T is the temperature in degrees Kelvin (degrees Celsius plus 273.16).

Four solutions in one series, 3.48×10^{-5}-*M* with respect to 4-chloro-4′-aminodiphenylsulfone, were observed throughout the ultraviolet spectral range at five temperatures, namely 15°, 20°, 25°, 30°, and 35° C. They represented the dissociated state, the undissociated state, and two intermediate stages of dissociation at 0.015-*M* and 0.035-*M* hydrochloric acid concentrations. Absorbance values at the different temperatures, at wavelength 286 mμ only, are shown in table 3. The K_c and pK_c values are calculated for the two concentrations in the usual manner. In this limited temperature range no significant error is introduced by considering concentrations independent of temperature. Assuming that the same activity coefficient terms ($-\log f = 1.0\,\mu$) apply at the temperature used, which is, of course, not strictly true, pK_a values can be estimated from data for the two solutions. They agree within 0.01 pK unit at each temperature, so an average is used. A plot of the pK_a values against $1/T\times10^3$, as shown in figure 4, yields a practically straight line indicating that the heat of dissociation is nearly constant over the temperature range studied. ΔH is found to be approximately 21,000 joules deg^{-1} mole^{-1}. This value is not very different from one of 19,000 reported earlier in a study of 4-aminobenzophenone which was based on more extensive data.

3.5. Basic Ionization Constant, K_b

The basic ionization constant, K_b, is derived from the usual relationship

$$K_b = K_w/K_a, \quad (6)$$

in which K_w is the activity product of water. For 4-chloro-4′-aminodiphenylsulfone K_b is $10^{-14}/4.2\times10^{-2}$ at 25° C, or 2.4×10^{-13}. This gives an equivalent value of 12.62 for pK_b.

4. References

[1] Hans Heymann and Louis F. Fieser, J. Am. Chem. Soc. **67,** 1979 (1945).

[2] Elizabeth E. Sager and Iris J. Siewers, J. Research NBS **45,** 489 (1950) RP2162.

[3] Elizabeth E. Sager and Iris J. Siewers, J. Research NBS **49,** 7 (1952) RP2337.

[4] Elizabeth E. Sager and Fleur C. Byers, J. Research NBS **58,** 33 (1957) RP2731.

WASHINGTON, March 19, 1957.

Journal of Research of the National Bureau of Standards Vol. 59, No. 4, October 1957 Research Paper 2795

Speed of Sound in Water by a Direct Method[1]

Martin Greenspan and Carroll E. Tschiegg

The speed of sound in distilled water was measured over the temperature range 0° to 100° C with an accuracy of 1 part in 30,000. The results are given as a fifth-degree polynomial and in tables. The water was contained in a cylindrical tank of fixed length, terminated at each end by a plane transducer, and the end-to-end time of flight of a pulse of sound was determined from a measurement of the pulse-repetition frequency required to set the successive echoes into time coincidence.

1. Introduction

The speed of sound in water, c, is a physical property of fundamental interest; it, together with the density, determines the adiabatic compressibility, and eventually the ratio of specific heats. The variation with temperature is anomalous; water is the only pure liquid for which it is known that the speed of sound does not decrease monotonically with temperature.

There is also a practical interest in c in that water is used as a standard liquid for the calibration of instruments that measure the speed of sound in liquids automatically, both in the laboratory and in the field. In fact, it was in connection with the calibration of such "velocimeters" [1][2] that our interest in this work was first aroused. In the first place, the available data scatter widely, as recent summaries [2, 3] clearly show. In many cases, the discrepancies far exceed the claimed accuracy or at least the precision of the methods, even when the methods compared are the same. In the second place, there exists no set of data that gives a smooth variation with temperature over any considerable range. In particular, the best of these data yield calibration curves for our velocimeters which are badly curved instead of straight (as they should be), and about which the data scatter irregularly, but reproducibly. The results here presented are free of these objections.

2. Method

At the top of figure 1 is a schematic of the apparatus. The sample is confined in a tube of which the ends are plane, parallel, electroacoustic transducers, quartz crystals in this case. If the left-hand crystal, say, is excited by a short pulse from the blocking oscillator, the oscilloscope, which measures the voltage on the right-hand crystal, will show a received pulse and a series of echoes, as indicated in idealized form on the line below (fig. 1). The pulse repetition frequency of the blocking oscillator is controlled by a sine-wave oscillator, and if this frequency were adjusted so that each blocking oscillator pulse coincided with the first received pulse of the next preceding cycle, then the oscillator period would equal the time of flight of the pulse. However, as the two pulses have different shapes, the accuracy with which the coincidence could be set would be very poor. Instead, the oscillator is run at about half this frequency and the coincidence to be set is that among the first received pulses corresponding to a particular electrical pulse, the first echo corresponding to the electrical pulse next preceding, and so on. Figure 1 illustrates the successive signals corresponding to three electrical input pulses. The input pulses fall halfway between the pulses for which the coincidence is set, so that they do not tend to overload the amplifier or distort the oscilloscope traces. The period of the oscillator, when properly set, multiplied by twice the length of the tank, is the speed of sound in the sample.

The oscilloscope trace actually looks like that shown in the inset (fig. 1). The first cycle corresponds to sound reflected from the inner faces only of the transducers, whereas the succeeding cycles correspond to sound reflected one or more times from an outer face. Therefore, the coincidence is set by maximizing the peak on either the first or second half-cycle; the same result is obtained in either case but the second half cycle is easier to use because it is bigger. What we are measuring here is the speed corresponding to the first arrival of the signal; in a nondispersive liquid this is the same as the phase velocity. It is true that the coincidence is made at a

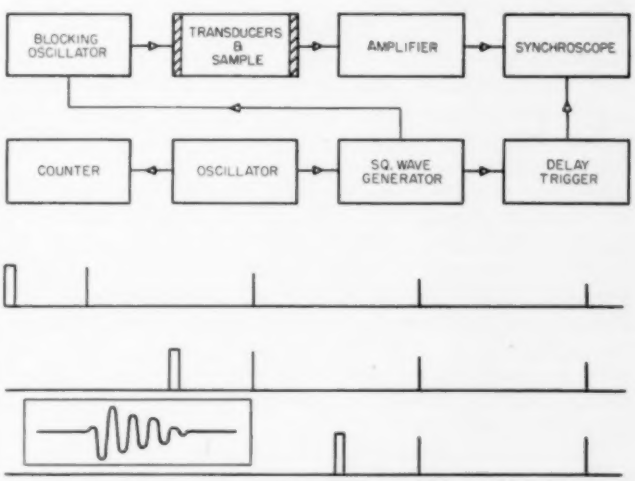

FIGURE 1. *Schematic of method.*

The three lower lines show in idealized form the events corresponding to three successive electrical pulses. The short, thick line represents the input pulse.

[1] This work was supported in part by the Office of Naval Research under contract NA-onr-70-48.

[2] Figures in brackets indicate the literature references at the end of this paper.

time one-fourth or three-quarters of the transducer period later than the time of first arrival, by which time there is opportunity for sound traveling by paths other than the shortest to affect the location of the maximum. However, the results are independent of whether the first or second half cycle is used; they are also not affected by substituting crystals of twice the thickness, or by changing the diameters of the tank, or of the hot electrodes. These results lead us to believe that the error introduced by this maximization technique is negligible.

The question has been examined also in another way. Suppose a coincidence to have been made at frequency f; others can then be made at submultiples of f. At the frequency $f/2$ for instance, the first received pulse corresponding to a particular input pulse coincides with the second echo (not the first, as before) corresponding to the electrical pulse next preceding, and so on. Effectively, the sound pulse is timed over a path twice as long as before. It is found that the measurements at f and near $f/2$ are substantially identical, so that the error in question is less than, or at most comparable to, the experimental error of the time measurement.

3. Apparatus

3.1. The Delay Line

The disassembled delay line is shown in the photograph, figure 2. The length of the tank is about 200 mm, and the bore about 13 mm. The filling holes are sealed by plugs having Teflon gaskets; a small hole in one plug provides pressure release.

The tank is of a chromium steel [3] which, after heat treatment, takes a good optical finish. Because this steel is not so corrosion resistant as the nickel-chromium stainless steels, the bore of the tank was heavily gold plated.

The ends of the tank are optically flat and parallel to within less than 1 μ. To these ends are carefully wrung the 0.8-mm thick x-cut quartz crystals, which also are optically flat. The caps, when bolted on, clamp the crystals through neoprene O-rings. A coaxial cable passes through a seal in each cap, and the center conductor makes contact with the outer (hot) electrode of the crystal through a light spring.

The outer electrode is a 9 mm circle of aluminum-backed pressure-sensitive adhesive tape. The inner (ground) electrode is of fired-on gold and is about 12 mm in diameter. Contact is made through a light gold-plated helical spring which touches the electrode around the edge and bears on a shoulder machined into the bore. The inner electrodes and springs are unnecessary if the sample has high conductivity or a high dielectric constant; they are usually omitted for water and aqueous solutions of salts. Figure 3 is a schematic drawing of one end of the assembly.

The length of the tank was measured at 20° C, and the coefficient of thermal expansion of the steel was measured on a sample cut from the same bar as

[3] Firth-Sterling type B–440A.

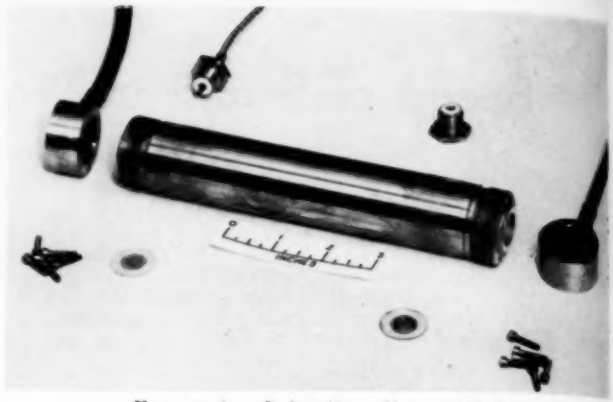

FIGURE 2. *Delay line, disassembled.*

Above the tank are the plugs which close the filling holes, and at the ends are the caps through which pass the electrical cables and which also clamp the crystals seen in the foreground.

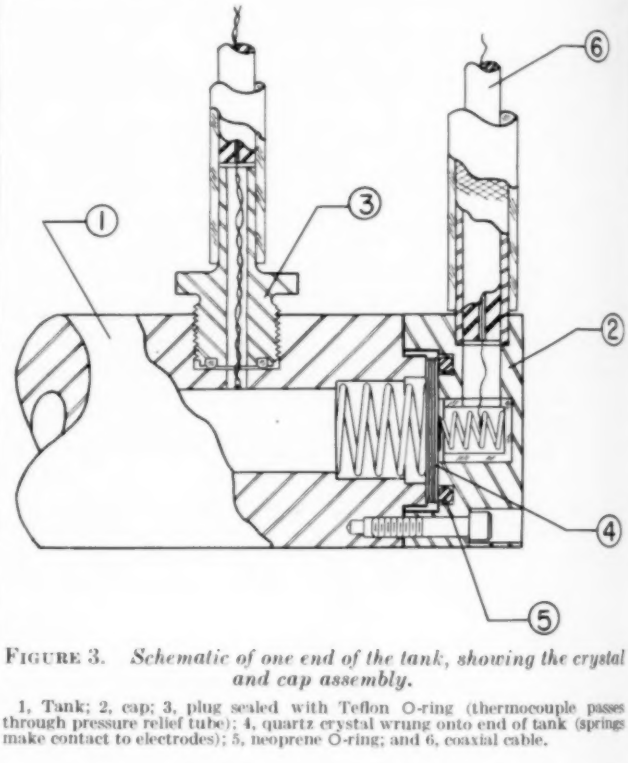

FIGURE 3. *Schematic of one end of the tank, showing the crystal and cap assembly.*

1, Tank; 2, cap; 3, plug sealed with Teflon O-ring (thermocouple passes through pressure relief tube); 4, quartz crystal wrung onto end of tank (springs make contact to electrodes); 5, neoprene O-ring; and 6, coaxial cable.

was the tank and heat-treated together with it. From these data, the length of the sound path is known to better than 2 parts in 10^5 at any temperature between 0° and 100° C. It is, of course, necessary that the crystals be wrung down with great care so that the fringes disappear all around the periphery, to achieve this accuracy. The clamping gaskets must bear directly over the contacting surface and not spread out over the unsupported area, else the crystal will bend. With these precautions, the delay line may be disassembled and reassembled repeatedly with reproducible results. If the crystals have been properly wrung on and clamped, they cannot be removed by hand after several days, but must be soaked off.

3.2. The Electronics

The electronic circuits (fig. 1) are, for the most part, conventional. However, the oscillator and the pulse-forming circuits must be exceptionally free of jitter. In addition, the oscillator must be provided with fine frequency control, so that it can be set within the required sensitivity of measurement, and it must be so stable that the frequency does not change during the counting time by enough to alter the count by more than one.

The blocking oscillator produces a pulse about 100 v high and 0.05 to 0.25 μsec wide. It is best driven by a large, fast pulse such as is gotten by differentiation of a square wave derived, in turn, from the sine-wave generator.[4] The jitter may be reduced further by means of a narrow band filter after the oscillator.

The receiving circuit consists simply of a short length of low-capacitance cable, a wide band (5.5 Mc, in this case) amplifier of gain 100 to 1,000, and a high-frequency type oscilloscope equipped with fast sweeps. The sweep is triggered from the oscillator through a variable delay; the necessary delay time is about half the oscillator period.

3.3 Temperature Control and Measurement

The delay line, suspended from its cables, is deeply immersed in a 27 gal, well-insulated, water bath. The bath is provided with 2 pump-type stirrers, 3 heating coils, and a cooling coil connected to a small refrigeration unit. The temperature of the water adjusts itself so that the losses equal the power input to the heating coils, and various temperatures are obtained simply by varying the power input. The temperature is, by this means, easily held to within less than 0.005 deg C for the interval of time required for the measurements, except that above 75° C, or so, the variation may become 0.02° or 0.03° C; at the higher temperatures, however, the thermal coefficient of the speed of sound in water is rather low.

The temperature of the bath water is measured with a platinum resistance thermometer and Mueller Bridge. A differential thermocouple has one junction in the sample in the delay line, and one tied to the platinum thermometer; it passes through the pressure release tube (fig. 2). The thermocouple reading serves to indicate when the sample and bath water are substantially in thermal equilibrium, and measurements are made when the discrepancy is less than 0.01° C (somewhat greater at the high temperatures). The thermocouple and galvanometer combination was calibrated for small temperature differences against the platinum resistance thermometer so that small corrections to the temperature readings could be made.

3.4. Samples

The measurements here reported were made on three separate samples of water. One sample was ordinary laboratory distilled water. This was boiled and poured, while still hot, into the preheated tank. Although dissolved air has a negligible effect on the speed of sound in water [4], it is desirable to exclude air and so prevent possible bubble formation on the transducers.

The other two samples were vacuum distilled directly into the tank. The tank was placed in an ice bath and connected to a flask of distilled water. The system was then evacuated, and the water allowed to distill over at about 50° C.

The results of the three runs were the same within the errors of measurement; the data were, therefore, combined.

3.5. Technique

The water bath was cooled to just above 0° C, and the heaters were operated at low power to stabilize the temperature. (Below room temperature the refrigeration machine was run continuously.) After the readings were taken, the power input to the heaters was increased, and so on until the temperature was just below 100° C. When the temperature was stabilized, as indicated by the constancy of the Mueller bridge reading and the near zero reading of the thermocouple galvanometer, the coincidence was set on the oscilloscope by one observer and the frequency (doubled for convenience) was measured by counting cycles for 10 sec (about 75,000 counts) by means of an electronic counter. At the same time, another observer balanced and read the Mueller bridge and read the thermocouple galvanometer deflection.

While the temperature readings were being made, the coincidence was independently set and the resulting frequency measured three times or more. The various readings were always within the ± 1 count inherent error (even for different observers) and the modal value was recorded. This, divided by 20 and multiplied by the length of the tank at the particular temperature, was taken as the speed of sound, c, corresponding to the temperature, T, obtained by calculation from the platinum thermometer and the thermocouple readings and the associated calibration data. All temperature calculations were made to the nearest 0.001° C and the final result was rounded off to the nearest 0.01° C.

In order to insure that the coincidence was set on the proper cycle, it was first set approximately, using the coarse frequency control, at a moderate sweep speed and low oscilloscope gain, so that the entire pulse was visible on the screen. The sweep speed was then increased while the delay was readjusted to keep the proper cycle centered. Next, the gain was increased while the base line was moved off the screen to keep the point of extreme deflection centered, and the amplitude was then adjusted to a maximum using the fine frequency control.

4. Results

From readings taken at 83 temperatures between 0.14° and 99.06° C, the calculated values of the speed of sound were fitted by the electronic com-

[4] The square-wave generator must be of the type that amplifies and then clips the input sine wave. The free-running, synchronized type is not suitable.

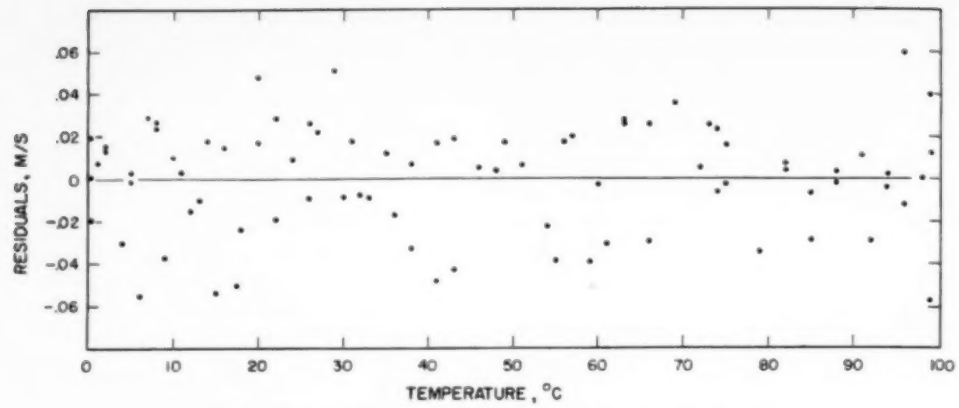

FIGURE 4. *Deviations, r, of equation 1 from the data.*

puter SEAC by the method of least squares, to a fifth-degree polynomial,

$$c=\sum_{i=0}^{5} a_i T^i. \qquad (1)$$

The reduction in the residual sum of squares over a fourth-degree polynomial, due to fitting the fifth-degree term, was statistically significant at a probability level less than 0.005, and the deviations of the data from the fifth-degree polynomial showed no statistically significant indication of lack of randomness. The deviations are plotted against temperature in figure 4.

The values of a_i in eq (1), for c in meters per second (m/s), and T in degrees C, are: $a_o=1{,}402.736$; $a_1=5.03358$; $a_2=-0.0579506$; $a_3=3.31636\times10^{-4}$; $a_4=-1.45262\times10^{-6}$; and $a_5=3.0449\times10^{-9}$. The standard deviation of the measurements is 0.0263 m/s, or about 17 ppm. Estimated standard deviations of the values of c predicted by eq (1) were calculated for five representative temperatures. The results are given in table 1.

TABLE 1. *Estimated standard deviation (s. d.) of values of c predicted by equation 1*

Temperature	s. d.	
°C	m/s	ppm
0	0.0114	8.1
10	.0065	4.5
50	.0058	3.8
70	.0062	4.0
100	.0145	9.4

Table 1 and figure 4 make it clear that eq (1), together with the listed constants, provides a satisfactory interpolation formula, and the errors introduced by its use are small relative to the possible systematic errors of measurement (see section 5). The values given in tables 2 and 3 were calculated from eq (1) by SEAC.

Table 2 gives the speed of sound in meters per second for each degree C from 0 to 100, and table 3 gives the speed of sound in feet per second at intervals of 2 deg F from 32° to 212°. In each case, the differences, which are listed for convenience in interpolation, were calculated from a table having more significant figures, so that on account of rounding-off errors, the tabulated differences in some cases differ by one unit in the last decimal place from the differences of the tabulated values of c. It is believed (see section 5) that the systematic errors do not exceed 1 part in 30,000. The tables should, therefore, be used in the following manner. In table 2, linear interpolation should be performed to the nearest 0.01 m/s and the final result rounded off to the nearest 0.1 m/s. The error will then not exceed one-half unit in the last place, i. e., 0.05 m/s. Linear interpolation in table 3 will yield errors that do not exceed 2 units (0.2 fps) in the last place.

5. Discussion

Following is a list of the known possible sources of error and an estimate of the upper limit of each error.

5.1. Frequency

As already stated, the frequency was measured by counting cycles for 10 sec; the total count was about 75,000. The inherent error is ±1 count, but in all cases the mode of at least three independent readings, of which, at worst, two were the same and the third different by one, was taken as the observed value. The counting error can thus be as great as 1 part in 75,000, but as it is random, the effect on the final results is negligible, as indicated in section 4. The 10-sec time base was obtained by division from a 1-Mc crystal oscillator which is stable to 2 parts in 10^7 per week, and which was compared with signals from WWV or from a local precision standard. The errors due to inaccuracies in the time base are, therefore, also negligible.

5.2. Length of Path

The length of the tank across its polished ends at 20° C was determined within 1μ, i. e., 5 ppm. Thermal expansion measurements were made at 20°, 60°, and 100° C; the lengths at intermediate temperatures were calculated by quadratic interpolation. The maximum absolute error in the thermal expansion coefficient is estimated at 0.2 ppm; this accumulates to 4 ppm at 0° C, and to 16 ppm at 100° C.

TABLE 2. *Speed of sound in water, metric units*

T	c	Δ	T	c	Δ	T	c	Δ	T	c	Δ
°C	m/s	m/s	°C	m/s	m/s	°C	m/s	m/s	°C	m/s	m/s
	1,400+			1,400+			1,500+			1,500+	
	2.74		25	97.00	2.71	50	42.87	1.12	75	55.45	−0.01
0	7.71	4.97	26	99.64	2.64	51	43.93	1.07	76	55.40	−.05
1	12.57	4.86	27	*2.20	2.56	52	44.95	1.02	77	55.31	−.09
2	17.32	4.75	28	4.68	2.49	53	45.92	0.97	78	55.18	−.13
3	21.96	4.64	29	7.10	2.41	54	46.83	.92	79	55.02	−.17
4	26.50	4.53	30	9.44	2.34	55	47.70	.87	80	54.81	−.20
5	30.92	4.43	31	11.71	2.27	56	48.51	.82	81	54.57	−.24
6	35.24	4.32	32	13.91	2.20	57	49.28	.77	82	54.30	−.28
7	39.46	4.22	33	16.05	2.14	58	50.00	.72	83	53.98	−.31
8	43.58	4.12	34	18.12	2.07	59	50.68	.67	84	53.63	−.35
9	47.59	4.02	35	20.12	2.00	60	51.30	.63	85	53.25	−.39
10	51.51	3.92	36	22.06	1.94	61	51.88	.58	86	52.82	−.42
11	55.34	3.82	37	23.93	1.87	62	52.42	.53	87	52.37	−.46
12	59.07	3.73	38	25.74	1.81	63	52.91	.49	88	51.88	−.49
13	62.70	3.64	39	27.49	1.75	64	53.35	.45	89	51.35	−.52
14	66.25	3.55	40	29.18	1.69	65	53.76	.40	90	50.79	−.56
15	69.70	3.46	41	30.80	1.63	66	54.11	.36	91	50.20	−.59
16	73.07	3.37	42	32.37	1.57	67	54.43	.31	92	49.58	−.63
17	76.35	3.28	43	33.88	1.51	68	54.70	.27	93	48.92	−.66
18	79.55	3.19	44	35.33	1.45	69	54.93	.23	94	48.23	−.69
19	82.66	3.11	45	36.72	1.39	70	55.12	.19	95	47.50	−.72
20	85.69	3.03	46	38.06	1.34	71	55.27	.15	96	46.75	−.76
21	88.63	2.95	47	39.34	1.28	72	55.37	.11	97	45.96	−.79
22	91.50	2.87	48	40.57	1.23	73	55.44	.07	98	45.14	−.82
23	94.29	2.79	49	41.74	1.17	74	55.47	.03	99	44.29	−.85
24	97.00	2.71	50	42.87	1.12	75	55.45	−.01	100	43.41	−.88
25	1,400+			1,500+			1,500+			1,500+	

TABLE 3. *Speed of sound in water, English units*

T	c	Δ	T	c	Δ	T	c	Δ	T	c	Δ
°F	fps	fps	°F	fps	fps	°F	fps	fps	°F	fps	fps
	4,600+			4,900+			5,000+			5,000+	
30	-------	-------	80	25.7	9.4	130	76.2	3.3	180	99.2	−1.0
32	2.1	-------	82	34.8	9.1	132	79.2	3.1	182	98.0	−1.2
34	20.3	18.1	84	43.7	8.8	134	82.1	2.9	184	96.7	−1.3
36	37.9	17.7	86	52.2	8.6	136	84.8	2.7	186	95.2	−1.5
38	55.1	17.2	88	60.5	8.3	138	87.3	2.5	188	93.6	−1.6
40	71.9	16.8	90	68.5	8.0	140	89.6	2.3	190	91.8	−1.8
42	88.2	16.3	92	76.2	7.7	142	91.7	2.1	192	89.9	−1.9
44	104.1	15.9	94	83.6	7.4	144	93.6	1.9	194	87.9	−2.1
46	119.6	15.5	96	90.8	7.2	146	95.3	1.7	196	85.7	−2.2
48	134.6	15.1	98	97.7	6.9	148	96.9	1.6	198	83.4	−2.3
50	149.3	14.7	100	*4.4	6.7	150	98.3	1.4	200	81.0	−2.5
52	163.6	14.3	102	10.8	6.4	152	99.5	1.2	202	78.4	−2.6
54	177.5	13.9	104	17.0	6.2	154	100.5	1.0	204	75.7	−2.7
56	191.0	13.5	106	22.9	5.9	156	101.4	0.9	206	72.9	−2.8
58	*4.1	13.1	108	28.6	5.7	158	102.1	.7	208	70.0	−3.0
60	16.9	12.8	110	34.0	5.4	160	102.6	.6	210	66.9	−3.1
62	29.3	12.4	112	39.2	5.2	162	103.0	.4	212	63.7	−3.2
64	41.3	12.0	114	44.2	5.0	164	103.2	.2	-------	-------	-------
66	53.0	11.7	116	48.9	4.8	166	103.2	.0	-------	-------	-------
68	64.4	11.4	118	53.5	4.5	168	103.1	−.1	-------	-------	-------
70	75.4	11.0	120	57.8	4.3	170	102.8	−.3	-------	-------	-------
72	86.1	10.7	122	61.9	4.1	172	102.4	−.4	-------	-------	-------
74	96.4	10.4	124	65.8	3.9	174	101.8	−.6	-------	-------	-------
76	106.5	10.1	126	69.4	3.7	176	101.1	−.8	-------	-------	-------
78	116.2	9.8	128	72.9	3.5	178	100.2	−.9	-------	-------	-------
80	125.7	9.4	130	76.2	3.3	180	99.2	−1.0	-------	-------	-------
	4,800+			5,000+			5,000+			5,000+	

Thus, the total uncertainty in the length of the tank is about 5 ppm at 20° C, and increases with temperature both ways; at 0° C it becomes about 9 ppm and at 100° C, about 21 ppm.

The question arises as to how closely the length of the sound path in the sample, i. e., the distance between the inner faces of the transducers, approximates to the length of the tank across the ends to which the crystals are wrung. Experience with developmental models showed that unless the assembly were very carefully made, with particular attention to avoidance of clamping pressure too near the unsupported areas of the crystals, the crystals might deflect enough to cause very sizable errors. The present design makes it possible to disassemble and reassemble the delay line repeatedly without affecting the result by a detectable amount; this holds true when the crystals normally used, which are 0.8 mm thick, are replaced by crystals 1.6 mm thick. It, therefore, appears that errors produced by misplacement or deformation of the crystals are insignificant.

5.3. Setting the Coincidence

As explained in section 2, it is believed that no measurable error is introduced by the technique of maximization of the second half cycle of the received pulse. However, a word should be said about the effect of personal bias on the part of the operator. The operators report, to varying degrees, tendencies to adjust not only for maximum height of peak, but also for maximum symmetry and sharpness of peak. Long experiment has convinced us that any of the three criteria lead to sensibly the same result, so that although different operators weigh the three criteria differently, they reproduce each other's settings so well that the discrepancies are negligible relative to other sources of error. The assumption is implicit that the errors of bias do not much exceed the discrepancies among individuals.

5.4. Temperature

The Mueller bridge with which the resistance of the platinum thermometer was measured has a least count of 0.0001 ohm corresponding, for a 25-ohm thermometer, to about 0.001° C. The bridge was calibrated internally so that the indicated resistance in terms of the internal standard is correct to about 0.0002 ohm aside from temperature effects and slow drifts in the arm ratio and in the zero. Allowing for these, it is estimated that the bridge error does not exceed 0.005° C; errors in the calibration of the platinum thermometer itself and those due to heating by the bridge current are much smaller. More important is the error that arises from thermal gradients in the bath. On the assumption that this does not exceed half the reading of the differential thermocouple which, it will be recalled, measures the difference between the temperature of the platinum element and that of the sample, an upper limit to the corresponding uncertainty in the speed of sound, c, was calculated at various temperatures from the known thermal coefficient of c. This upper limit is zero at 74° C, where c is stationary and increases steadily in both directions, reaching about 25 ppm at 0° C, and about 14 ppm at 100° C.

5.5. Purity of Sample

Because the results obtained on ordinary laboratory distilled water were indistinguishable from those obtained on the same water redistilled in vacuum directly into the apparatus, it is felt that the remaining impurities do not have a measurable effect. Several measurements made on local tap water gave results about 30 ppm higher than for distilled water.

5.6. Over-all Accuracy

From the foregoing discussion it appears that the major sources of error are the uncertainties in the length of the path and in the temperature. Both of these are temperature dependent; their sum is an upper limit to the total error. This is about 35 ppm at 0° C; it falls to 15 ppm at 40° C and is almost constant at this value out to 70° C, and rises to about 35 ppm at 100° C. It is upon these considerations that the recommendations for the use of the tables in section 4 are based.

The values of c here reported are lower than those of most other workers, in particular the value at 30° C is about 0.4 m/s below that of Del Grosso, Smura, and Fougere [3], whose work with the ultrasonic interferometer is perhaps the most carefully planned, executed, and analyzed work of this type to date. It was, therefore, felt desirable to perform an independent experiment using an apparatus and a method as different as possible from those of both Del Grosso, et al., and ourselves. An apparatus was constructed with which it is possible to measure, as a function of distance, the phase on the axis of a beam of progressive waves emitted by a small piston-like radiator. If the wave were plane, the phase φ would vary linearly with distance x, and the phase speed c would be $2\pi fx/\varphi$ where f is frequency. In the present case, the wave is not plane and the slope of the curve $2\pi fx$ versus φ depends on x and on the geometry of the arrangement. However, the theory enables us to select a distance x_0 of the receiver from the source such that for $x > x_0$ the departure of $2\pi f dx/d\varphi$ from c is as small as desired.

Five runs were made in distilled water at temperatures between 15° and 25° C. The principal uncertainties are thought to be first, one of about 40 ppm corresponding to a possible error of 0.01° C in the temperature, and second, one of about 56 ppm related directly to the inaccuracies of the screw with which the receiver displacement was measured. These are independent. However, in the worst case of the 5, the result differed from the value gotten from table 2 by only 27 ppm. The value of Del Grosso, et al. [3] disagrees with that of table 2 by 272 ppm.

This work will be reported in detail elsewhere.

The authors are grateful to the personnel of the Engineering Metrology Section and of the Length Section, in whose Laboratories the length of the tank and its thermal expansion, respectively, were measured. Thanks are particularly due to Joseph M. Cameron of the Statistical Engineering Section who advised the authors on problems of data processing, and who performed the curve-fitting computations on SEAC.

6. References

[1] Martin Greenspan and Carroll E. Tschiegg, Sing-around ultrasonic velocimeter for liquids, Rev. Sci. Instr. (in press).

[2] R. A. McConnell and W. F. Mruk, Microacoustic interferometer using 30 Mc pulses, J. Acoust. Soc. Amer. **27**, 672 (1955).

[3] V. A. Del Grosso, E. J. Smura, and P. F. Fougere, Accuracy of ultrasonic interferometer determinations, NRL Report 4439, Naval Research Laboratory, Washington, D. C. (Dec. 6, 1954).

[4] Martin Greenspan and Carroll E. Tschiegg, Effect of dissolved air on the speed of sound in water, J. Acoust. Soc. Amer. **28**, 501 (1956).

Washington, March 27, 1957.

Journal of Research of the National Bureau of Standards Vol. 59, No. 4, October 1957 Research Paper 2796

Pattern of a Flush-Mounted Microwave Antenna

James R. Wait

The numerical results for the far zone radiation from an axial slot on a circular cylinder of perfect conductivity and infinite length are discussed. It is shown that the results for large diameter cylinders can be expressed in a universal form that is suitable for pattern calculations for arrays of slots on a gently curved surface. The work is compared with a related diffraction problem considered by Fock.

1. Introduction

The radiation from flush-mounted microwave antennas has aroused considerable interest in recent years [1−6].[1] From a theoretical standpoint the problem would seem to be simple enough; the surface on which the antenna is mounted is considered to be adequately represented by a sphere or cylinder whose radius of curvature is matched to that of the local curvature of the actual surface. Unfortunately, the formal solution of the problem, in terms of the classical harmonic series involving integral or half-integral order Bessel functions, always converges very poorly when the radius of curvature is large compared to the wavelength. There are two well-known alternative representations [6, 7], however, which can be used to advantage in certain cases. In the illuminated region of the antenna, geometrical optics is most satisfactory, while deep in the shadow the rigorous harmonic series can be converted into the rapidly converging residue series.

The calculation of the radiation field of a flush-mounted antenna in the tangent plane (the classical light-shadow boundary) is not readily treated by either geometrical optics or the residue series. In the former case the field is indeterminant, and in the latter case the convergence is extremely poor and would actually diverge in the illuminated region. Despite the fact that the harmonic series is cumbersome, it is valid in this transition zone between the illuminated and shadow regions of space. Therefore, it is desirable to attempt to adapt the harmonic-series representation to surfaces of large radius of curvature. This is the purpose of the present paper.

2. Theoretical Basis

A thin axial slot, cut on a circular cylinder of infinite length and perfect conductivity is considered because it gives rise to a plane-polarized radiation field. The cylinder is taken to be of radius a and coaxial with a cylindrical coordinate system (ρ,ϕ,z). The slot that extends from z_1 to z_2 at $\phi=0$, has a voltage distribution $V(z)$ throughout its length. The radiation pattern is best expressed in terms of spherical coordinates (r,ϕ,θ) where $\theta=0$ corresponds to the axis of the cylinder. It has been shown [9] that the electric field, which has only a ϕ component, is given by

$$E_\phi=\frac{e^{-ikr}}{r}S(\theta)M(x,\phi), \tag{1}$$

where

$$S(\theta)=\frac{k\sin\theta}{2\pi}\int_{z_1}^{z_2}V(z)e^{ikz\cos\theta}dz, \tag{2}$$

$$M(x,\phi)=\frac{1}{\pi x}\sum_{m=0}^{\infty}\frac{\epsilon_m e^{im\pi/2}\cos m\phi}{H_m^{(2)\prime}(x)}, \tag{3}$$

$x=ka\sin\theta$, $k=2\pi/\text{free space wavelength}$, $\epsilon_0=1,\epsilon_m=2(m\neq 0)$, and $H_m^{(2)\prime}(x)$ is the derivative of the Hankel function appropriate for a time factor $\exp(i\omega t)$. Equation (1) is valid for $kr\sin\theta\gg 1$.

The function $S(\theta)$ is the space factor of the slot, or an array of collinear slots if they were cut in an infinite plane conducting sheet. The function $M(x,\phi)$ is called the "cylinder space factor" as it fully describes the effect of the finite diameter of the cylinder on the radiation pattern in both the θ and ϕ directions. For purposes of computation, it is written

$$M(x,\phi)=|M(x,\phi)|e^{i\alpha(x,\phi)}. \tag{4}$$

The phase function $\alpha(x,\phi)$ is a rapidly varying function of ϕ for the larger x values. For this reason, it is desirable to express α in the illuminated region $(0<|\phi|<\pi/2)$ as a geometrical-optical term plus a correction factor $\Delta(x,\phi)$, as follows [9]

$$\alpha(x,\phi)=\alpha(x,0)-x(1-\cos\phi)+\Delta(x,\phi). \tag{5a}$$

In the shadow region $(\pi/2<|\phi|<\pi)$, it is desirable to express α as a physical-optical term plus a correction, which is also designated $\Delta(x,\phi)$, in the following manner.

$$\alpha(x,\phi)=\alpha(x,\pi/2)+(\pi/2-\phi)x+\Delta(x,\phi). \tag{5b}$$

The amplitude $|M(x,\phi)|$ and the phase correction $\Delta(x,\phi)$ of the cylinder space factor are shown plotted in figures 1 and 2 for ϕ from 0 to 180° for $x=10$, 12, 15, 18, and 21. To prevent troublesome overlapping, the ordinates are shifted for each curve by a constant amount.

[1] Figures in brackets indicate the literature references at the end of this paper.

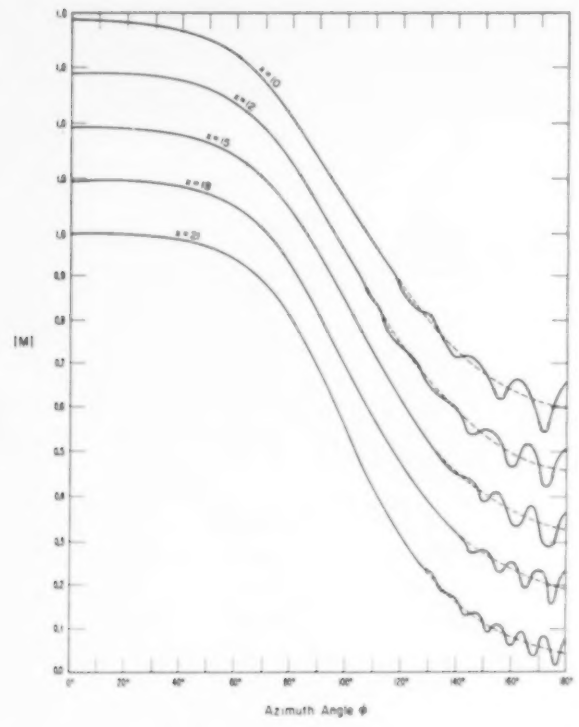

FIGURE 1. *Amplitude of cylinder space factor for narrow axial slot.*

N. B. vertical scale is shifted for each curve.

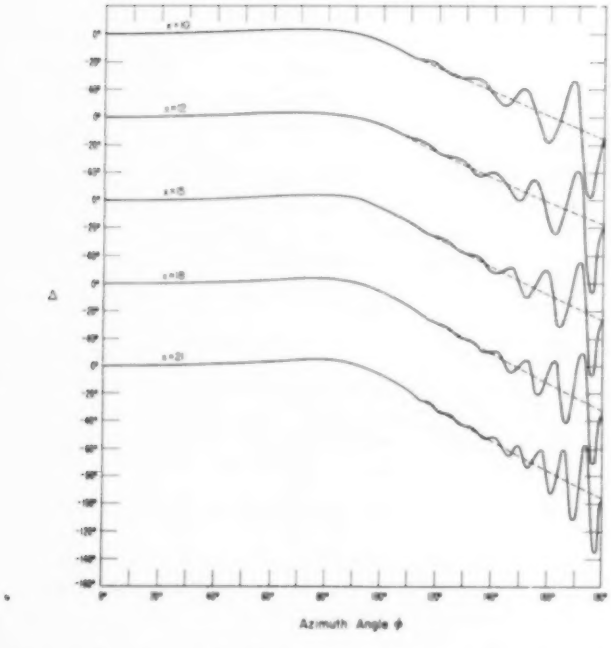

FIGURE 2. *Phase of cylinder space factor for narrow axial slot.*

N. B. vertical scale is shifted for each curve.

For $|\phi|<90°$ but not near 90°, the value of the space factor is quite well approximated by the geometrical-optics approximation. That is

$$\Delta(x,\phi)\cong 0$$

and

$$|M(x,\phi)|\cong 1$$

Deep in the shadow, that is $|\phi|>90°$ but not near 90°, $M(x,\phi)$ has the form of a damped standing wave, and can be characterized by a function of the form

$$A(\phi-\pi/2)e^{-ix(\phi-\pi/2)}+A(3\pi/2-\phi)e^{-ix\left(\frac{3\pi}{2}-\phi\right)}$$

where

$$A(\beta)\cong\exp\left[-i\tau(\pi a/\lambda)^{1/3}\,\beta\right]$$

with $\tau=0.808\,\exp(-i\pi/3)$. This exponential form for $A(\phi)$ is the first term of a rather complicated residue series [7]. It is only valid for $ka\gg 1$. The higher order terms (higher modes) are also parametric in $(\pi a/\lambda)^{1/3}\beta$, where β is some angular distance. It is, therefore, logical to expect $M(x,\phi)$ to be parametric in $(x/2)^{1/3}(\phi-\pi/2)$ and $(x/2)^{1/3}[(3\pi/2)-\phi]$. In fact, if the ripples are ignored, the function $M(x,\phi)$ should be a function only of $(x/2)^{1/3}(\phi-\pi/2)$. The dotted curves in figures 1 and 2 are believed to be the appropriate form of $M(x,\phi)$ when the standing-wave effect, due to the interfering traveling wave from the other side of the cylinder, is removed. These "smoothed" curves are then replotted as a function of X, where $X=(x/2)^{1/3}(\phi-\pi/2)$. The results are shown in figure 3a where both the values of amplitude $|M(X)|$ and the phase correction $\Delta(X)$ for $x=10$, 12, 15, 18 and 21 fall on the same set of curves for the range of X indicated. The amplitude is also shown in figure 3b, being plotted on a log scale.

Having the space factor for the cylinder plotted in this universal form suggests that one may extrapolate the results to larger values of x. This concept, embodied in presenting the results in terms of a parameter X, is not unrelated to the notion of angular distance that has been successfully employed in the representation of field strengths of a transmitter at large ranges over a spherical earth [10]. In the latter instance, the angular distance is defined as the angle subtended at the center of the earth between the horizons of transmitting and receiving antennas. In the present situation, the angular distance is $\phi-\pi/2$ since the source antenna is on the cylinder and the observer is at infinity.

While the present problem is concerned directly with the radiation of an axial slot on a circular cylinder, there is a direct application of the results to the reciprocal case where a plane wave is incident on the cylinder (the E vector is to be perpendicular to the cylinder axis). Then it is possible to regard $M(x,\theta)$ as being proportional to the surface current excited on the cylinder. In other words, the axial slot can be regarded as a receiving antenna and the source is taken to be at infinity.

In view of the reciprocal nature of the problem, it is desirable to compare the present results with those

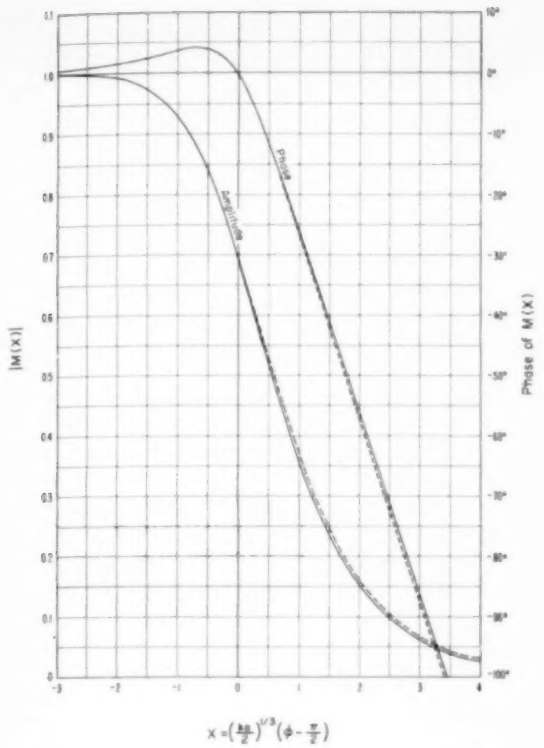

FIGURE 3a. *Amplitude and phase of space factor in parametric form.*

——From circular cylinder data; ..... from Fock.

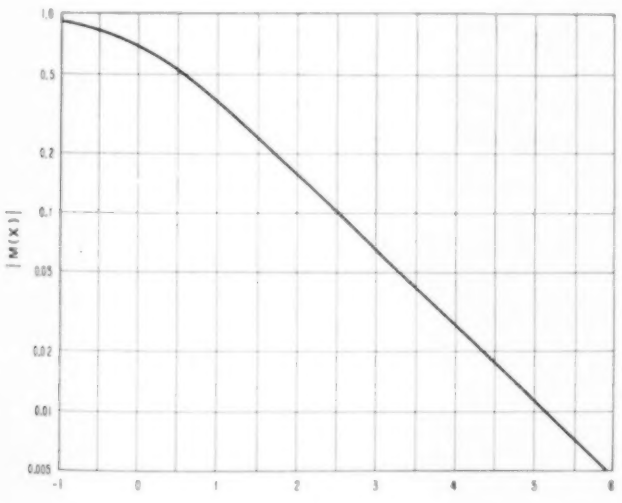

FIGURE 3b. *Amplitude of space factor in parametric form.*

From Circular - cylinder data.

of Fock [11] for the currents excited on a curved surface by an incident plane wave. Fock first considers the diffraction of plane wave by a paraboloid and, in particular, focuses his attention on the tangential magnetic field in the penumbral region (near the boundary of light and shadow). Then, after postulating that the surface currents are only dependent on the local radius of curvature, he obtains a representation for the current distribution that is only dependent on the parameter l/d where l is the distance from the light-shadow boundary and d is the width of the penumbral region. Fock then believes that his results are reasonably valid for any shaped bodies so long as the radius of curvature is always very large compared to the wavelength. As a crucial test of Fock's approximate formula, his results are plotted in figure 3a along with the cylinder computed data. The agreement is very good. There appears to be a slight discrepancy for larger positive X values which is not entirely unexpected because some of Fock's restrictions are becoming violated. Nevertheless, considerable justification is given to the validity of the extrapolation of the cylinder curves to larger values of x.

3. An Application

An interesting application of the foregoing theory is the calculation of the pattern of an end-fire array, of slots on a gently curved surface. For example consider the array of $2N+1$ parallel and axial slots on a cylindrical surface of radius a indicated in figure 4. The angle Φ defines the direction of the observer

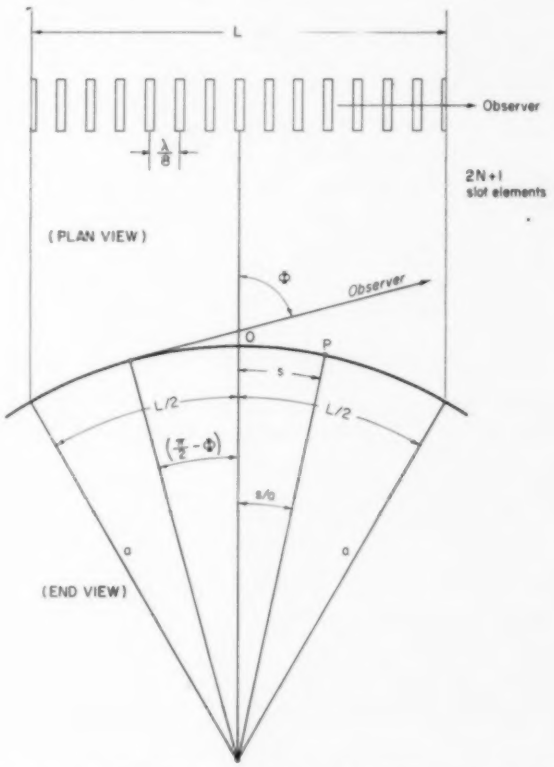

FIGURE 4. *Schematic diagram of end-fire array of slots on a curved conducting surface.*

with respect to the normal at 0, the center of the array. The array and the observer are taken to be in the principal plane (i. e., the plane of the paper). s is the distance from 0, measured along the cylinder surface, to P, the location of any one of the elements. The field due to the source at P is then proportional to

$$e^{iky}K(s)A(s)$$

where $K(s)$ is the relative strength of the element, y is the projection of s on the ray from 0 to the observer and $A(s)$ is the correction factor to geometrical optics. In terms of the function M, $A(s)$ is given by

$$A(s)=M(X) \text{ for } X\leqq 0, \tag{6a}$$

$$\cong M(X)e^{-i\frac{X^3}{3}} \text{ for } X\geqq 0, \tag{6b}$$

where

$$X=-\left[\left(\frac{\pi}{2}-\Phi\right)+\frac{s}{a}\right]\left(\frac{ka}{2}\right)^{1/3}.$$

The factor y is given by $y=c\sin[\Phi-(s/2a)]$ when c is the chord length OP and because

$$c=\left[2a^2\left(1-\cos\frac{s}{a}\right)\right]^{1/2}\cong s\left(1-\frac{s^2}{24a^2}\right), \tag{7a}$$

it follows that

$$y\cong s\left(1-\frac{s^2}{24a^2}\right)\sin\left(\Phi-\frac{s}{2a}\right) \tag{7b}$$

subject to $s<<a$.

Remembering that there are $2N+1$ elements spaced at intervals Δs, it is seen that

$$2N\times\Delta s=L$$

where L is the length of the array. The source is now written

$$K(s)=e^{-\Gamma s}$$

where Γ is the propagation constant of the exciting wave along the array. For the present purpose

$$\Gamma=+imk,$$

where m is a constant real number.

The total field of the array is now proportional to

$$\sum_{n=-N}^{N}e^{iky}e^{-ikms}A(s)$$

where $s=n\cdot\Delta s$ with $n=-N,\ -N+1,\ \ldots\ -1,\ 0,\ 1,\ 2\ \ldots\ N-1,\ N$. Introducing dimensionless parameters, defined by

$$\Delta S=k\Delta s \text{ and } S=n\Delta S$$

it follows that the pattern $T(\Phi)$ of the array is given by

$$T(\Phi)=\sum_{n=-N}^{N}e^{i[Y(S)-mS]}A(X), \tag{8a}$$

where

$$Y(S)=S\left(1-\frac{S^2}{24(ka)^2}\right)\sin\left(\Phi-\frac{S}{2(ka)}\right) \tag{8b}$$

and

$$X=-\left[\left(\frac{\pi}{2}-\Phi\right)+\frac{S}{ka}\right]\left[\frac{ka}{2}\right]^{1/3}. \tag{8c}$$

When ka tends to infinity such that the surface is effectively flat, the pattern becomes

$$T(\Phi)=T_0(\Phi)=\sum_{n=-N}^{N}e^{i[Y(S)-mS]}, \tag{9a}$$

where $Y(S)=S\sin\Phi$ and since $S=n\cdot\Delta S$,

$$T_0(\Phi)=\frac{e^{-iNK}(1-e^{i(2N+1)K})}{1-e^{iK}} \tag{9b}$$

where $K=\Delta S[\sin\Phi-m]$.

According to the analysis of Hansen and Woodyard [12], the maximum gain in the end-fire direction (i. e., $\Phi=90°$) is obtained when $m\cong(N+2)/N$. Then, taking the electrical spacing between the elements as 45° or $\Delta S=\pi/4$, the array has 65 elements, $N=32$ and the total length of the array is 8 wavelengths. The pattern $T_0(\Phi)$ in this case is only defined for the region $-90°<\Phi<90°$. The main lobe and the first side lobe are shown plotted in figure 5 normalized such that the maximum field is 0 db. Using the same values of N and ΔS, the corresponding pattern $T(\Phi)$ is plotted for $ka=200$. The main lobe is seen to be somewhat changed in

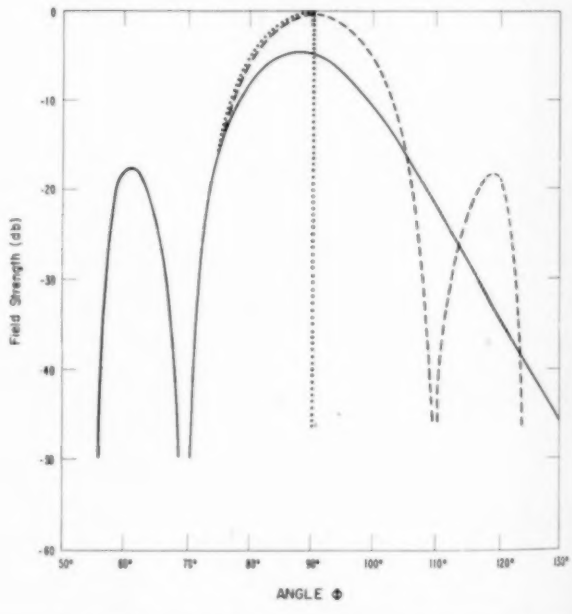

FIGURE 5. *Pattern of end-fire array of slots on a curved surface.*

..... $ka=\infty$; ——— $ka=200$; — — — $ka=200$, $A(X)=1$; array length=8λ; number of elements=65.

form, particularly in the directions near $\Phi=90°$ which is the tangent plane of the center of the array. The decibel level of the field in the diffraction zone ($\Phi>90°$) is seen to decrease linearly with angle. There are no lobes formed in this region. It is of interest to know how the curvature of the array itself would modify the pattern. Therefore, for sake of comparison, the pattern $T(\Phi)$ of the end-fire array of isolated elements on a circular arc ($ka=200$) is also plotted in figure 5. The working formula here is identical to equation (8a) with $A(X)$ being replaced by 1 because diffraction effects are no longer present. The pattern is almost identical to that for an end-fire array where elements are on a straight line. Lobes, in this case, are formed on both sides of the main beam although they are not quite symmetrical about it.

The pattern $T(\Phi)$ is also computed for $ka=100$, and is shown plotted in figure 6 along with the curve for $ka=\infty$ and the curved array of isolated elements.

It would seem that an end-fire array of slots on a curved surface has some rather interesting properties. The main effects of the non-flatness of the surface is to tilt the maximum of the main beam up slightly, and to extend the total width of the main beam into the shadow region. There is no evidence of lobes on this side of the beam, although at large angles (Φ approaching 180°), there is the possibility that the back lobe from the end-fire array could creep around the surface in the other direction and form lobes. This effect from a practical standpoint, however, is completely insignificant for $ka>100$.

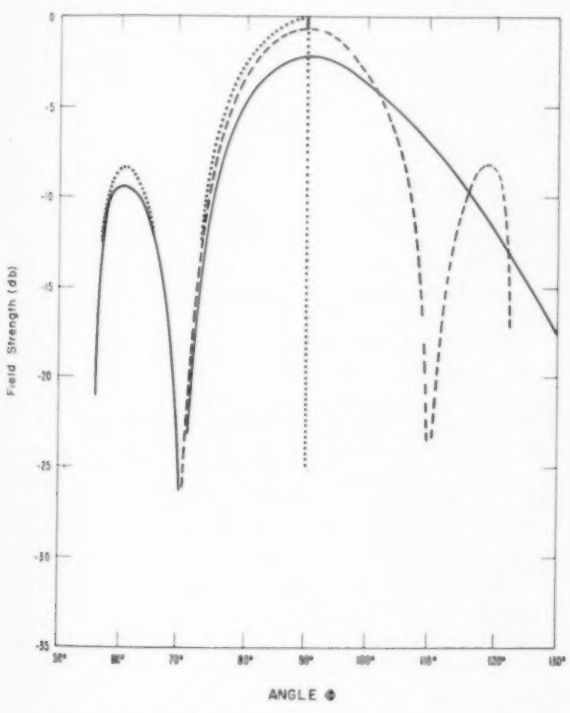

FIGURE 6. *Pattern of end-fire array of slots on a curved surface.*

..... $ka=\infty$; ——— $ka=100$; — — — $ka=100$, $A(X)=1$; array length=8λ; number of elements=65.

4. Concluding Remarks

It is seen that the radiation pattern of a flush-mounted antenna is influenced, to a considerable extent, by the radius of curvature of the surface on which it is mounted. In most cases, the main beam is tilted upward away from the surface, although the total width of the beam can be broadened into the shadow. Similar phenomena had been observed in the calculated patterns of slots on a conducting half-plane [13]. It would appear that any attempt to reduce the side lobes of an end-fire array by using a diffracting edge or surface will lead to a broadening of the main beam. It is also quite apparent that the resultant pattern of a flush mounted antenna is not simply obtained by multiplying the free space pattern by the pattern of a single slot on the curved surface. Such a process would produce a pattern with lobes in the diffraction or shadow region which do not exist in reality for a nonclosed surface. Furthermore, this "multiplication" technique would not predict the broadening of the beam in the tangent plane.

The author thanks William Briggs for his assistance in the calculation of the patterns in figures 5 and 6.

5. References

[1] G. Sinclair, The patterns of slotted cylinder antennas, Proc. I. R. E., **36,** 1487 (1948).
[2] C. H. Papas, Radiation from a transverse slot in an infinite cylinder, J. Math. and Phys. **28,** 227 (1950).
[3] C. Silver and W. K. Saunders, Radiation from a transverse slot in a circular cylinder, J. Appl. Phys. **21,** 749 (1950).
[4] S. Sensiper, W. G. Sterns, and T. T. Taylor, A further study of the patterns of single slots on circular conducting cylinders, paper presented at Spring International Scientific Radio Union (U. R. S. I.) Meeting (April 24, 1951).
[5] J. R. Wait and S. Kahana, Calculated patterns of circumferential slots on a circular conducting cylinder, Can. J. Technol. **33,** 77 (1955).
[6] L. L. Baillin, The radiation field produced by a slot in large circular cylinder, Trans. P. G. A. P. (Institute of Radio Engineers) **3,** 128 (1955).
[7] G. N. Watson, The diffraction of radio waves by the earth, Proc. Roy. Soc. **95,** 546 (1919).
[8] H. Bremmer, Terrestrial radio waves, theory of propagation, chapter 3 (Elsevier Publishing Co., Amsterdam, 1949).
[9] J. R. Wait, Radiation characteristics of axial slots on a conducting cylinder, Wireless Engr. **32,** 316 (1955).
[10] K. A. Norton, P. L. Rice, and L. E. Vogler, The use of angular distance in estimating transmission loss, Proc. I. R. E. **43,** 1488 (1955).
[11] V. Fock, The field of a plane wave near the surface of a conducting body, J. Phys. (U. S. S. R.) **10,** 399 (1946).
[12] W. W. Hansen and J. R. Woodyard, A new principle in directional antenna design, Proc. I. R. E. **26,** 333 (1938).
[13] J. R. Wait and R. E. Walpole, Calculated radiation characteristics of slots cut in metal sheets, Can. J. Technol. **33,** 211 (1955).

BOULDER, COLO., March 28, 1957.

Journal of Research of the National Bureau of Standards Vol. 59, No. 4, October 1957 Research Paper 2797

Standards for *p*H Measurements from 60° to 95° C

Vincent E. Bower and Roger G. Bates

The NBS standard *p*H scale is defined in terms of several reference solutions whose *p*H values (pH_S) have heretofore been assigned only in the range 0° to 60° C. Recent measurements of the standard potential of the silver–silver-chloride electrode at temperatures above 60° now permit this scale to be extended to 95° C.

Electromotive-force measurements of cells with hydrogen and silver–silver-chloride electrodes and containing buffer-chloride solutions are reported in this paper for the range 60° to 95° C. The assignment of pH_S values to the following five reference solutions is described: 0.05-*m* potassium tetroxalate; potassium hydrogen tartrate (saturated at 25° C); 0.05-*m* potassium hydrogen phthalate; 0.025-*m* potassium dihydrogen phosphate; 0.025-*m* disodium hydrogen phosphate; and 0.01-*m* borax.

1. Introduction

The Bureau has recommended a standard *p*H scale defined in terms of several reference points. The primary standards which fix the points on this scale are six in number and cover the *p*H range 1.6 to 12.5 at 25° C. Their compositions are as follows: A 0.05-*m* solution of potassium tetroxalate (pH_S 1.68 [1][1]); a solution saturated with potassium hydrogen tartrate at 25° C (pH_S 3.56 [2]); 0.05-*m* potassium hydrogen phthalate (pH_S 4.01 [3]); a solution 0.025-*m* with respect to both potassium dihydrogen phosphate, and disodium hydrogen phosphate (pH_S 6.86 [4]); 0.01-*m* borax (sodium tetraborate, pH_S 9.18 [5]); and a solution saturated with calcium hydroxide at 25° C (pH_S 12.45 [6]).

In earlier published work, the pH_S values of five of these reference standards have been determined at intervals of 5 deg from 0° to 60° C, permitting the standardization of *p*H equipment over a rather wide range of temperatures. At the time when most of these values were obtained, standards at higher temperatures were precluded by a lack of data for the standard potential of the silver–silver-chloride electrode, or other reference electrode, above 60° C. A need on the part of commerce and industry for accurate standards for measuring *p*H at temperatures up to 95° C, however, led the authors to undertake a determination of this important electrode potential in the range 60° to 95° C [7]. The pH_S values of all but one of these standards have now been extended to this high range of temperature. Calcium hydroxide has a negative temperature coefficient of solubility, and a separation of solid material was sometimes observed when a solution saturated at 25° C was heated to temperatures above 60° C. Furthermore, the poor stability of those cells in which precipitation did not occur made precise measurements extremely difficult. For these reasons, pH_S values have not been assigned to the calcium hydroxide standard in this extended temperature range.

[1] Figures in brackets indicate the literature references at the end of this paper.

2. Method of Assigning pH_S

The procedure by which the standard *p*H values have been assigned to the standard reference solutions has been set forth in earlier publications [1 to 6, 8, 9]. There are three steps in the procedure: (1) Measurement of the emf of the cell Pt; H_2(g), standard reference solution, KCl (*m*), AgCl; Ag. This cell contains the reference solution in which a soluble chloride (usually potassium chloride) is present at one of three selected low, accurately known, molalities (*m*). From the emf (*E*), the standard potential of the silver–silver-chloride electrode ($-E°$ [7]), and natural constants, values of the quantity *pw*H are calculated by the formula

$$pw\mathrm{H} \equiv \frac{(E-E°)F}{2.3026RT} + \log m \qquad (1)$$

in which *F* is the faraday, *R* the gas constant, and *T* the temperature on the Kelvin scale; (2) the effect of the added chloride on the value of *pw*H is removed by extrapolation to $m=0$, in order to obtain the limiting value, *pw*H°; (3) the standard *p*H values, termed pH_S, are calculated from *pw*H° and a conventional definition of the activity coefficient of chloride ion, f_{Cl}:

$$pH_S = pw\mathrm{H}° + \log f_{Cl}. \qquad (2)$$

The single ionic activity coefficient, f_{Cl}, is related in some arbitrary manner to mean activity coefficients, which are either experimentally determined or calculated from equations, like that of Debye and Hückel [10], believed to be valid for dilute solutions. For this step it is necessary to know the ionic strength of the solution.

3. Experimental Procedures

In view of the high vapor pressure of water in the cell solutions at these elevated temperatures, each cell vessel was provided with a saturator consisting of three chambers in series [11], in addition to the single saturating chamber that was a part of the vessel itself [12]. The hydrogen gas bubbled through

a total depth of nearly 30 cm of solution before entering the hydrogen electrode compartment of the cell. By this means, vapor-liquid equilibrium was believed to be established at all of the temperatures. The smallest volume of hydrogen sufficient to separate the solution from the rubber stopper holding the electrodes was allowed to remain in the silver–silver-chloride electrode compartment at the time the cell was filled.

The constant temperature bath was filled with a commercial heavy mineral oil of U. S. P. grade. Temperatures were measured with a platinum resistance thermometer, and are believed to have been fixed at the nominal values within $\pm 0.05°$ C. In order to correct the observed emf to 1 atm partial pressure of hydrogen, the vapor pressures of the solutions were taken to be the same as those of pure water. The pressure corrections at 60° to 95° C, in millivolts, have been tabulated elsewhere [9].

The cell solutions were prepared from weighed amounts of the buffer materials (NBS Standard Samples), and from potassium chloride solutions of the desired molality. Dissolved oxygen was removed by bubbling pure hydrogen through the solutions for 2 hr before the cells were filled. Concentrations were expressed on the molal scale (moles per kilogram of water) exclusively, inasmuch as the molality remains unchanged when the temperature of the solution is altered. The dilution effect on the *p*H of these standard solutions is small. Hence, in practice it is permissible to regard the buffer concentrations given in the tables as either *molarities* or *molalities*. The error exceeds 0.001 *p*H unit only for the tetroxalate solution, where it may amount to 0.002 unit.

The preparation of the electrodes has been described elsewhere [9]. The hydrogen electrodes used in the phthalate solutions were coated with palladium black to minimize reduction of the solute. In other details, the procedure followed closely that of the study of hydrochloric acid solutions at 60° to 95° C. [7].

The duration of stability of these cells is considerably reduced at elevated temperatures, particularly when the cell solutions are alkaline. For this reason, the cells were brought to initial equilibrium at room temperature, and the measurements at 60° to 95° C were completed within 8 hr after the temperature of the bath was raised.

4. Results

The measurements were made at three low molalities (m), namely 0.015, 0.010, and 0.005, of potassium chloride. It has been found that the values of pwH for a given buffer solution, computed by eq (1), usually vary linearly with m below $m=0.015$. Although most of the measurements at high temperatures were of insufficient precision to provide an independent test of linearity, nevertheless, a straight line, located by the method of least squares, was drawn through the values of pwH. The intercept of this line

$$pw\mathrm{H} = pw\mathrm{H}^\circ + am \qquad (3)$$

with the axis at $m=0$ is pwH°, and the slope of the line is designated a.

The experimental data, which were rather numerous, are summarized in table 1. In the next to the last column is given the value of σ, the standard deviation of a single "observed" value of pwH from the calculated value, and in the last column is found σ_t, the standard deviation of pwH°, the intercept.

TABLE 1. *Summary of data and calculated values of* pwH°

Reference solution	Temperature	Number of cells for $m_{KCl}=$			Constants of eq (3)		Standard deviations	
		0.005	0.010	0.015	pwH°	a	σ	σ_t
	°C							
0.05-m potassium tetroxalate	60	3	2	2	1.827	0.28	0.003	0.003
	70	3	2	2	1.849	.35	.003	.003
	80	3	2	2	1.877	.34	.002	.002
	90	3	2	2	1.904	.16	.012	.011
	95	3	2	2	1.919	.01	.011	.010
Potassium hydrogen tartrate, saturated at 25° C	60	5	4	2	3.643	−.42	.002	.002
	70	5	4	2	3.664	−.20	.003	.002
	80	5	4	2	3.698	−.60	.002	.002
	90	5	4	2	3.738	−.25	.003	.002
	95	5	4	2	3.767	−1.56	.005	.004
0.05-m potassium hydrogen phthalate	60	6	4	5	4.175	−.05	.005	.003
	70	4	3	3	4.219	−.03	.007	.005
	80	4	3	3	4.250	−.01	.006	.005
	90	4	3	3	4.301	+.01	.006	.005
	95	6	4	5	4.331	.04	.005	.003
0.025-m potassium dihydrogen phosphate, 0.025-m disodium hydrogen phosphate	60	5	4	2	6.948	−.97	.005	.004
	70	5	4	2	6.962	−.64	.004	.003
	80	5	4	2	6.979	−.29	.004	.003
	90	5	4	2	7.001	+.05	.005	.003
	95	5	4	2	7.014	.03	.004	.003
0.01-m borax	60	5	5	3	9.026	.04	.005	.003
	70	5	5	3	8.990	.20	.004	.003
	80	5	5	3	8.953	.90	.003	.002
	90	5	5	3	8.920	1.19	.005	.003
	95	5	5	3	8.899	1.77	.012	.009

5. Calculation of pH_S

Several different conventions for the estimation of the activity coefficient of chloride ion, f_{Cl} in eq (2), have been used in assigning pH_S values to the six NBS standards. Inasmuch as this coefficient has no independent thermodynamic definition, one convention cannot be termed "more correct" than another. In fairness, all of these may be called "reasonable", and it is fortunate that all lead to identical pH values at very low concentrations and to values that differ by only about ± 0.01 unit at an ionic strength of 0.1 [8, 9]. The assignment of pH_S values with an accuracy of ± 0.001 unit must await the universal acceptance of a single convention for the estimation of the individual ionic activity coefficients needed in the evaluation of electrochemical data.

Mean activity coefficients of the electrolytes present in buffer solutions are ordinarily unknown; hence, assumed relationships among the activity coefficients of the ions in these mixtures are not usually a fruitful means of evaluating f_{Cl}. It is just as satisfactory, and more convenient, to estimate f_{Cl} by the Debye-Hückel equation

$$\log f_{Cl} = \frac{-A\sqrt{\mu}}{1+Ba^*\sqrt{\mu}} \qquad (4)$$

where A and B are constants for the water medium at a particular temperature, μ is the ionic strength, and a^* is an "ion-size parameter". When the latter is given a value of 4 to 6, the right side of eq (4) reproduces the logarithm of the mean activity coefficient of many uniunivalent strong electrolytes very successfully.

In order to use eq (4) to calculate pH_S at elevated temperatures, it is necessary to know, within about 10 percent, the ionic strength of the buffer solution at 60° to 95° C. The evaluation was accomplished as follows for the five buffer solutions:

1. 0.05-*m* potassium tetroxalate: in the earlier work [1], the ionic strength of the 0.05-*m* solution was found to be 0.077 at 0° C and 0.074 at 60° C. This change was not only small, but approximately linear; hence, the values of the ionic strength at 60° to 95° C were obtained by extrapolation, and an average value of 0.073 was selected.

2. Potassium hydrogen tartrate, saturated at 25° C: the equation for the calculation of the ionic strength is given in an earlier paper [2]. The ratio of the dissociation constants, K_2/K_1, needed in the calculation, was estimated with the required accuracy from the known ratio in the range 0° to 60° C [13] by extrapolation to the higher temperatures. In this way, it was shown that the ionic strength of the tartrate solution saturated at 25° C is practically constant at 0.04 in the temperature range 25° to 95° C.

3. 0.05-*m* potassium hydrogen phthalate: the ionic strength of this solution between 25° and 60° C was calculated from the compositions listed by Hamer, Pinching, and Acree [3], and found to change only 0.3 percent when the temperature is increased by 35° C. The ionic strengths were plotted, and the curve extended to 95° C. An average value of 0.053 was chosen for the range 60° to 95° C.

4. 0.025-*m* potassium dihydrogen phosphate, 0.025-*m* disodium hydrogen phosphate: inasmuch as negligible amounts of free hydrogen and hydroxyl ions are present in these solutions, the ionic strength is constant at 0.1 from 0° to 95° C.

5. 0.01-*m* borax: the ionic strength is 0.02 and is unchanged by the increased degree of hydrolysis at the elevated temperatures. The formation of polyboric acids is not believed to be sufficiently extensive at this low concentration and relatively high pH to affect the ionic strength appreciably [5].

These values of the ionic strength were used to compute pH_S by eq (2) with the aid of the conventional definition of f_{Cl} embodied in eq (4). The ion-size parameter a^* of the latter equation was given two values, 4 and 6, and the values of pH_S given in table 2 are the mean of the two results to the nearest 0.01 unit. The pH_S of the six NBS standards for all the temperatures at which an assignment of pH_S has been made are plotted in figures 1 and 2, and are included in table 2 for the convenience of the reader.

The reference solutions should be preserved at room temperature, where they are known to be stable for several weeks, and portions heated to the elevated temperatures as needed for the standardization of pH equipment.

TABLE 2. *pH_S of the six reference solutions[a] from 0° to 95° C*

t	0.05-*m* K tetroxalate	KH tartrate, (saturated at 25° C)	0.05-*m* KH phthalate	0.025-*m* KH_2PO_4, 0.025-*m* Na_2HPO_4	0.01-*m* borax	$Ca(OH)_2$, (saturated at 25° C)
0	1.67	----------	4.01	6.98	9.46	13.43
5	1.67	----------	4.01	6.95	9.39	13.21
10	1.67	----------	4.00	6.92	9.33	13.00
15	1.67	----------	4.00	6.90	9.27	12.81
20	1.68	----------	4.00	6.88	9.22	12.63
25	1.68	3.56	4.01	6.86	9.18	12.45
30	1.69	3.55	4.01	6.85	9.14	12.30
35	1.69	3.55	4.02	6.84	9.10	12.14
40	1.70	3.54	4.03	6.84	9.07	11.99
45	1.70	3.55	4.04	6.83	9.04	11.84
50	1.71	3.55	4.06	6.83	9.01	11.70
55	1.72	3.56	4.07	6.84	8.99	11.58
60	1.72	3.56	4.09	6.84	8.96	11.45
70	1.74	3.58	4.12	6.85	8.93	----------
80	1.77	3.61	4.16	6.86	8.89	----------
90	1.80	3.65	4.20	6.88	8.85	----------
95	1.81	3.68	4.23	6.89	8.83	----------

[a] In the preparation of the buffer solutions, it is usually more convenient to dissolve the buffer substance in water and dilute to a given volume in a volumetric flask than to add a known weight of water. As noted above, the pH_S of solutions, whose *molarities* at 25° C are the same numerically as the *molalities* given in table 2, will not differ appreciably from the values listed.

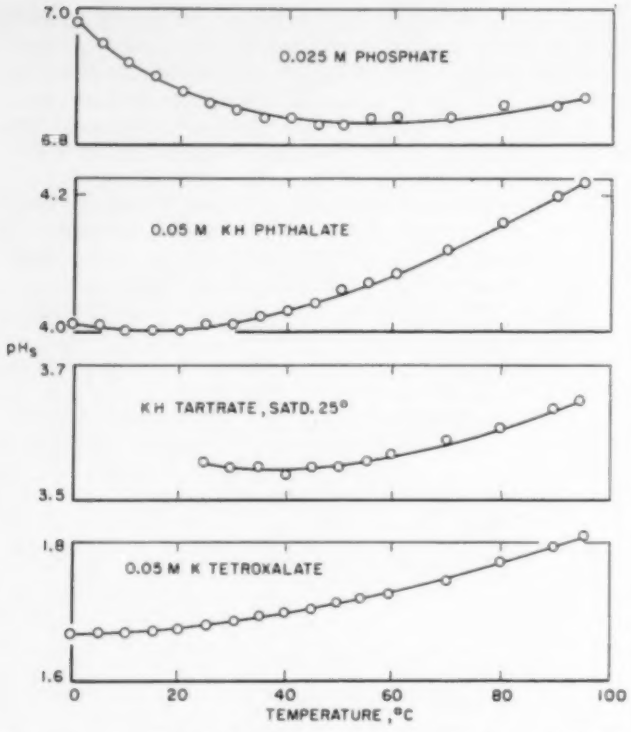

FIGURE 1. *pH_S of the NBS tetroxalate, tartrate, phthalate, and phosphate standards at 0° to 95° C.*

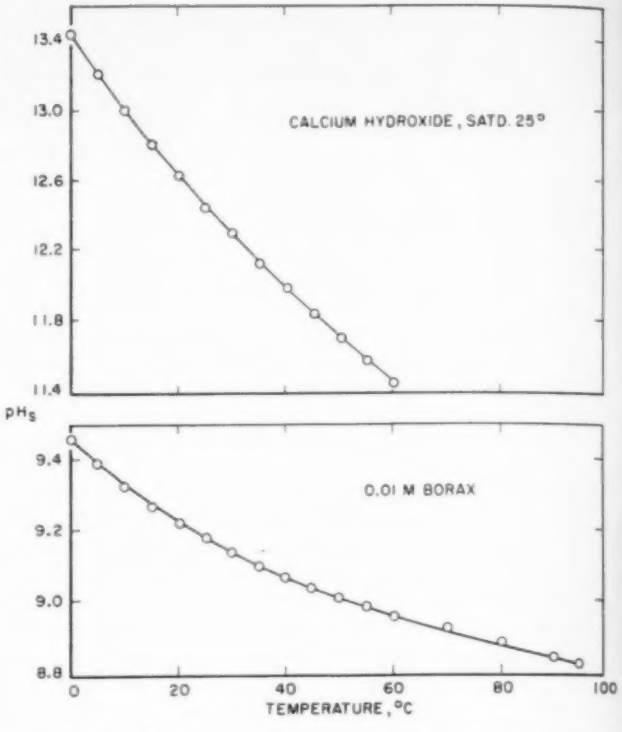

FIGURE 2. *pH_S of the NBS borax and calcium hydroxide standards from 0° to 95° C.*

6. References

[1] V. E. Bower, R. G. Bates, and E. R. Smith, J. Research NBS **51,** 189 (1953) RP2450.
[2] R. G. Bates, V. E. Bower, R. G. Miller, and E. R. Smith, J. Research NBS **47,** 433 (1951) RP2268.
[3] W. J. Hamer, G. D. Pinching, and S. F. Acree, J. Research NBS **36,** 47 (1946) RP1690.
[4] R. G. Bates and S. F. Acree, J. Research NBS **34,** 373 (1945) RP1648.
[5] G. G. Manov, N. J. DeLollis, P. W. Lindvall, and S. F. Acree, J. Research NBS **36,** 543 (1946) RP1721.
[6] R. G. Bates, V. E. Bower, and E. R. Smith, J. Research NBS **56,** 305 (1956) RP2680.
[7] R. G. Bates and V. E. Bower, J. Research NBS **53,** 283 (1954) RP2546.
[8] R. G. Bates, Analyst **77,** 653 (1952).
[9] R. G. Bates, Electrometric *p*H determinations, chapters 4 and 7 (John Wiley & Sons, Inc., New York, N. Y., 1954).
[10] P. Debye and E. Hückel, Physik. Z. **24,** 185 (1923).
[11] R. G. Bates and G. D. Pinching, J. Research NBS **42,** 419 (1949) RP1982.
[12] R. G. Bates and S. F. Acree, J. Research NBS **30,** 129 (1943) RP1524.
[13] R. G. Bates and R. G. Canham, J. Research NBS **47,** 343 (1951) RP2260.

WASHINGTON, April 15, 1957.

Journal of Research of the National Bureau of Standards Vol. 59, No. 4, October 1957 Research Paper 2798

A Numerical Study of Dedekind's Cubic Class Number Formula

Harvey Cohn [1]

In this paper an analytic formula of Dedekind is used to compute class numbers for a sample of pure cubic fields, employing the National Bureau of Standards electronic computer, the SEAC. The computation is one of major magnitude, and it illustrates the usefulness of combining integral and decimal arithmetic. The class numbers obtained are of much greater magnitude than those of pure cubic fields previously studied by means of hand computer methods.

1. Introduction

The discovery of fields with high class numbers [2] has become an end in itself [10].[3] There are generally two possible procedures: One is the *algebraic* method, consisting, operationally, of a certain sorting of values of polynomials according to factors; the second is the *analytic* method, based on zeta-function residues. The second method is of special interest when applicable, because of the scarcity of types of field for which a usable formula emerges.

In 1900, Dedekind applied both methods to the "pure" cubic field, or the field formed by adjoining $M^{1/3}$ to the rationals [4]. The largest class number h that Dedekind achieved was $h=9$ for $M=91$. In 1950, Cassels published a table of class numbers [1] with the larger $h=12$ for $M=43$, using the algebraic method. To achieve a substantially larger h it is necessary to take larger values of M. Furthermore, Dedekind's analytic formula is the simpler method to program for a machine for certain special M, namely, those that equal $(s^3+1)/c^3$ for s and c integers. A sample of 21 cases were run, yielding six class numbers h between 18 and 27, as well as other smaller ones (including the cases cited above).

As an incidental result the quadratic fields (whose relation to the pure cubic field is similar to the relation of rational numbers to the quadratic field) are studied in some numerical detail.

The computation uses a mixture of integral and decimal arithmetic like the earlier work with Gorn [3], but, here, more fortunately, round-off provides no difficulty, even far beyond the range covered. The work was begun about July 1956 and the runs were completed November 1956.

2. Dedekind's Formula

The first algebraic investigations of class number were made by Markoff [8], but the first explicit "closed" formula for class number was derived by Dedekind. The entire numerical study undertaken here stems from his formula, which we give without proof (in an equivalent form):

$$\epsilon^h=\frac{\Pi \mathrm{H}(\omega_N)^{1/6}}{\Pi \mathrm{H}(\omega_R)^{1/6}}. \tag{2.1}$$

Here h is the much desired class number of the real field $R(M^{1/3})$, and $\epsilon(>1)$ is the (often elusive) fundamental unit, which is discussed later. The function $\mathrm{H}(z)$ is defined for z a positive imaginary quantity ($\mathrm{Im}z>0$), as the (positive) function

$$\mathrm{H}(z)=\eta(z)\eta(-\bar{z})[i(\bar{z}-z)]^{1/2}, \tag{2.2}$$

where $\eta(z)$ is the (analytic) Dedekind eta-function [6].

$$\eta(z)=\exp(\pi iz/12)\prod_{n=1}^{\infty}(1-\exp 2\pi izn), \tag{2.3}$$

and $\bar{z}$ denotes the complex conjugate of z. The symbols ω_N, ω_R, are rather complicated and are treated in the next section, but more immediately relevant to the cubic field itself is the following fact: If M is decomposed by positive a, b, c, so that

$$M=ab^2c^3, \tag{2.4}$$

(so that a and b are free of quadratic factors), then $R(M^{1/3})$ is generated equally well by $(ab^2)^{1/3}$ or $(a^2b)^{1/3}$. Hence the number pair (a,b) of relatively prime integers (not both 1) uniquely determines a field $K_{a,b}=R(M^{1/3})$. For this field the conductor k is defined as

$$\left.\begin{aligned} k&=ab & a^2-b^2&\equiv 0 \pmod 9\\ k&=3ab & a^2-b^2&\not\equiv 0 \pmod 9.\end{aligned}\right\} \tag{2.5}$$

As a final definition,

$$D=-3k^2 \tag{2.6}$$

is called the discriminant. Its significance lies in the fact that the algebraic integers, in particular the fundamental unit ϵ, together with the algebraic conjugates ϵ', $\bar{\epsilon}'$ (the complex conjugates) satisfy

$$D\leq|(\epsilon-\epsilon')(\epsilon'-\bar{\epsilon}')(\epsilon-\bar{\epsilon}')|^2. \tag{2.7}$$

[1] Present address, Department of Mathematics, Washington University, St. Louis, Mo.

[2] A general background in algebraic number theory, including quadratic forms is assumed (see [7]).

[3] Figures in brackets indicate the literature references at the end of this paper.

434677—57——3

3. Quadratic Field

Associated with the cubic field in question is the quadratic field generated by adjoining to the rationals the imaginary cube root of unity ρ given by (say) the positive imaginary root of

$$\rho^2+\rho+1=0. \tag{3.1}$$

For this the norm function N is defined by

$$N(p+q\rho)=(p+q\rho)(p+q\rho^2)=p^2-pq+q^2. \tag{3.2}$$

We finally associate with the field $K_{a,b}$ and its conductor k the triples of integers $\{A, B, C\}$, such that

$$AC=k \tag{3.3}$$

$$1\leqq B<A \tag{3.4}$$

$$(A,N(B+C\rho))=1. \tag{3.5}$$

For every such triple of integers we construct the quadratic form

$$Q(x,y)=N[Ax+(B+C\rho)y] \tag{3.6}$$

and consider any prime p, not dividing $3k^2$, represented by $Q(x,y)$ for integral x and y. Then $\{A,B,C\}$ is called a *residue* (or *nonresidue*) triple or $Q(x,y)$ is called a *residue* (or *nonresidue*) form according to whether or not the equation

$$x^3\equiv a^2b \pmod p \tag{3.7}$$

is solvable for an integer x. Then for each triple satisfying eq (3.3), (3.4), or (3.5) a form $Q(x,y)$ is defined with "root"

$$\omega=\frac{B+C\rho}{A}. \tag{3.8}$$

The root ω is an ω_R or an ω_N according as the residue or nonresidue character of the form. The product symbol in eq (2.1) should then be self-explanatory. It can be shown there are $3k''$ triples $\{A,B,C\}$ that generate an ω_R and $6k''$ that generate an ω_N (not all of the ω_R or ω_N being distinct), where $9k''$, the total number of triples, is given by

$$9k''=k\prod_{p/k}(1-(-3/p)/p). \tag{3.9}$$

Here $(-3/p)$ is the usual quadratic residue symbol,

$$(-3/p)=\begin{cases} 1 \text{ for } p\equiv 1 \pmod 3 \\ -1 \text{ for } p\equiv -1 \pmod 3 \\ 0 \text{ for } p\equiv 0 \pmod 3. \end{cases} \tag{3.10}$$

The properties of the quadratic form $Q(x,y)$ will eventually come into play. It might suffice for the time being to mention that the function $H(\omega)$, according to a well-known property of the Dedekind eta-function, is invariant under a unimodular change of variables; thus a unimodular integral change of variables of $Q(x,y)$ will not affect $H(\omega)$; neither will the change $\omega'=-\bar{\omega}$. Thus let $Q(x,y)$ be equivalent to the reduced form

$$Q^*(X,Y)=RX^2+SXY+TY^2. \tag{3.11}$$

Its root may be written

$$\omega^*=\frac{-S+ik\cdot 3^{1/2}}{R},$$

so that

$$0\leqq S/2<R\leqq(-D/3)^{1/2}=k \tag{3.12}$$

because, for all $9k''$ forms corresponding to conductor k,

$$D=-4RT+S^2=-3k^2. \tag{3.13}$$

We are now guaranteed by eq (3.12) a much more favorable scaling for the computation of $H(\omega)$. Thus

$$\left.\begin{aligned} \log H(\omega)&=-\pi k3^{1/2}/(12R)+\sum_{n=1}^{\infty}\log(1-2\kappa^n\cos Sn/R+\kappa^{2n}) \\ \kappa&=\exp(-\pi k3^{1/2}/R), \end{aligned}\right\} \tag{3.14}$$

and $\kappa\leqq\exp(-\pi 3^{1/2})$, so that to the degree of round-off used here, it will develop that no more than five terms of the infinite sum (or product) are necessary, when the reduced form is used for $Q(x,y)$.

4. Units and Choice of Field

We henceforth confine ourselves to fields generated by $M^{1/3}$, where, for a positive or negative integer s,

$$M=s^3+1. \tag{4.1}$$

The advantage is that a very obvious unit is

$$\eta=|-s+M^{1/3}|^{-1}=|s^2+sM^{1/3}+M^{2/3}|, \tag{4.2}$$

where $M^{1/3}$ refers to the real root. A fundamental unit is clearly of the type $\eta^{1/m}$, and the value of m can be ascertained in the sample treated here, by means of well-known results of Dedekind supplemented by the lemma (compare [9]):

LEMMA. In the notation of (2.5), if $k>10s$, then

$$\epsilon=\eta \text{ or } \eta^{1/2}. \tag{4.3}$$

PROOF. Let $\epsilon=\eta^{1/m}$ be the fundamental unit. Then ϵ, as an algebraic number, has a (root) discriminant not less than the discriminant D of $K_{a,b}$. Hence

$$D\leqq|\epsilon-\epsilon'|^2|\epsilon-\bar{\epsilon}'|^2|\epsilon'-\bar{\epsilon}'|^2,$$

where ϵ', $\bar{\epsilon}'$ are the complex conjugate roots belonging to the same equation as ϵ. But $|\epsilon'|=|\bar{\epsilon}'|=\epsilon^{-1/2}$, thus

$$D \leqq (\epsilon+\epsilon^{-1/2})^4(2\epsilon^{-1/2})^2 \leqq 4\epsilon^3(1+\epsilon^{-3/2})^4. \qquad (4.4)$$

But finally, $D=3k^2$, $\epsilon=\eta^{1/m}$, whereas η is approximately $3s^2$ from eq (4.2). Hence

$$3k^2 \leq 4(3s^2)^{3/m}(1+\eta^{-3/2m})^4(\eta/3s^2)^{3/m}. \qquad (4.5)$$

Taking the maximum on the right when $m \geqq 3$, we see that the corresponding factors in parentheses are as follows:

$$3k^2 \leqq 4(3s^2)\cdot 2^4(1+2^{1/3}+2^{2/3})/3, \qquad (4.6)$$

(the last factor being the one where $m=3$, $s=1$), the inequality (4.6) is contradicted when $k>10s$. Q.E.D.

The list of 21 cases is given in table 1 in order of increasing k. Those cases in which the fundamental unit was known to Dedekind or Cassels are denoted [4] by a "D" or "C", respectively. In the other cases, easily, $k>10s$. The possibility that $\eta=\epsilon^2$ is *excluded* by the fact that in these cases the class number, calculated by assuming $\eta=\epsilon$, will turn out to be *odd*.

5. Subroutines

The following number-theoretic subroutines were programed for this computation: One should bear in mind that the SEAC is a binary machine with a 44 bit word and sign bit. The numbers treated range arithmetically from $-4+2^{-42}$ to $4-2^{-42}$, i. e., the decimal point is fixed between the second and third high-order bit. Integers are held in the low end of the register (or scaled by 2^{-42}).

1. *Division of two integers* to produce integral quotient and integral remainder. (The built-in division operation produced only a "decimal" quotient.)

2. *The Euclidean algorithm*, or solution in X, Y of

$$sX+tY=(s,t). \qquad (5.1)$$

3. *Reduction of modules.*[5]

4. *Multiplication of modules.*[5]

5. *Generation of coefficients of* $Q(x,y)$ (from $\{A,B,C\}$ of eq (3.6)).

6. *Transformation of coefficients of* $Q(x,y)$ *under unimodular change of variables.*

7. *Reduction of* $Q(x,y)$ *to the properly or improperly equivalent reduced form* $Q^*(x,y)$ *subject to conditions* (3.12). To do this we first find the minimum value of $Q(x,y)$ by scanning all of the finite set of points for which $Q(x,y)<Q(1,0)=A^2$, or for which

$$[Ax+(B+C/2)y]^2+3C^2y^2/4<A^2. \qquad (5.2)$$

If the minimum value is $Q(x_0,y_0)=R$, then the Euclidean algorithm generates an integral unimodular transformation of coordinates, (or finds a_{12},a_{22}), so that $a_{22}x_0-a_{12}y_0=1$. Thus in the new coordinates,

$$\left.\begin{aligned} x_0X'+a_{12}Y'&=x \\ y_0X'+a_{22}Y'&=y \end{aligned}\right\} \qquad (5.3)$$

$Q(x,y)$ becomes

$$Q(X,Y)=RX'^2+S'X'Y'+T'Y'^2. \qquad (5.4)$$

Now to minimize the coefficient of $X'Y'$, all we need do is perform the transformation

$$\left.\begin{aligned} X'&=X+gY \\ Y'&=Y, \end{aligned}\right\} \qquad (5.5)$$

choosing $g=-[S'/2R]$, (the integral part), and we obtain $Q^*(X,Y)$ of eq (3.11) and (3.12).

8. *Determination of the residue character of a quadratic form.* This subroutine finds a small [6] prime p represented by $Q^*(X,Y)$ and not dividing D. (The procedure is similar to the search for the minimum of $Q(x,y)$ by eq (5.2).) Then the eq (3.7) is tested with $+x$ and $-x$, where x runs from 1 to $(p-1)/2$. If x passes through all these values without eq (3.7) being satisfied, then, and only then, Q is a nonresidue form.

9. *The built-in "base zero" operations.* These are standard fixed-point subroutines for input conversion to binary form and output conversion to decimal form, for logarithms, exponentials, sines, and cosines, among others.

6. First Run. Class Numbers

The subroutines listed earlier, taken together with the formulas and concomitant explanations, should indicate the basic program for computing h. It must be added that (binary) nonintegral quantities used, e. g., in logarithmic computations were scaled by 2^{-14}, and the final decimal values for $h \log_{10} \epsilon$ were expressed to six decimal places.

The basic procedure is to generate the $9k''$ triples $\{A,B,C\}$ in lexicographic order. For each triple we compute the corresponding forms Q and (reduced) Q^*, and finally we form (and accumulate) the contributions (3.14), resulting in the following data (in decimal form):

Input: "Case number", a, b, k, D

Output: For a nonresidue form, eq (3.11),

$$R,S$$

[4] See headnote to table 1.

[5] See section 7.

[6] No effort was made to secure the smallest p, although this seems to have happened accidentally in the few cases spot checked. The smallest prime would have required much more programing, although the effect might have proved rewarding.

For a residue form, eq (3.7), (3.11),

$$x,p,R,S$$

Final output,

$$h \log \epsilon,\ h \log_{10} \epsilon.$$

For simplicity, R and S, which are never negative, were packed into one word, likewise x (with sign removed) and p. To identify a residue form, the x, p combination was printed first, with a minus sign. The residue and nonresidue forms are omitted from the final tabulation to save space. The division $h=h \log_{10}\epsilon/\log_{10}\epsilon$ was performed by hand, resulting in integral h to five significant figures (see table 1). The data from tables of Dedekind and Cassels are denoted by "D" and "C", respectively.

During the actual runs, the program was read in on wire, and the parameters were read in on teletype tape in trios of "case number", a, b. (Here the case number was packed with identifying information to check the tape position.) The output was on teletype printer.

The program exhausted almost 900 of the 1,024 electrostatic memory spaces.

The running time varied from 3 minutes for case I to 14 hours for case XXI. A subroutine permitted the current $\{A,B,C\}$ and cumulative sum of $\pm\log$ H(ω) to be dumped every half hour or so for rerun purposes. Almost no time went into input-output, by comparison. The vast bulk of the time went toward the testing of the residue characters, i. e., toward the solution or nonsolution of eq (3.7). The problem was brought to a close at case XXI largely because time was beginning to become prohibitive.

The SEAC has no overflow stops at all, not even for 0/0, and no automatic error checks. As a substitute for both, a test was made to see if the discriminant of each quadratic form checks with $-3k^2$. In the range covered, no overflow would have occurred, barring machine errors.

7. Group Structure of Modules

A good deal of insight into the machinery of Dedekind's formula is gained by considering the composition structure of the group of quadratic forms in the "order" of discriminant $-3k^2$. Once again, rather than summarize a well-known and lengthy theory, we shall consider the modules only in relation to the present computation.

The notation

$$\mathfrak{M}=[A_1+B_1\rho, \ldots, A_t+B_t\rho] \tag{7.1}$$

denotes the aggregate of integers in $R(\rho)$

$$\xi=\Sigma n_i(A_i+B_i\rho),$$

where n_i are integers. Such a set is called a *module*. Every module has a *reduced basis* like $[A, B+C\rho]$ identified with the triple $\{A,B,C\}$ of section 3. Here *A is taken as the minimum positive rational integer in* $\mathfrak{M}$, and $B+C\rho$ is defined by the conditions that C is the *minimum positive coefficient of* ρ, *whereas B is the minimum positive integer in a module element in which the coefficient of* ρ *is* C. The enumeration of triples $\{A,B,C\}$ enumerates modules, of course, whereas $Q(x,y)$ is the norm of an arbitrary element of the module. Clearly

TABLE 1

"D" and "C" denote units or class numbers appearing in Dedekind's and Cassel's works, respectively.

Case	s	$\|M\|$	a	b	c	$\log_{10}\eta$	ϵ		k	k''	$h \log_{10}\epsilon$	h		Generator	D
I	1	2	2	1	1	0. 585159	η	D	6	1	0. 585159	1	D	$2^{1/3}$	−108
II	2	9	1	3	1	1. 096455	η	D	9	1	1. 096455	1	D	$3^{1/3}$	−243
III	3	28	7	2	1	1. 436650	$\eta^{1/2}$	D	14	2	2. 154975	3	D	$28^{1/3}$	−588
IV	−18	5831	17	1	7	2. 987641	η	D	17	2	2. 987641	1	D	$17^{1/3}$	−867
V	8	513	19	1	3	2. 283584	$\eta^{1/2}$	D	19	2	3. 425376	3	D	$19^{1/3}$	−1083
VI	−2	7	7	1	1	1. 060137	η	D	21	2	3. 180412	3	D	$7^{1/3}$	−1323
VII	−3	26	26	1	1	1. 425922	η	D	26	4	4. 277770	3	C	$26^{1/3}$	−2028
VIII	19	6860	5	2	7	3. 034650	$\eta^{1/2}$	D	30	6	4. 551974	3	D	$20^{1/3}$	−2700
IX	−10	999	37	1	3	2. 476964	η	D	37	4	7. 430929	3	C	$37^{1/3}$	−4107
X	−4	63	7	3	1	1. 678966	η	D	63	6	10. 073793	6	D	$63^{1/3}$	−11907
XI	−9	728	91	1	2	2. 385408	η		91	8	21. 468668	9	D	$91^{1/3}$	−24843
XII	23	12168	1	39	2	3. 200589	η	D	117	12	19. 203533	6	C	$39^{1/3}$	−41067
XIII	5	126	14	3	1	1. 876216	η		126	18	16. 885942	9		$126^{1/3}$	−47628
XIV	7	344	43	1	2	2. 167739	η	D	129	14	26. 012867	12	C	$43^{1/3}$	−49923
XV	−5	124	31	2	1	1. 873900	η		186	30	16. 865096	9		$124^{1/3}$	−103788
XVI	4	65	65	1	1	1. 683490	η	D	195	24	30. 302812	18		$65^{1/3}$	−114075
XVII	−6	215	215	1	1	2. 032753	η		215	28	42. 687799	21		$215^{1/3}$	−138675
XVIII	6	217	217	1	1	2. 034093	η		217	20	54. 920504	27		$217^{1/3}$	−141267
XIX	−7	342	38	3	1	2. 166895	η		342	54	58. 506160	27		$342^{1/3}$	−350892
XX	15	3376	422	1	2	2. 829347	η		422	70	59. 416280	21		$422^{1/3}$	−534252
XXI	17	4914	182	1	3	2. 938049	η		546	72	79. 327311	27		$182^{1/3}$	−894348

$$\rho\mathfrak{M}=\rho[A,\ B+C\rho]=[\rho A,\ -C+(B-C)\rho]$$

is another module leading to the same $Q(x,y)$, as $N(\rho)=1$, so is $\rho^2\mathfrak{M}$. Thus the triples $\{A,B,C\}$ or the reduced modules $[A,\ B+C\rho]$, with $AC=k$, come in "threes," leading to the same form $Q(x,y)$.

Dedekind considered the multiplicative group formed by the modules under multiplication of basis elements:

$$[A,\ B_1+C_1\rho][A_2,\ B_2+C_2\rho]=$$
$$[A_1A_2,\ A_1B_2+A_1C_2\rho,\ A_2B_1+A_2C_1\rho,\ (B_1B_2-C_1C_2)+(B_1C_2+B_2C_1-C_1C_2)\rho]. \quad (7.2)$$

It can be shown that the product module can be reduced to the form $[A_3,\ B_3+C_3\rho]$ where $A_3C_3=k$, (provided $A_1C_1=A_2C_2=k$). This process is closely analogous to the composition of forms, or, of course the multiplication of ideals.

For the purpose of performing this multiplication of modules we need two subroutines mentioned earlier (numbers 3 and 4 of section 5).

3. *Reduction of modules*, (from $[A_1,\ B_1+C_1\rho,\ B_2+C_2\rho]$ to the reduced form $[A,\ B+C\rho]$).

4. *Multiplication of modules.* This is the repeated application of the earlier subroutine for the reduction of product (7.2) to $[A,\ B+C\rho]$.

The notation "residue" (or "nonresidue") module can now be introduced to correspond to "residue" (or "nonresidue") form. Dedekind has shown that the set of residue modules forms a subgroup of index three among the set of all modules. Thus the nonresidue modules can be partitioned into co-sets so that all modules are of type

$$\mathfrak{R},\ \mathfrak{R}\mathfrak{N}_1,\ \mathfrak{R}\mathfrak{N}_1^2,$$

where $\mathfrak{R}$ is a *variable* residue and $\mathfrak{N}_1$ is a fixed nonresidue module. In the notation $\mathrm{H}(\mathfrak{M})$ for $\mathrm{H}(B+C\rho/A)$, we can write in accordance with (2.1)

$$\epsilon^h=\frac{\Pi\mathrm{H}(\mathfrak{R}\mathfrak{N}_1)}{\Pi\mathrm{H}(\mathfrak{R})}. \quad (7.3)$$

Now if we take precautions that once $\mathfrak{R}$ appears, $\rho\mathfrak{R}$ and $\rho_2\mathfrak{R}$ shall *not* appear, we have only k'' factors in numerator or denominator.

Now (7.3) is very close to Dedekind's original formula. (Dedekind used quadratic forms and not modules to generate the products in (7.3).)

8. Ambiguous Forms and Modules

To appreciate the relation between modules and forms we must realize that not only do $\mathfrak{M}$, $\rho\mathfrak{M}$, $\rho^2\mathfrak{M}$ correspond to the same form but $\mathfrak{M}$ and $\overline{\mathfrak{M}}$ can correspond to the same form. Here $\mathfrak{M}$, the conjugate module is defined by

$$\left.\begin{aligned}\mathfrak{M}&=[A,\ B+C\rho]\\ \mathfrak{M}&=[A,\ B+C\rho^2].\end{aligned}\right\} \quad (8.1)$$

The difficulty really arises when $\mathfrak{M}=\overline{\mathfrak{M}}$, (or $\rho\mathfrak{M}=\overline{\mathfrak{M}}$, etc.). (The second possibility is really no different as it implies $\rho^2\mathfrak{M}$ is then its own conjugate.) These are the *ambiguous* forms of classical number theory. Generally $\mathfrak{M}\overline{\mathfrak{M}}=[1,\ k\rho]$ the unit element, or principal ideal so that if $\mathfrak{M}=\overline{\mathfrak{M}}$, $\mathfrak{M}^2$ is a unit element and $\mathfrak{M}$ must belong to any subgroup of index three. In other words the self-conjugate modules are all *residue* modules.

To give an ample illustration let us take case VI, $s=-4$, $k=21$, and list the $9k''=18$ modules in lexicographic order, as does the computing machine, but with the interrelations in question clearly indicated.

LIST OF MODULES FOR $k=21$

$[1,\ 21\rho]=\mathfrak{M}_0$	$[7,\ 5+3\rho]=\mathfrak{M}_3$	$[21,\ 7+\rho]=\rho\mathfrak{M}_1$
$[3,\ 7\rho]=\mathfrak{M}_1$	$[7,\ 6+3\rho]=\overline{\mathfrak{M}_2}$	$[21,\ 9+\rho]=\rho\mathfrak{M}_3$
$[3,\ 1+7\rho]=\overline{\mathfrak{M}_1}$	$[21,\ \rho]=\rho\mathfrak{M}_0$	$[21,\ 13+\rho]=\rho^2\mathfrak{M}_3$
$[7,\ 3\rho]=\rho\overline{\mathfrak{M}_1}$	$[21,\ 1+\rho]=\rho^2\mathfrak{M}_0$	$[21,\ 15+\rho]=\rho^2\overline{\mathfrak{M}_1}$
$[7,\ 3+3\rho]=\rho^2\mathfrak{M}_1$	$[21,\ 4+\rho]=\rho^2\overline{\mathfrak{M}_2}$	$[21,\ 16+\rho]=\rho^2\mathfrak{M}_2$
$[7,\ 4+3\rho]=\mathfrak{M}_2$	$[21,\ 6+\rho]=\rho\overline{\mathfrak{M}_2}$	$[21,\ 18+\rho]=\rho\mathfrak{M}_2$.

These modules form a group with identity element $\mathfrak{M}_0$. Rather than construct the whole group table we might identify $\mathfrak{M}_i,\rho\mathfrak{M}_i,\rho^2\mathfrak{M}_i$ as one element, and it is easy to see that the group reduces to an abelian group of order 6 given by

$$\mathfrak{M}_0,\ \mathfrak{M}_1,\ \mathfrak{M}_3,\ \overline{\mathfrak{M}_1}=\mathfrak{M}_1^2,\ \mathfrak{M}_2=\mathfrak{M}_1\mathfrak{M}_3,\ \overline{\mathfrak{M}_2}=\mathfrak{M}_1^2\mathfrak{M}_3 \quad (8.2)$$

with the generators $\mathfrak{M}_1$, $\mathfrak{M}_3$ satisfying

$$\mathfrak{M}_0=\mathfrak{M}_1^3=\mathfrak{M}_3^2. \quad (8.3)$$

We see $\mathfrak{M}_0$, $\mathfrak{M}_3$ are the residue subgroup, for clearly, $\mathfrak{M}_0=\overline{\mathfrak{M}_0}$, $\mathfrak{M}_3=\overline{\mathfrak{M}_3}$.

The corresponding quadratic forms, (grouped after Dedekind with their "negatives"), are [7]

$$\left.\begin{aligned}\mathfrak{M}_0:&\quad x^2\pm xy+331y^2=Q_0(x,y)\\ \mathfrak{M}_1:&\quad 9x^2\pm 3xy+37y^2=Q_1(x,y)\\ \mathfrak{M}_2:&\quad 13x^2\pm 9xy+27y^2=Q_2(x,y)\\ \mathfrak{M}_3:&\quad 19x^2\pm 11xy+19y^2=Q_3(x,y).\end{aligned}\right\} \quad (8.4)$$

Forms for $\mathfrak{M}_0$ and $\mathfrak{M}_3$ are ambiguous (or self-conjugate). Note that $ab^2=7$, so that for the primes given

$$\begin{cases}331=Q_0(0,1), & 10^3\equiv 7\pmod{331}\\ 19=Q_3(1,0), & 4^3=7\pmod{19}\end{cases}$$

[7] The negative of $Q(x,y)$ is found by replacing S by $-S$ or, effectively, by keeping R and D fixed and replacing S by $2R-S$.

TABLE 2

Case	Test value		Form			
			Residue		Nonresidue	
	$\|x\|$	p	R	S	R'	S'
I	4	31	1	0	4	2
II	16	61	1	1	7	3
III	11	151	1	0	4	2
	6	61	3	0	12	18
IV	3	223	1	1	7	13
	11	73	3	3	13	15
V	31	271	1	1	7	3
	26	97	3	3	13	23
VI	10	331	1	1	9	15
	4	19	* 19	27	13	17
VII	49	523	1	0	4	6
	17	181	3	0	12	6
	4	19	19	10	21	24
	4	19	19	28	7	10
VIII	14	691	1	0	4	2
	22	127	25	0	13	2
	1	19	19	6	25	20
	1	19	19	32	9	6
	1	7	7	10	25	40
	1	7	7	4	27	36
IX	304	1, 033	1	1	7	11
	104	349	3	3	21	39
	1	19	19	23	31	27
	1	19	19	15	13	25
X	305	3, 019	1	1	9	15
	21	73	49	49	19	33
	9	37	37	9	49	63
	9	37	37	65	43	45
	1	31	31	11	49	7
	1	31	31	51	13	1
XI	747	6, 211	1	1	49	7
	17	139	49	49	49	77
	8	67	67	125	37	13
	11	79	* 79	147	43	21
	8	67	67	9	57	3
	454	2, 089	3	3	61	17
	4	31	31	53	19	3
	4	31	31	9	73	59
XII	3,364	10, 267	1	1	9	15
	2	139	81	63	81	9
	2	139	81	99	81	45
	6	193	63	39	7	11
	6	193	63	87	63	3
	15	103	* 103	37	49	17
	1	19	19	31	67	65
	3	43	43	27	79	31
	4	31	31	47	73	55
	4	31	31	15	37	59
	3	43	43	59	61	13
	1	19	19	7	97	35

* Signifies quadratic form whose negative belongs to a conjugate module.

Case	Test value		Form			
			Residue		Nonresidue	
	$\|x\|$	p	R	S	R'	S'
XIII	352	11, 923	1	0	4	2
	18	331	36	66	36	30
	18	331	36	6	9	6
	71	439	49	0	73	48
	43	163	81	72	79	82
	43	163	81	90	43	82
	2	67	67	70	81	36
	2	67	67	64	49	70
	12	103	103	24	49	84
	12	103	103	182	61	108
	13	109	109	130	37	18
	13	109	109	88	81	18
	4	31	31	22	117	102
	4	31	31	40	97	22
	4	19	19	10	76	10
	11	241	52	54	13	2
	11	241	52	50	52	102
	4	19	19	28	76	66
XV	93	25, 921	1	0	4	6
	87	751	36	66	9	12
	87	751	36	6	36	42
	17	1, 069	27	0	108	54
	109	499	52	2	13	2
	55	997	63	6	103	200
	64	397	76	22	76	98
	56	601	148	206	148	58
	56	601	148	90	37	16
	64	397	76	130	19	16
	55	997	63	120	163	80
	109	499	52	102	52	50
	3	97	97	180	157	254
	12	463	117	102	61	20
	3	151	151	292	43	10
	7	73	73	96	91	50
	163	1, 447	91	76	79	106
	13	211	133	92	109	78
	31	193	171	174	49	22
	23	241	108	18	27	18
	115	937	28	34	7	6
	115	937	28	22	28	50
	23	241	108	98	108	90
	31	193	171	168	133	22
	13	211	133	174	63	78
	163	1, 447	91	106	117	24
	7	73	73	50	139	242
	3	151	151	10	172	162
	12	463	117	132	127	142
	3	97	97	14	67	120
XVI	838	28, 549	1	1	9	3
	253	1, 297	25	25	133	191
	11	211	169	169	61	103
	111	409	169	273	31	37
	111	409	169	65	109	131
	43	157	157	165	25	35
	7	139	139	105	169	143
	7	139	139	173	25	5
	43	157	157	149	127	239
	2	19	19	1	169	299
	2	19	19	37	171	75
	6	151	151	9	169	221
	18	79	79	157	49	61
	18	79	79	1	169	247
	6	151	151	293	175	215
	12	163	163	5	37	25
	2	73	73	103	175	145
	48	463	63	75	63	33
	4	43	43	45	103	7
	342	1, 063	27	27	27	45
	4	43	43	41	133	37
	48	463	63	51	7	9
	2	73	73	43	67	115
	12	163	163	321	97	71

in accordance with eq (3.7). In the "general" situation, of course, the residue modules will not all be ambiguous.

9. Second Run. Residue Group

A second run was undertaken to simulate more closely Dedekind's original method, which consisted of using the structure of the residue group. The advantage in so doing is clear if we think of the fact that most of the computing time goes toward testing eq (3.7) for a solution. The amount of work can be cut to about a sixth [8] if we agree to keep the quadratic forms in storage so as to never test the same form twice. Because the memory had been almost exhausted by the program, magnetic tape was used for storage of forms.

The second run proceeded as follows. The machine generated the modules, testing each in turn until it came to (say) $\mathfrak{R}_1$, the first nonresidue module, which it put into memory. (Only the internal memory had been used thus far.) Once the machine reached this point it returned to the *beginning* of the list of modules and did two things "simultaneously": First of all, it tested each module whose quadratic form was not on the tape and loaded on the tape [9] every form that had been tested. Second, the machine took the residue module (say) $\mathfrak{R}$ that had not been previously tested (and loaded on tape) and formed $\mathfrak{R}_1\mathfrak{R}$ loading both quadratic forms on tape, while it accumulated $\log H(\mathfrak{R}_1\mathfrak{R}) - \log H(\mathfrak{R})$.

The second run led to an interesting array of quadratic forms which we see in table 2. Here R,S refer to coefficients of the residue quadratic form and R',S' refer to the corresponding nonresidue quadratic form which is formed by multiplying by the module $\mathfrak{R}_1$ as explained earlier.

Unfortunately, here overflow was a serious problem in the multiplication of modules, and only cases I through XVI, excluding XIV, went to completion. The forms for which $S=R$ or zero obviously correspond to self-conjugate modules.[10] The other self-conjugate modules are marked by "a", and can be spotted by the fact that the residue quadratic form and its negative do *not* both appear in table 2 (see footnote 9).

[8] Unfortunately tape motion produced too much delay (as much as 1 min per search) to permit these benefits to be fully realized.

[9] Here, whenever $\overline{\mathfrak{M}}=\mathfrak{M}$, $\rho\mathfrak{M}$, or $\rho^2\mathfrak{M}$, one should load both the Q for $\mathfrak{M}$ and the negative Q (for $\overline{\mathfrak{M}}$) on the tape to prevent both Q and its negative from appearing as residue forms. This fact had been overlooked and had to be corrected by an undesirable manual intervention in the computation.

[10] See footnote to table 2.

10. Concluding Prospects

The computation consummated here represents one phase of what really amounts to a larger task. The computation of units should also be programed, possibly after Voronoi's algorithm [5], so that h can be found even when M does not have the fortuitous form s^3+1. The storage of the previously tested forms in a larger high-speed memory would, of course, have speeded up computations, but the testing of congruence (3.7) leaves much to be desired in the direction of efficiency. To carry the groupings of modules and forms on to larger k, a double precision multiplication of modules would have to be provided. Lastly, it would be desirable to find the class structure algebraically [2], which is not altogether beyond the capacity of the SEAC.

The class structures, as well as the group structures, of the modules shall be the subject of further theoretical investigations.

The author thanks Olga Taussky for her aid and encouragement.

11. References

[1] J. W. S. Cassels, The rational solutions of the diophantine equations $Y^2=X^3-D$, Acta Math. **82,** 244 (1950).
[2] H. Cohn, Some experiments in ideal factorization on the MIDAC, J. Assoc. Comput. Mach. **2,** 111 (1955).
[3] H. Cohn and S. Gorn, A computation of cyclic cubic units, J. Research NBS **59,** 155 (1957) RP2783.
[4] R. Dedekind, Über die Anzahl der Idealklassen in reinen kubischen Zahlkörpern, Journ. für die reine und ang. Math. **121,** 40 (1900)
[5] B. N. Delauney and D. K. Fadeev, Theory of irrationals of third degree (in Russian), Travaux de l'Institut Stekloff XI (1940).
[6] R. Fueter, Vorlesungen über die singulären Moduln und die komplexe Multiplikation der elliptischen Funktionen, vol. I (Teubner, Leipzig, 1924).
[7] E. Hecke, Theorie der algebraischen Zahlen (Akad. Verlag, Leipzig, 1923).
[8] A. Markoff, Sur les nombres entiers dependents d'une racine cubique d'un nombre entier. Mém. de l'Acad. Imp. des Sciences de St. Pétersbourg, VII 38 (1892).
[9] T. Nagell, Über die Einheiten in reinen kubischen Zahlkörpern. Videnskap. Skrift. I, Mat. Kl., 11 (1923).
[10] O. Taussky, Some computational problems in algebraic number theory, numerical analysis, Proc. Symp. Appl. Math. Vol. 6. Amer. Math. Soc. 1956, 187–193.

WASHINGTON, March 14, 1957.

Journal of Research of the National Bureau of Standards Vol. 59, No. 4, October 1957 Research Paper 2799

Impact Properties of Slack-Quenched Alloy Steels

Melvin R. Meyerson and Samuel J. Rosenberg

A method was developed for slack quenching impact specimens so as to produce uniform and accurately controlled hardnesses and microstructures at any location in the cross section. Steels of the 81xx type, without and with boron, and varying in hardenability, were studied to evaluate the effect of slack quenching upon the impact properties.

Slack quenching was shown to be detrimental to the impact properties of the steels. The injurious effects were found to be dependent on the carbon and alloy content of the steels, the degree of slack quenching, and the amount of tempering.

When any two steels were slack quenched to the same hardness, the higher carbon lower alloy steel had impact properties inferior to those of the lower carbon higher alloy steel. Tempering usually improved the properties of both and reduced the differences between them.

The higher the hardness to which any steel was slack quenched, the lower were its impact properties. When tempered to the same hardness, however, the steel originally slack quenched to the higher hardness had the better impact properties.

1. Introduction

Despite the fact that slack-quenched structures are frequently found in heat-treated steels, quantitative evaluation of the effect of slack quenching upon the mechanical properties of such steels has never been adequately defined. This is due, not to lack of recognition that such data are needed, but rather to the lack of heat-treating techniques that can accurately control the desired slack-quenched microstructures.

In an effort to overcome this deficiency, many researches have evaluated the effect of nonmartensitic decomposition products of austenite upon the mechanical properties of various steels. With but one exception, the amount and nature of the nonmartensitic products have been controlled by the use of isothermal transformation techniques. Although much excellent work of this nature has been carried out, the results obtained are not necessarily indicative of the properties of slack-quenched steels in which the amount and nature of the nonmartensitic products may vary considerably, depending upon size effects and the rate of cooling. The reported exception is the work of Vajda and Busby [1,2],[1] who end quenched 7-in. diameter rounds and tested specimens cut from sections parallel to the quenched ends. Although the technique developed was new and useful, it suffers from two disadvantages in that the mass of steel needed for development of the slack-quenched specimens is considerable and the cross sections of the test specimens so obtained cannot be uniform because finite differences in cooling rates must exist. These authors attempted to minimize the latter by using subsize specimens, but the fact remains that finite changes in cooling rate, with corresponding differences in microstructure, exist over the cross sections of the specimens so obtained.

The project described in this paper is concerned with the effect of slack quenching upon the impact properties of steels, data which were desired by Watertown Arsenal. The problem posed was: Given a pair of selected steels whose Jominy (end quench) hardenability curves crossed each other, the intersection of these curves represent equal hardness, obtained at equal cooling rates. The resulting microstructures, however, could be expected to be dissimilar. Information was desired as to the effect such slack quenching would have upon the impact properties of the steels involved.

The present paper describes a simple technique for accurately controlling the hardness and microstructure of slack-quenched impact specimens, and gives the results of the effect of slack quenching, both with and without tempering, upon the impact properties of a series of 81xx steels, both without and with boron. Specifically, a comparison is made between the structure and impact properties of various pairs of steels, slack quenched to the hardness corresponding to a point of intersection of their Jominy curves (the steels were intentionally designed to give this intersection). A similar comparison is made of the structures and impact properties of pairs of the same steels treated with boron and slack quenched to obtain a hardness equal to that at the point of intersection of their Jominy curves. A third comparison is made between pairs of the boron-free and boron steels. A few supplementary tests were made on some of the same steels as fully hardened and then tempered to the same hardness levels as the slack-quenched steels, or the slack-quenched and tempered steels.

2. Experimental Steels

2.1. Design, Melting, Fabrication, and Analyses

Using 8140 as a base, it was planned to study the effects of slack quenching upon similar alloy steel of higher and lower carbon, with the alloy content so modified that the Jominy hardenability curves of the various steels intersect. Jominy hardenabilities were calculated in accordance with the procedure described in the Metals Handbook [3], using the values and multiplying factors given therein. For purposes of calculation, an ASTM grain size number of 8 was assumed for all steels. The validity of this

[1] Figures in brackets indicate the literature references at the end of this paper.

TABLE 1. *Chemical compositions and hardening temperatures of the steels*

Steel No.	Percent by weight										Hardening temperature
	C	Mn	P	S	Si	Ni	Cr	Mo	Al	B	
											° F
BR-27	0.49	0.87	------	------	0.33	0.22	0.30	0.08	0.05	None	1,500
BR-28										0.0018	
BR-21	.46	.91	0.005	0.029	.28	.24	.35	.10	.06	None	1,500
BR-22										0.0017	
BR-17	.44	.87	.005	.026	.27	.32	.46	.16	.07	None	1,550
BR-18										0.0019	
BR-1	.38	.44	------	------	.08	.30	.42	.13	.06	None	1,550
BR-2										0.0022	
BR-25	.30	.75	------	------	.28	.52	.68	.15	.05	None	1,600
BR-26										0.0021	
BR-19	.28	.90	.006	.027	.30	.45	.62	.21	.08	None	1,600
BR-20										0.0017	
BR-23	.19	.96	.005	.024	.33	.63	.86	.32	.08	None	1,625
BR-24										0.0020	
BR-29	.19	.95	------	------	.33	.68	.86	.19	.06	None	1,625
BR-30										0.0024	

assumption was borne out by subsequent metallographic examinations.

Beginning with the calculated hardenability of 8140, using the composition corresponding to the middle of the range (0.41% C, 0.85% Mn, 0.28% Si, 0.30% Ni, 0.43% Cr, 0.11% Mo), hardenability curves were calculated for steels at carbon levels of 0.20 percent, 0.30 percent, and 0.50 percent with manganese and silicon constant at the midlevel of 8140 and with nickel, chromium, and molybdenum increased for the two lower carbon levels and decreased for the higher carbon steel. In changing the alloy content, the Ni-Cr-Mo ratio was maintained constant at the same ratio as exists in 8140. Several curves were calculated for each carbon level, using different totals of alloy content, and from these curves four steels varying in carbon content were selected for melting.

All steels were melted in an induction furnace, using a magnesia crucible. Each melt was 150 lb, deoxidized with aluminum (2 lb/ton) and split two ways during pouring with boron (as ferroboron) added in the ladle to one-half of each melt. The steels were poured into hot-topped split molds 13½ in. high, 2¾ in. square at the bottom and 3¾ in. square at the top. A cast Jominy specimen also was poured from each split heat. The ingots, containing about 45 lb of usable metal, were either surface ground or cleaned by tumbling and then hot rolled to ⅝ in. plate. A 4 in. length (for Jominy specimens) was sheared off when the plate thickness reached 1¼ in. All plates were normalized at 1,650° F before being machined into specimens.

The compositions of the steels are listed in table 1. Chemical analyses were made only on samples taken from the boron-treated halves of the split heats.

A metallographic examination was made of each boron-free steel shown in table 1. Photomicrographs of these (except BR–29) in the hot-rolled and normalized condition are shown in figure 1. Ferrite banding was absent or very slight, BR–1 being the worst in this respect. In three of the steels (BR–17, 19, and 23), the carbides were partially spheroidized.

2.2. Hardenability

At least one Jominy hardenability test was made on each steel, both as cast and normalized, and as hot rolled and normalized. The proper hardening temperature, based on carbon content, was used for each steel in making the Jominy tests, and in all subsequent hardening. These temperatures are shown in the last column of table 1. The addition of boron resulted in improved hardenability in each case, and the amount of improvement varied with the composition of the steel (figs. 2 and 3). Generally, those steels that had the lowest carbon content were improved the most by the addition, an exception being BR–1, which was low in manganese and silicon. The results obtained on both the cast and wrought specimens of the same steel agreed closely. However, the curves did not, in general, coincide with the computed curves; the experimental curves indicated lower hardenability than was computed (fig. 4).

The ASTM procedure for making Jominy hardenability tests [4] specifies that the hardenability test bar be quenched from the proper hardening temperature for that steel. The graph paper supplied by ASTM for plotting the results of hardenability tests indicates that a specific cooling rate (at 1,300° F) is obtained at each increment of distance from the quenched end. Actually this cooling rate can be influenced somewhat by the hardening temperature. However, because the range of hardening temperatures used in the present study was relatively small (±65° F), it is believed that variations in cooling rate, due to the different quenching temperatures used, were insignificant.

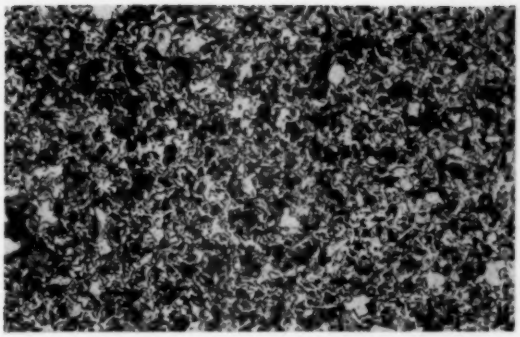

BR-27 (0.49% C)

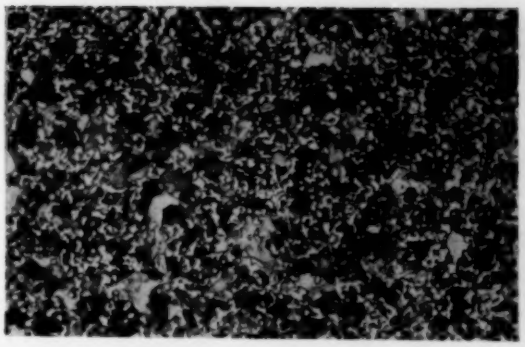

BR-21 (0.46% C)

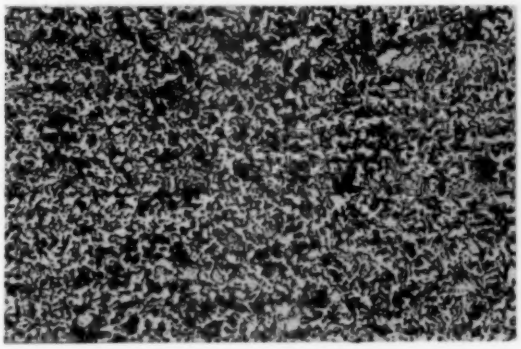

BR-17 (0.44% C)

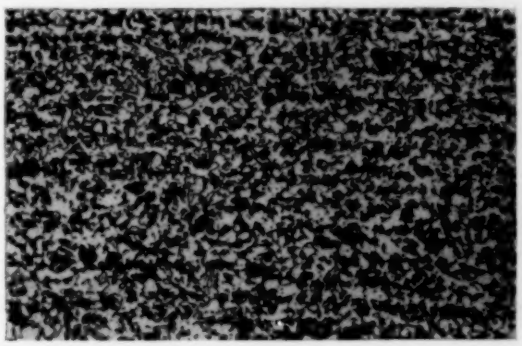

BR-1 (0.38% C)

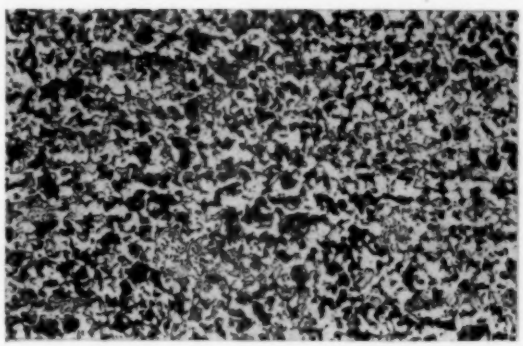

BR—25 (0.30% C)

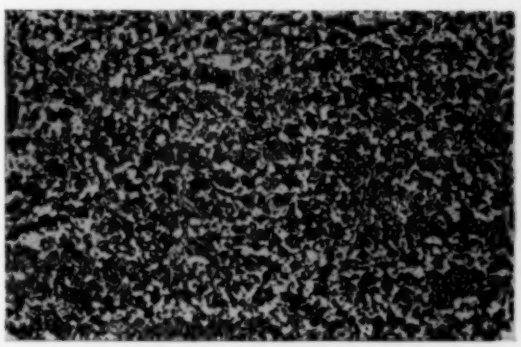

BR-19 (0.28% C)

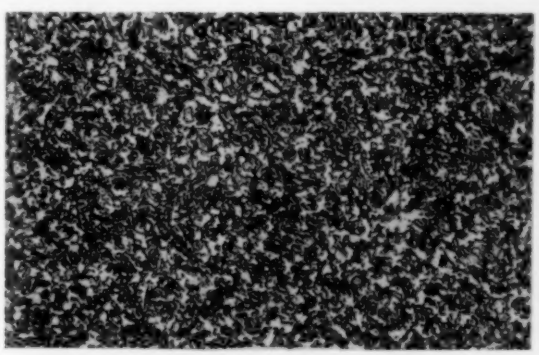

BR-23 (0.19% C)

FIGURE 1. *Structures of boron-free steels.*
Hot rolled to 5/8 in. plate and then normalized (1 hr at 1,650° F, air cooled). Etched in 1% nital. × 100.

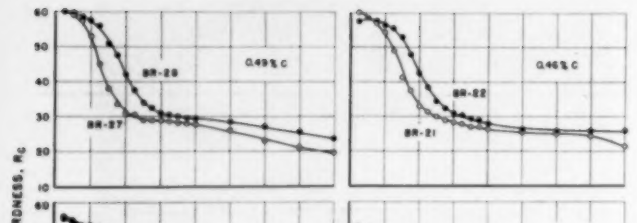

FIGURE 2. *Hardenability curves for split heats of steels as hot rolled and normalized.*

Numbers on curves are the steel identification numbers. Odd-numbered steels are the base steels; even-numbered steels are the boron-treated splits.

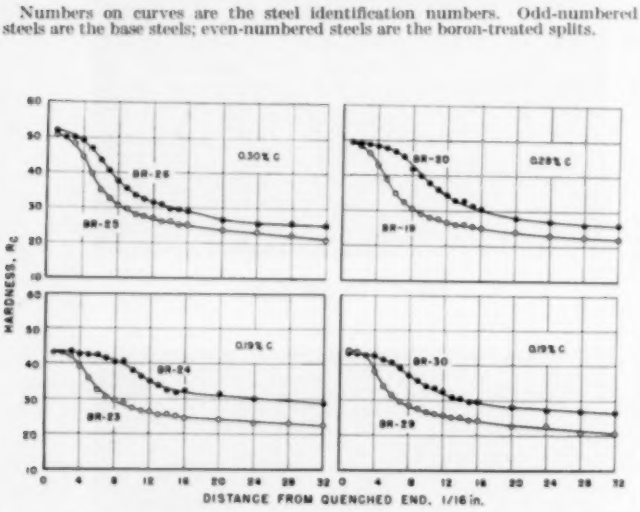

FIGURE 3. *Hardenability curves for split heats of steels as hot rolled and normalized.*

Numbers on curves are the steel identification numbers. Odd-numbered steels are the base steels; even-numbered steels are the boron-treated splits.

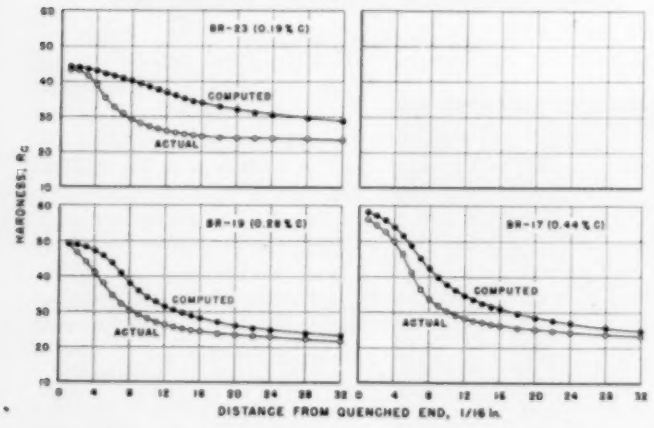

FIGURE 4. *Comparison of computed and actual hardenabilities of some of the steels.*

In order to determine accurately the points of equal hardness at equal cooling rates between any two or more steels, all of the hardenability curves were plotted on an expanded scale as a single master graph, and the intersections of the various curves determined. For practical purposes, and because of the limits of accuracy in hardness testing, curves approaching each other within $\pm\frac{1}{2}$ R_c were considered as intersecting even if no actual intersection occurred. Only intersections at a hardness level of 30 R_c or higher were used. Four such hardenability curves, taken from the master graph, are shown in figure 5.

Based on carbon content and provided that the hardenability curves cross each other only once, there are six possible intersections of two curves each, for the boron-free steels, and six for the boron steels. There are only six possible intersections of two curves each for the boron-free steels versus the boron steels, because the presence of boron always improved the hardenability. It was found that none of the curves of the higher carbon steels containing boron intersected those of the lower carbon steels without boron. For convenience, each combination will be referred to as follows:

Code A—0.50% C and 0.41% C
Code B—0.41% C and 0.30% C
Code C—0.30% C and 0.20% C
Code D—0.50% C and 0.30% C
Code E—0.41% C and 0.20% C
Code F—0.50% C and 0.20% C

Although 18 combinations of one intersection were theoretically possible, only 15 could be obtained, as

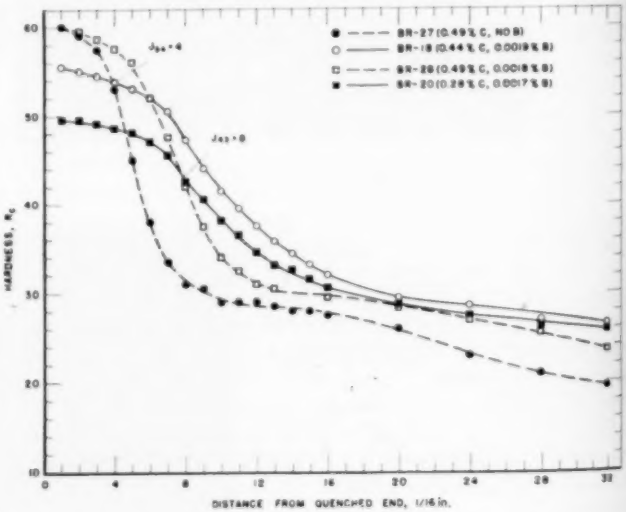

FIGURE 5. *Jominy hardenability curves for four of the steels.*

Intersections of the curves indicate points of equal hardness at equal cooling rates.

indicated in table 2. In order to obtain this many combinations, it was necessary to utilize steel BR–1, which had a low manganese and silicon content.

All of the steels were examined metallographically after being slack quenched to the proper hardness level at which they were to be tested, and the microstructures at each of the hardness levels noted in table 2 are shown in figures 6, 7, and 8. The structures varied according to carbon and alloy content, and the hardness levels to which the steels were slack quenched, and the two steels of any pair quenched to the same hardness usually varied in structure, often markedly. Steels quenched to the higher levels of hardness contained appreciable amounts of martensite, some bainite, and occasionally small amounts of pearlite and sometimes even traces of ferrite. As the slack-quenched hardness decreased, more bainite, pearlite, and ferrite appeared in the microstructures. The relative amounts of the various constituents were influenced by the carbon content in that the lower carbon steels had more martensite and bainite, and less pearlite, when quenched to moderate levels of hardness, than did the higher carbon steels. This difference in any pair of steels became more marked as the differential in carbon content increased.

TABLE 2. *Selected intersections (±½ R_c) of Jominy hardenability curves*

Combination code	Steel numbers and percent carbon content	Hardness at intersection, R_c	Distance from quenched end, 1/16 in.
	Boron-free steel versus boron-free steel		
A	BR–27 (0.49C) and BR–17 (0.44C)	46	5
B	BR–1 (0.38C) and BR–25 (0.30C)	49.5	3
C	BR–19 (0.28C) and BR–23 (0.19C)	30	8
D	BR–27 (0.49C) and BR–25 (0.30C)	33	7
E	Not obtained	.....	.....
F	Not obtained	.....	.....
	Boron-free steel versus boron steel		
A	BR–27 (0.49C) and BR–18 (0.44C)	54	4
B	BR–17 (0.44C) and BR–26 (0.30C)	48	5
C	BR–19 (0.28C) and BR–24 (0.19C)	42	4
D	BR–21 (0.46C) and BR–20 (0.28C)	48	5
E	BR–17 (0.44C) and BR–30 (0.19C)	40	6
F	BR–21 (0.46C) and BR–24 (0.19C)	43	5
	Boron steel versus boron steel		
A	BR–18 (0.44C) and BR–22 (0.46C)	52.5	6
B	BR–18 (0.44C) and BR–20 (0.28C)	30	18
C	BR–24 (0.19C) and BR–26 (0.30C)	43	6
D	BR–20 (0.28C) and BR–28 (0.49C)	43	8
E	Not obtained	.....	.....
F	BR–30 (0.19C) and BR–28 (0.49C)	33	12

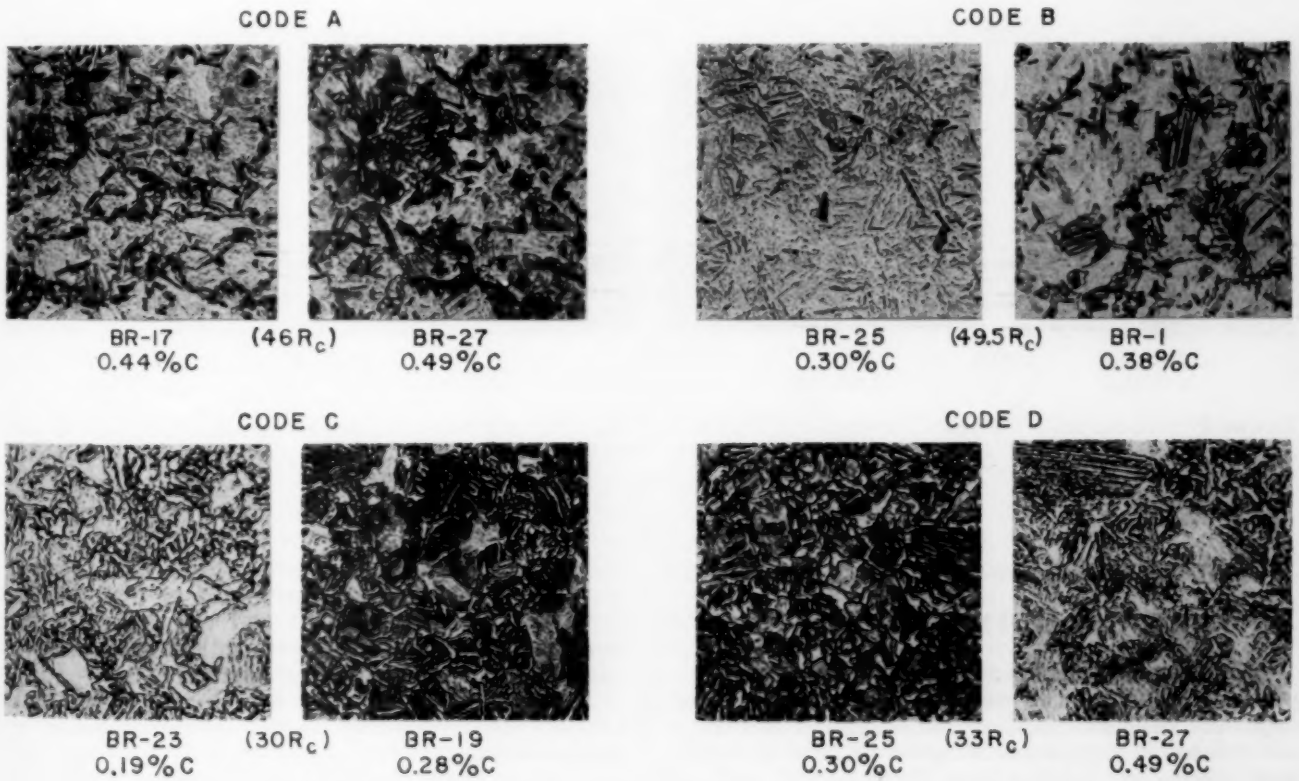

FIGURE 6. *Microstructures of pairs of steels, boron-free, slack quenched to hardness levels selected for testing.*

Etched with 1% nital. × 500.

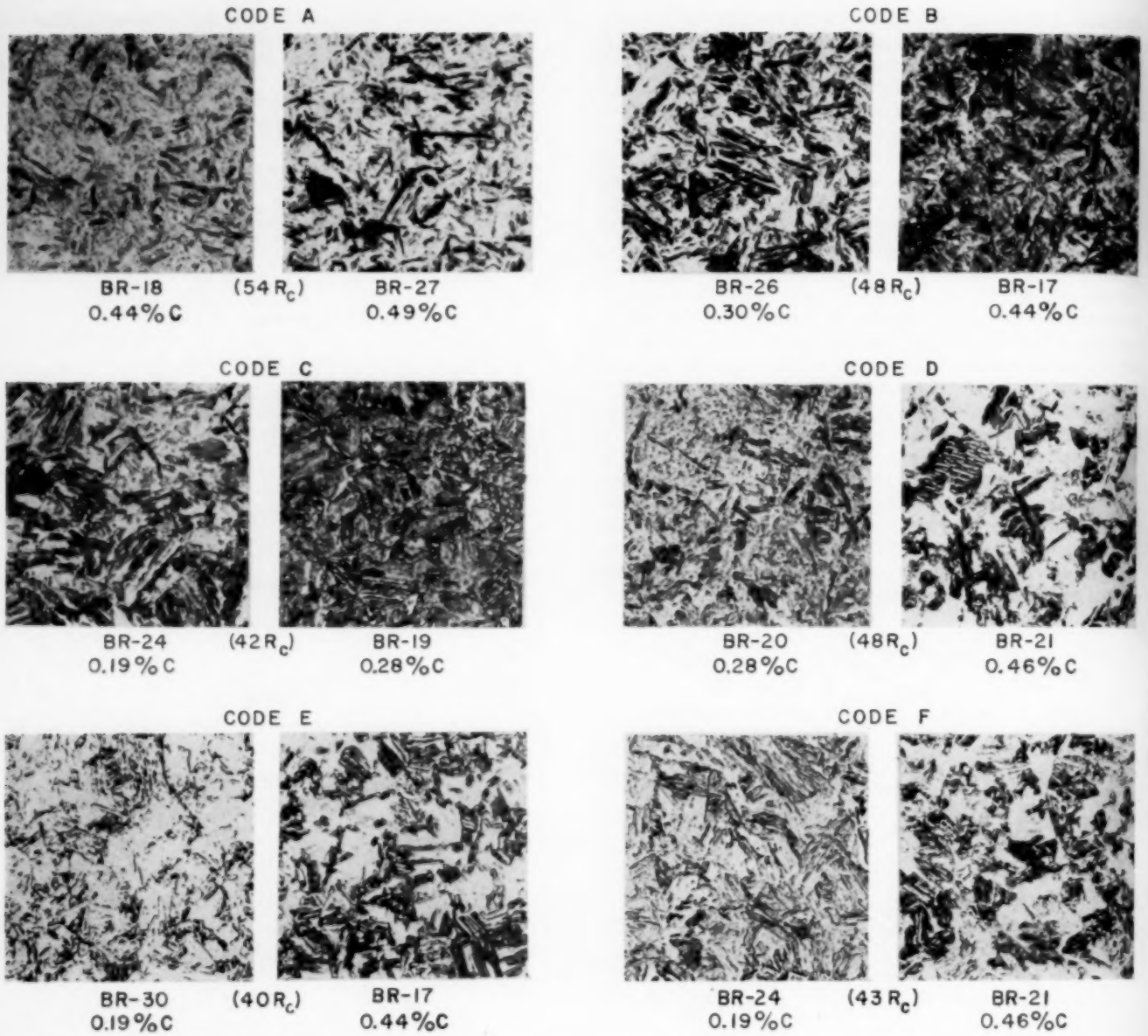

FIGURE 7. *Microstructures of pairs of steels, boron-treated (even numbered) and boron-free (odd numbered), slack quenched to the hardness levels selected for testing.*

Etched with 1% nital. × 500.

3. Development of Heat-Treating Techniques

3.1. Controlled Slack Quenching

A Jominy specimen contains an infinite number of planes parallel to the quenched end, each of theoretically constant cooling characteristics (assuming no surface cooling), and decreasing in rate of cooling with increasing distance from the quenched end. If heat loss through radiation is low in comparison with the rate of abstraction of heat from the quenched end, impact specimens should be amenable to end quenching and so develop an infinite number of planes, each uniformly cooled. With this thesis in mind, experiments were conducted to evaluate the effect of various means of end quenching impact specimens so as to develop controlled hardnesses at selected distances from the quenched end.

The root of the V-notch in a Charpy specimen is 1.08 in. (approximately $1\frac{7}{16}$ in.) from each end. In steels of moderate hardenability, the hardness value obtained at $1\frac{7}{16}$ in. from the quenched end of a Jominy specimen usually is appreciably lower than the maximum obtainable. It was obvious, therefore, that any method that was developed for end quenching impact specimens would have to give markedly

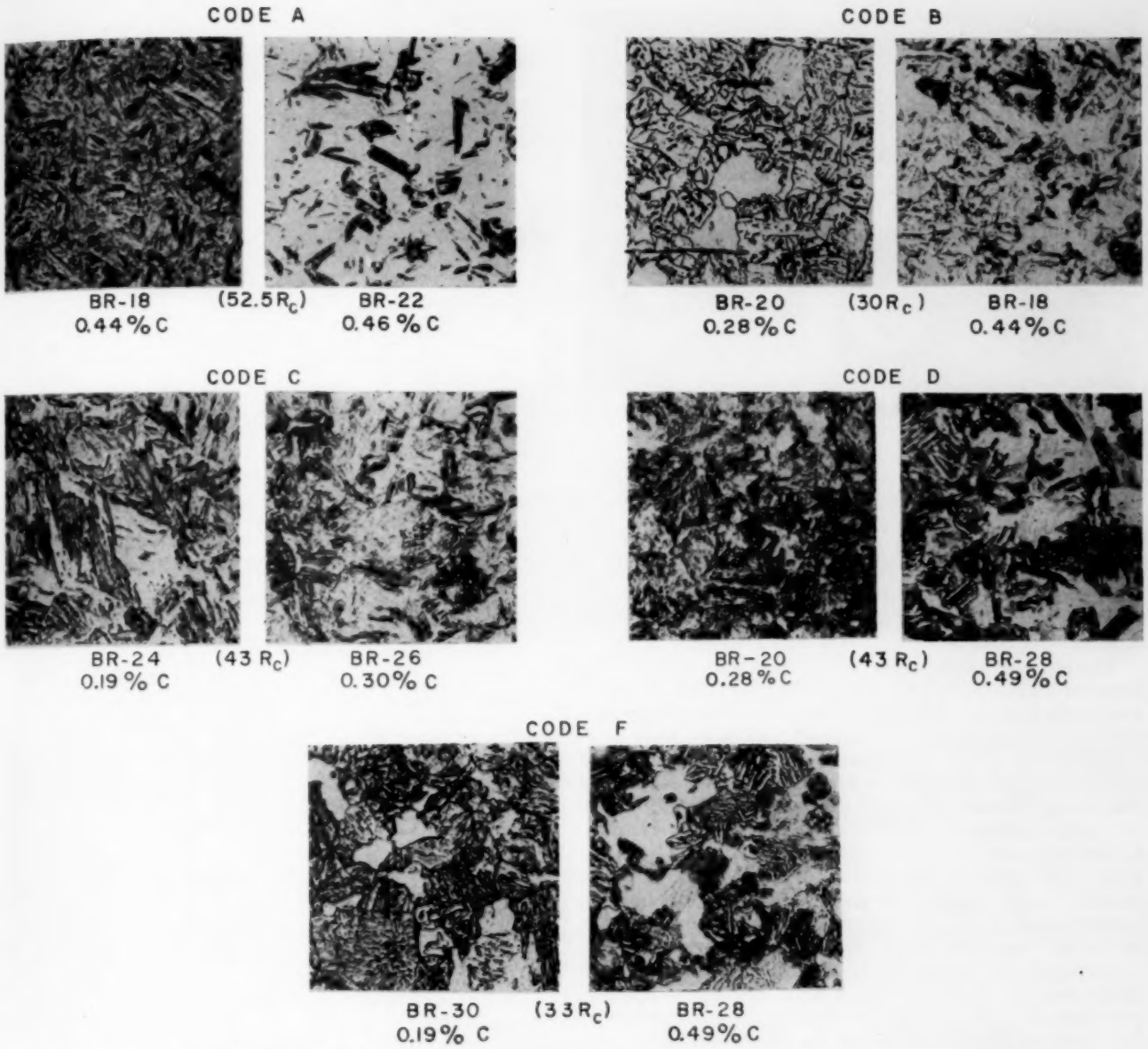

FIGURE 8. *Microstructures of pairs of steels, boron-treated, slack quenched to the hardness levels selected for testing.*

Etched with 1% nital. × 500.

faster cooling rates at a distance of $1\frac{7}{16}$ in. from the quenched end than that attained in the conventional Jominy specimen, if impact specimens were to be slack quenched to hardnesses only slightly below the maximum possible. Several methods to speed the rate of cooling, involving the use of various specially designed shapes and adapters, were tried, but none was completely satisfactory. The method finally adopted had the advantages of simplicity, reproducibility, and economy of material and machining. The details of this method are as follows:

The impact specimen is rough machined to approximately 0.42 in. square to allow for scaling and decarburization and to a length of $2\frac{5}{16}$ in. so that there will be some latitude for locating the notch. One end is drilled and tapped to accommodate about a ¼-in. length of a ¼-20 screw, 2 in. long. A washer, locked in a selected position by two nuts, serves to support the specimen in the quenching fixture so that a predetermined portion of the length of the specimen is immersed vertically into a still-quenching medium, which may be brine, water, or any other suitable liquid. The quenching fixture is a ¼-in. steel plate with 8 holes $\frac{21}{32}$ in. in diameter so as to accommodate 8 specimens (fig. 9). Metal straps attached to the steel plate hold it in position above the quenching bath. After quenching, the specimens are stress relieved at 250° F to prevent cracking and are then ground equally on each side to 0.394 in. square, thereby

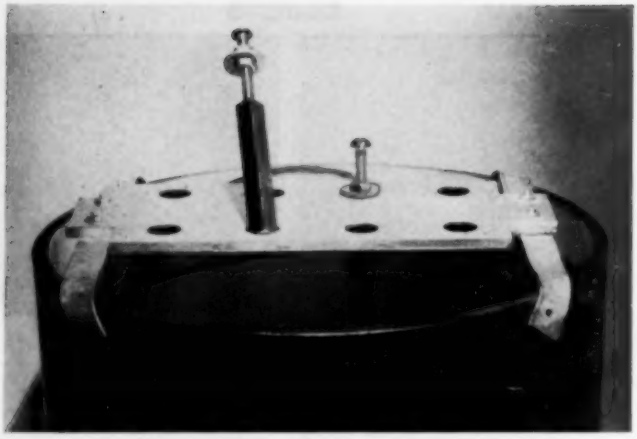

FIGURE 9. *Fixture for end-immersion quenching of impact specimens.*

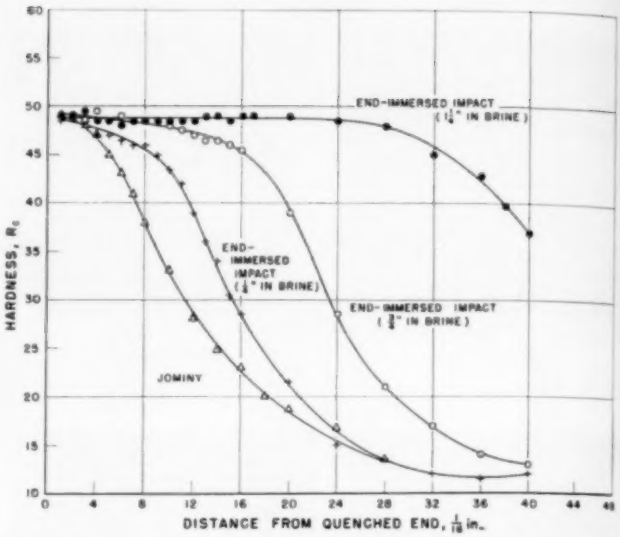
HARDNESS, R_c
DISTANCE FROM QUENCHED END, 1/16 in.
END-IMMERSED IMPACT (1 1/4" IN BRINE)
END-IMMERSED IMPACT (1/4" IN BRINE)
END-IMMERSED IMPACT (3/8" IN BRINE)
JOMINY

FIGURE 10. *Hardenability curves obtained by end immersing impact specimens to various depths in brine compared with the standard curve obtained from a 1-in. round Jominy specimen end quenched in the conventional manner.*

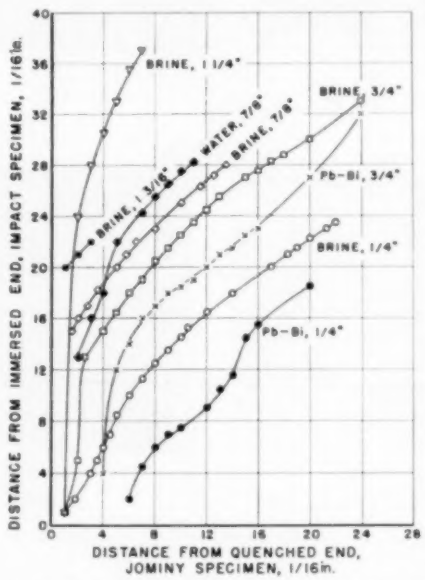

FIGURE 11. *Correlation between end-immersed impact specimens and end-quenched Jominy specimens.*

The plotted points represent locations of equal hardness and, consequently, equal cooling rates. For example, assume it is desired to duplicate in an impact specimen the same hardness as that produced at 8/16 in. from the quenched end of a Jominy specimen. From the curves, end immersing an impact specimen to 7/8 in. in brine will produce this hardness at a distance of 23/16 in. from its immersed end. Furthermore, immersing the impact specimens to 3/4 in. in brine will produce the desired hardness at 20/16 in. Temperature of the lead-bismuth alloy was 300° F.

removing any decarburization that may have occurred. A hardness survey is then made on one face to locate the exact position of the notch. This location is marked, a standard V-notch is cut into the specimen at this point, and the ends of the specimen are cut off at a distance of 1.08 in. on each side of the notch.

During the exploratory work, specimens of a commercial steel (0.28% C, 1.6% Mn, 0.0015% B) were end immersed to different levels, and the hardnesses and microstructures at various positions were correlated with those that existed in a standard Jominy end-quenched specimen of the same steel. Repeated hardness checks and metallographic examinations of end-immersed impact specimens showed consistently equal hardness and similar microstructures over the entire cross section of any selected plane parallel to the quenched end. Hardness surveys on impact specimens end immersed to various depths in brine, together with the Jominy curve for the same steel, are shown in figure 10. Examination of these curves indicated that any hardness (corresponding to some particular cooling rate) existing in the Jominy specimen could be duplicated by end immersing the impact specimen. The correlation between the normally end-quenched Jominy specimens and the impact specimens, immersed to different depths in brine, water, and liquid lead-bismuth alloy, is shown in figure 11.

As a result of the exploratory work described, performed on the steel noted, additional tests were conducted on one of the experimental steels. An impact specimen was end immersed into brine to a depth of 7/8 in. and the hardness was measured on flats 0.015 and 0.197 in. (approximately center) below the original surface. The hardness and microstructure at both levels checked closely; the curves shown in figure 12 represent the averages of the hardness readings plotted against the distances from the quenched end. The microstructures of both the end-immersed impact specimen and of the Jominy specimen of the same steel at selected locations of equal hardness are also shown in this figure. It will be noted that the microstructures at positions of equal hardness are similar and that the structure of the impact specimen at any plane of hardness is uniform from just below the surface to the center. An additional example of the uniformity of structure that exists from just below the surface to the center of an end-immersed impact specimen of another steel is shown in figure 13.

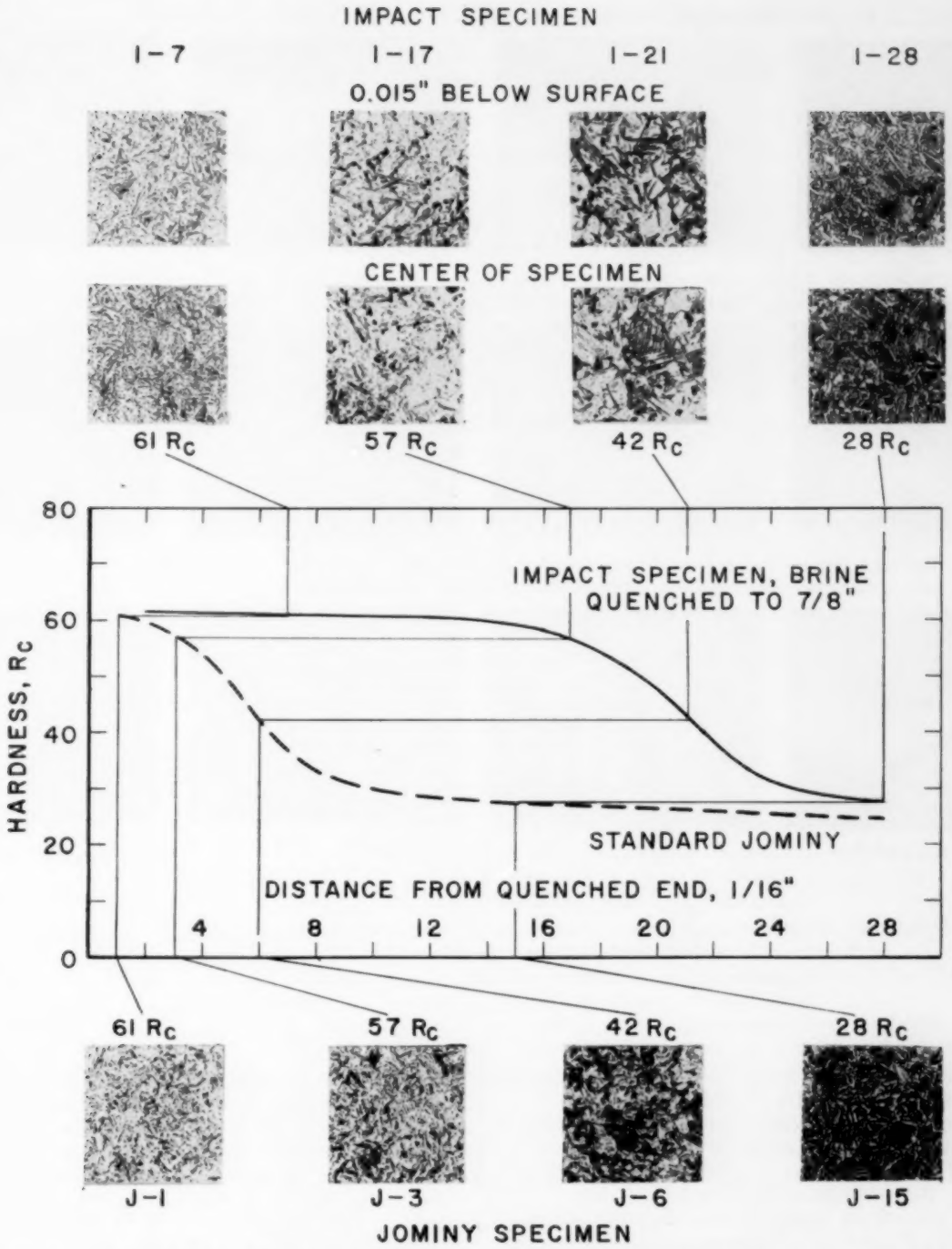

FIGURE 12. *End-quench hardenability curves and microstructures at equivalent hardness levels on a standard Jominy specimen and an end-immersed impact specimen from a single steel (BR-21, 0.46% C).*

Etched with 1% nital. × 500.

3.2. Controlled Tempering

In addition to comparing the impact properties of pairs of different steels slack quenched to the same hardness at similar cooling rates, it was desired also to compare these pairs of steels as slack quenched to the same hardness and subsequently tempered to a lower but equal hardness. It was apparent that the tempering treatments necessary to produce the desired hardness could be expected to vary from steel to steel and that comprehensive

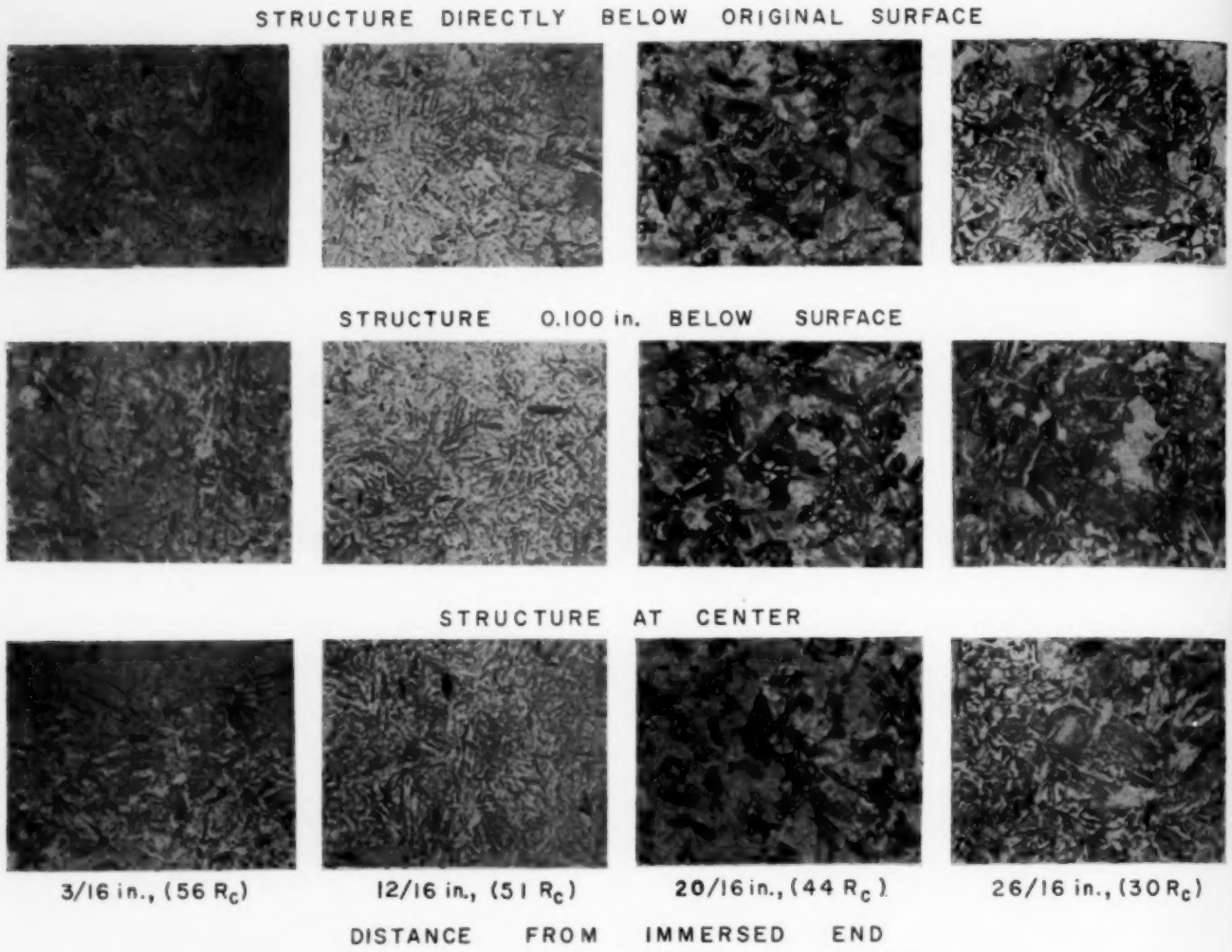
STRUCTURE DIRECTLY BELOW ORIGINAL SURFACE
STRUCTURE 0.100 in. BELOW SURFACE
STRUCTURE AT CENTER
3/16 in., (56 Rc)
12/16 in., (51 Rc)
20/16 in., (44 Rc)
26/16 in., (30 Rc)
DISTANCE FROM IMMERSED END

FIGURE 13. *Uniformity of microstructure from just below the surface to the center and at different distances from the immersed end of an impact specimen of steel BR–17 (0.44% C).*

This specimen was end immersed to a depth of 7/8 in. in brine. Etched with 1% nital. × 500.

data on the influence of tempering the experimental steels, therefore, would be necessary.

Impact specimens of many of the boron-free steels were end immersed in brine to a depth of ⅞ in. The original surfaces were removed by grinding and a hardness determination was made every 1/16 in. from the quenched end. These specimens were then tempered for 1 hr in succession at 300°, 400°, 500,° 600,° 700,° 800,° 900,° and 1,000° F and a hardness survey was made of the entire length of each specimen after each temper. A similar procedure was followed with conventionally quenched Jominy bars using a tempering time of 1½ hr because of the larger cross section. The resulting data are presented in figures 14 and 15. Figure 14 shows the effect of tempering up to 1,000° F on the maximum hardness (hardness at 1/16 in. from the quenched end of the Jominy specimen) as measured on both Jominy and impact specimens. Figure 15 differs in that it shows the effect of tempering on the planes of originally equal slack-quenched hardnesses of pairs of impact specimens of the steels.

The curves of figure 15 were used as a guide for tempering the test specimens of these particular steels. These data were sufficient to serve as a general guide, subject to experimental modification, for all of the steels. After slack quenching and then stress relieving at 250° F, the planes of equal hardness were located and the specimens were then tempered for 1 hr at the proper temperature to give the desired hardness. The hardness of the same plane was checked in each specimen after tempering to assure that the proper hardness level had been reached. Any specimen which failed to develop the proper hardness within ±1 R_c (most were within less than ±½ R_c) was not used.

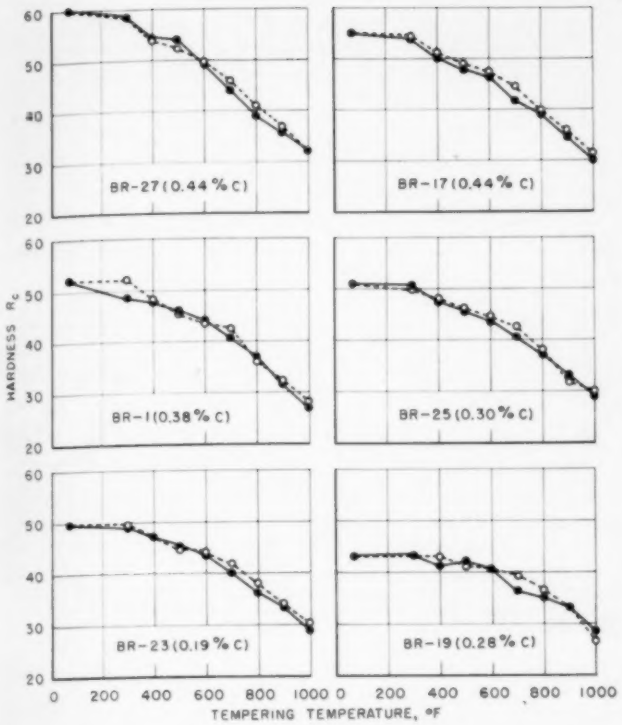

FIGURE 14. *Effect of tempering temperature on maximum hardness (hardness at J–1 of the standard Jominy bar).*

Solid lines represent values obtained from Jominy bars, dashed lines from impact specimens.

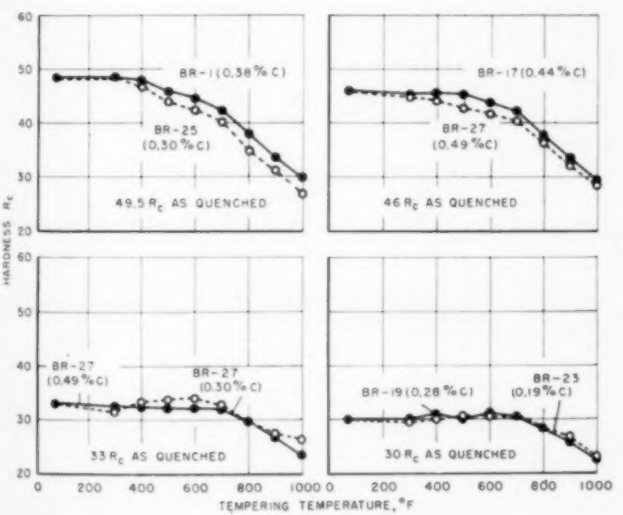

FIGURE 15. *Effect of tempering temperature on the hardness of pairs of end-immersed impact bars at planes of originally equal hardnesses and cooling rates (points of intersection of their Jominy hardenability curves).*

4. Impact Tests—Results and Discussion

4.1. Test Procedure

All tests were conducted in a Charpy impact testing machine of 224-ft-lb capacity. The machine conformed to ASTM specifications except for the radius of the striking edge which was 0.047 in. instead of 0.315 in. All specimens conformed to the ASTM standard for Charpy V-notch impact specimens (0.394 in. square times 2.165 in. long, with a 45° V-notch, 0.079 in. deep, and a root radius of 0.010 in). The test temperature varied within the range of −320° F to +300° F. Specimens tested at other than room temperature were held at the temperature of test in a liquid bath for at least 15 min prior to breaking, and the elapsed time between removal from the bath and breaking of the specimens was about 3 sec.

Impact tests were made on pairs of steels slack quenched at equal cooling rates to identical hardness levels. In addition, tests also were made on many of these pairs of steels as slack quenched to equal hardness levels and subsequently tempered to lower but equal hardness levels. Supplementary tests were made on some of the same steels as fully hardened and then tempered to the same hardness levels as the slack-quenched or slack-quenched and tempered steels.

The impact data obtained were plotted on two sets of graphs. The first (figs. 16 to 20) compares the impact properties of the various pairs of steels slack quenched to equal hardness, both with and without tempering. Data on the properties of any one steel, therefore, often appear in more than one graph, depending upon the combination of steels involved. In order to assess more directly the effect of slack quenching, both with and without tempering, upon the impact properties of individual steels, the data are replotted in the second set of graphs (figs. 21 to 27). Where available, data for the fully hardened steels are included.

All fractured specimens were examined to evaluate the relative amounts of brittle and ductile fracture. It was observed that the gradation in appearance of fracture from ductile to brittle was less distinct in many slack-quenched specimens than it was in fully hardened specimens. This was attributed to the mixed structures existing in the slack-quenched specimens. Consequently, quantitative determinations of the relative amounts of brittle and ductile fracture in slack-quenched specimens were difficult to make in some cases and the values obtained were believed to be only approximately correct. For this reason the data are not included in the graphs.

4.2. Slack-Quenched Pairs of Steels

The test data obtained on pairs of steels, slack quenched to the hardness levels indicated, and also as slack quenched and tempered, are given in figures 16 to 20, inclusive. The hardness at which each

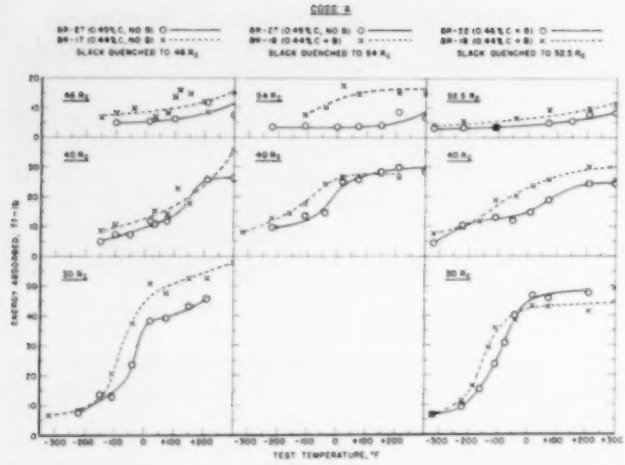

FIGURE 16. *Impact strengths of slack-quenched pairs of steels—Code A.*

The underlined hardness number in each block indicates the hardness of the steels, as quenched. The lower hardnesses were obtained by tempering the slack-quenched steels. Maximum hardness: BR-27, 60 R_c; BR-22, 58 R_c; BR-17, 55 R_c; BR-18, 55 1/2 R_c.

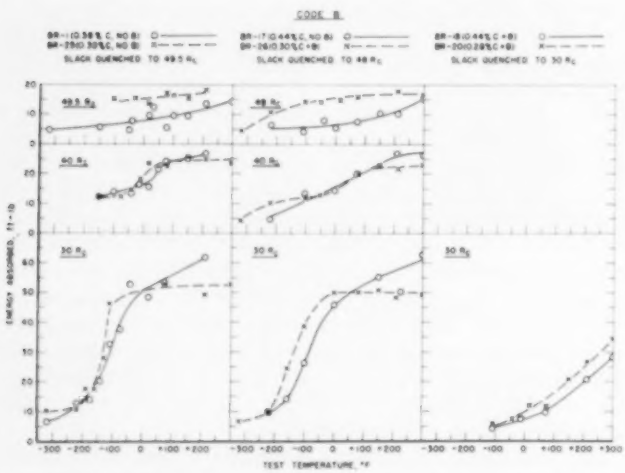

FIGURE 17. *Impact strengths of slack-quenched pairs of steels—Code B.*

The underlined hardness number in each block indicates the hardness of the steels. The lower hardnesses were obtained by tempering the slack-quenched steels. Maximum hardness: BR-17, 55 R_c; BR-18, 55 1/2 R_c; BR-1, 52 R_c; BR-25, 50 1/2 R_c; BR-26, 51 1/2 R_c; BR-20, 49 1/2 R_c.

pair of steels was tested is indicated in the various blocks by the underlined value. Each figure gives the complete data for a single combination as indicated by the code thereon and includes, where available, a nonboron versus a nonboron steel (left column), a nonboron versus a boron steel (center column), and a boron versus a boron steel (right column). Because of variations in melting, the carbon contents often varied slightly from the desired values.

A significant observation to be made from these figures is that the lower carbon steel of any pair

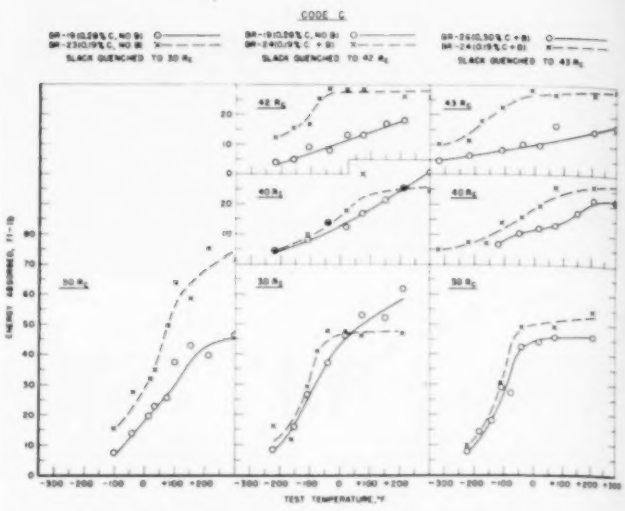

FIGURE 18. *Impact strengths of slack-quenched pairs of steels—Code C.*

The underlined hardness number in each block indicates the hardness of the steels. The lower hardnesses were obtained by tempering the slack-quenched steels. Maximum hardness: BR-26, 51 1/2 R_c; BR-19, 49 1/2 R_c; BR-23, 43 R_c; BR-25, 43 1/2 R_c.

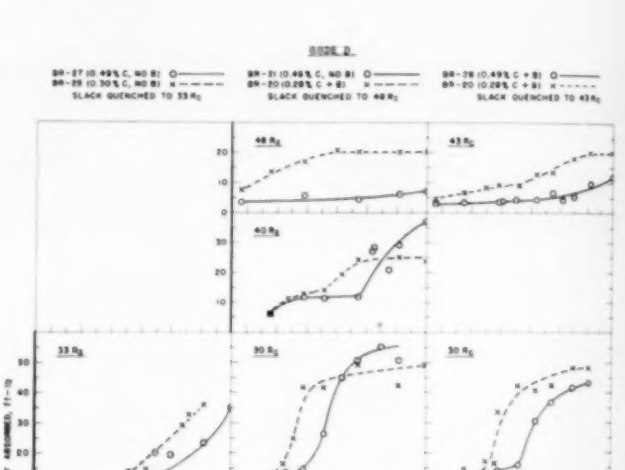

FIGURE 19. *Impact strengths of slack-quenched pairs of steels—Code D.*

The underlined hardness number in each block indicates the hardness of the steels. The lower hardnesses were obtained by tempering the slack-quenched steels. Maximum hardness: BR-27, 60 R_c; BR-28, 60 R_c; BR-21, 59 R_c; BR-25, 50 1/2 R_c; BR-20, 49 1/2 R_c.

slack quenched to the same hardness invariably showed impact properties superior to that of the higher carbon steel, regardless of whether or not boron was present. With but one or two exceptions, where the differences in the impact curves were slight, this superiority was maintained after tempering the slack-quenched pairs.

The degree of difference in impact properties noted between the individual steels of each slack-quenched pair was usually greatest in the as-slack-quenched

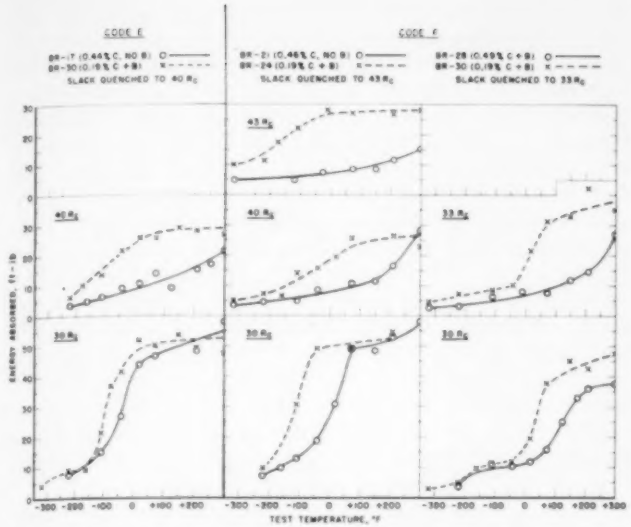

FIGURE 20. *Impact strengths of slack-quenched pairs of steels—Code E and Code F.*

The underlined hardness number in each block indicates the hardness of the steels. The lower hardnesses were obtained by tempering the slack-quenched steels. Maximum hardness: BR–28, 60 R_c; BR–21, 59 R_c; BR–17, 55 R_c; BR–30, 43 R_c; BR–24, 43½ R_c.

condition; tempering generally reduced the difference between the steels in each pair. The extent of the initial difference in impact properties of the as-slack-quenched steels was related to the difference in carbon content of the steels in each pair; i. e., the greater the difference in carbon, the greater the difference in impact properties. Tempering, generally, raised the impact strength levels of the pairs, particularly at the higher and intermediate temperatures of test. This resulted in the establishment of a more pronounced transition from ductile to brittle fracture.

It must be emphasized that, because of the design of the experimental steels, the total alloy contents varied inversely with the carbon contents and that the higher amount of alloy in the lower carbon steels may be a factor in the better impact properties shown by these steels. To separate these two variables would have necessitated melting additional series of steels not contemplated in the original plan of the investigation.

4.3. Evaluation of Effect of Slack Quenching Upon the Impact Properties

The effect of slack quenching upon the impact strength of the steels at certain hardness levels is shown in figures 21 to 27, inclusive. Each figure (except fig. 27) presents all the impact data on each split heat tested, both without and with boron. Figure 27 gives data on two steels not from the same heat (BR–1 and BR–30). Data are given for each steel as slack quenched to the hardness indicated, and as slack quenched and tempered. For comparison, data also are given, where available, on the properties of the steels as fully hardened and then tempered to the required hardness level.

The impact properties of the untempered slack-quenched steels were lower the higher the hardness to which the steels were slack quenched. This was attributed to the greater quantity of untempered martensite present in the harder steels. Upon tempering, however, this order was reversed and the steels originally slack quenched to the higher hardness levels had impact properties superior to the same steels originally slack quenched to the lower hardness levels, thus indicating the deleterious effect of slack quenching. This was attributed to the larger amounts of tempered martensite present in the steels originally slack quenched to the higher hardnesses. The steels originally slack quenched to the lower hardnesses contained less martensite that could be toughened by tempering, and more ferrite and pearlite; the two latter constituents are not appreciably toughened by tempering.

As an illustration of the trends just described, attention is directed to the data for steel BR–17 (fig. 23). This steel was slack quenched to three levels of hardness, R_e 48, 46, and 40. Examination of the curves indicates that the impact properties improved slightly as the slack-quenched hardness decreased. When tempered to 40 and 30 R_e, however, the impact properties of the steels originally slack quenched to 48 R_e were better than those slack quenched to 46 R_e, which, in turn, were better than those slack quenched to 40 R_e. Another illustration

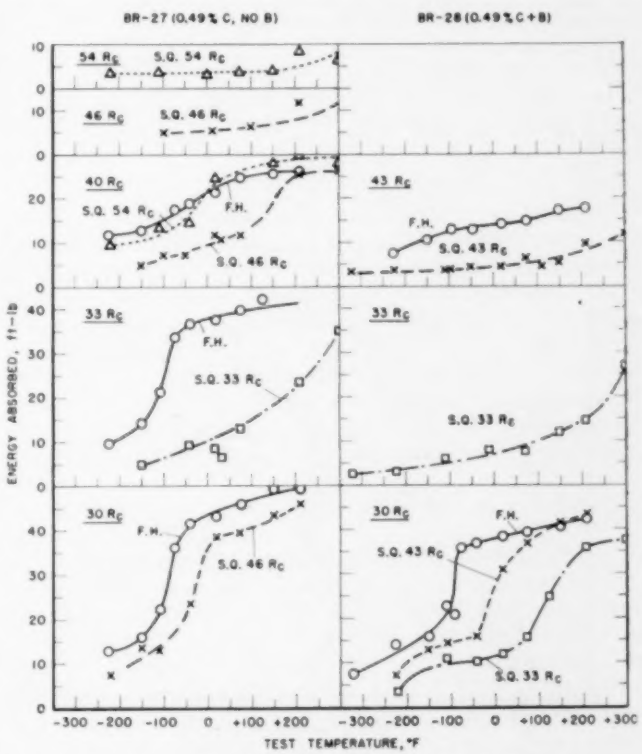

FIGURE 21. *Impact strengths of the 0.49%C steels.*

The underlined hardness number in each block indicates the hardness of the steel. The hardness number on each curve indicates the original slack-quenched hardness. Where the underlined hardness is less than the slack-quenched hardness, the specimens have been tempered. S. Q. equals slack quenched. F. H. equals fully hardened. As fully hardened, both steels had an original hardness of 60 R_c.

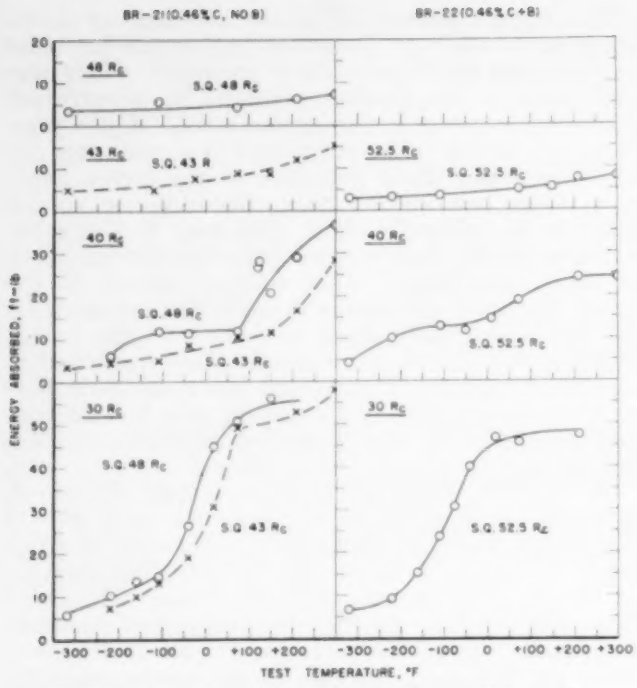

FIGURE 22. *Impact strengths of the 0.46%C steels.*

The underlined hardness number in each block indicates the hardness of the steel. The hardness number on each curve indicates the original slack-quenched hardness. Where the underlined hardness is less than the slack-quenched hardness, the specimens have been tempered. S. Q. equals slack quenched. No tests were made on steels BR-21 and BR-22 as initially fully hardened but in this condition the hardness was 59 and 58 R_c, respectively.

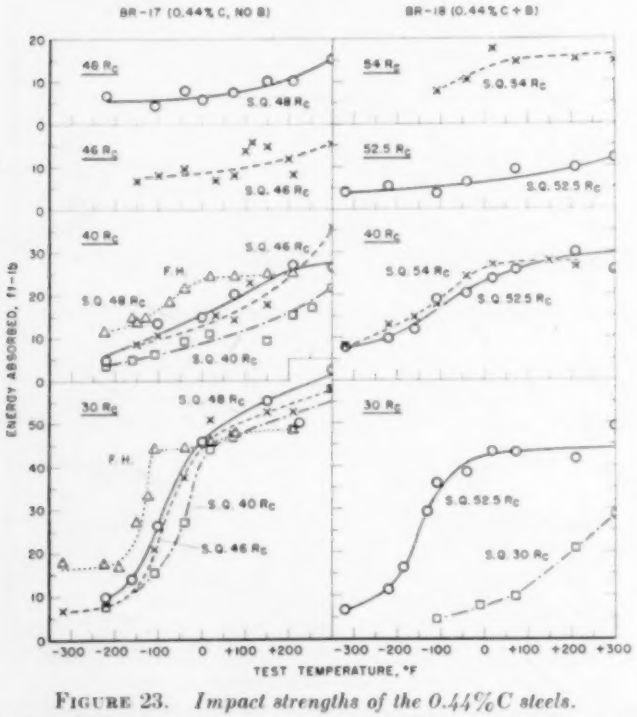

FIGURE 23. *Impact strengths of the 0.44%C steels.*

The underlined hardness number in each block indicates the hardness of the steel. The hardness number on each curve indicates the original slack-quenched hardness. Where the underlined hardness is less than the slack-quenched hardness, the specimens have been tempered. S. Q. equals slack quenched. F. H. equals fully hardened. As fully hardened, BR-17 had an initial hardness of 55 R_c. No tests were made on BR-18 as initially fully hardened, but in this condition its hardness was 55½ R_c.

of this trend is shown in figure 21 for steel BR-28. As initially slack quenched to 33 R_c and tested at that hardness, the impact properties were somewhat superior to those of the same steel initially slack quenched to 43 R_c, and tested at that hardness. However, after tempering both to 30 R_c, the steel initially slack quenched to the higher hardness had the better impact properties. When the original slack-quenched hardness was relatively high, thus indicating only a small amount of nonmartensitic products in the microstructure, the deleterious effect of slack quenching upon the impact properties was small. This is illustrated by steel BR–27 (fig. 21) tested at 40 R_c. As slack quenched to 54 R_c and then tempered to 40 R_c, the steel showed slightly inferior impact properties only below 0°F as compared with the fully hardened (original hardness equals 60 R_c) and tempered steel. The same trend was shown by many of the other steels.

Thus, at any particular hardness, the fully hardened and tempered steels were usually superior to the slack quenched and tempered steels. In some cases, however, they were only equal, or even slightly inferior to the slack-quenched steels over a portion of the testing range.

The boron and nonboron steels showed one significant difference in their reaction to tempering in the

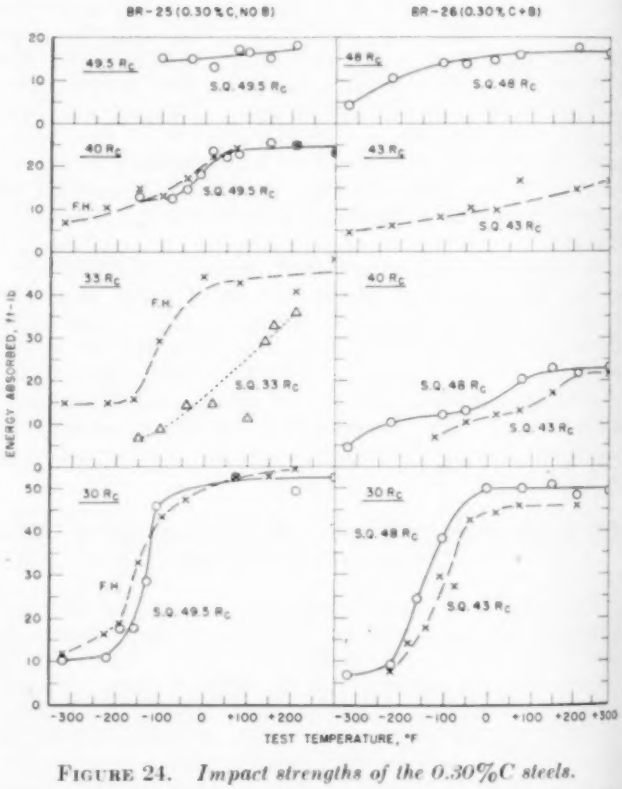

FIGURE 24. *Impact strengths of the 0.30%C steels.*

The underlined hardness number in each block indicates the hardness of the steel. The hardness number on each curve indicates the original slack-quenched hardness. Where the underlined hardness is less than the slack-quenched hardness, the specimens have been tempered. S. Q. equals slack quenched. F. H. equals fully hardened. As fully hardened, BR-25 had an original hardness of 51 R_c. No tests were made on BR-26 as initially fully hardened, but in this condition its hardness was 51½ R_c.

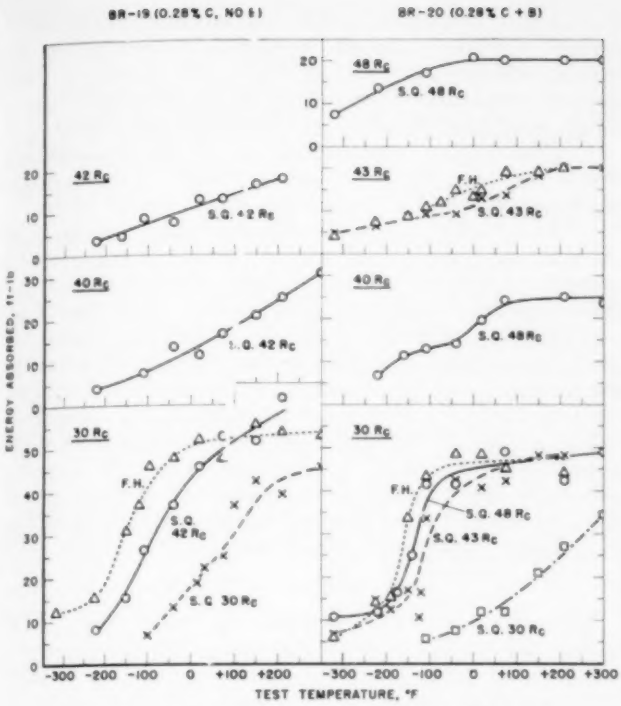

FIGURE 25. *Impact strengths of the 0.28%C steels.*

The underlined hardness number in each block indicates the hardness of the steel. The hardness number on each curve indicates the original slack-quenched hardness. Where the underlined hardness is less than the slack-quenched hardness, the specimens have been tempered. S. Q. equals slack quenched. F. H. equals fully hardened. As fully hardened, both steels had an original hardness of 49½ R_c.

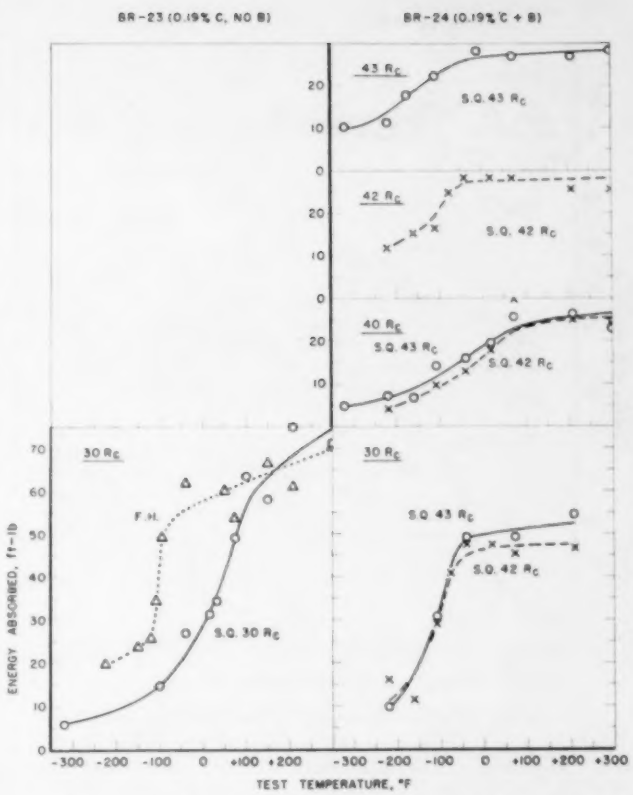

FIGURE 26. *Impact strengths of the 0.19%C steels.*

The underlined hardness number in each block indicates the hardness of the steel. The hardness number on each curve indicates the original slack-quenched hardness. Where the underlined hardness is less than the slack-quenched hardness, the specimens have been tempered. S. Q. equals slack quenched. F. H. equals fully hardened. As fully hardened, BR-23 had an original hardness of 44 R_c. No tests were made on BR-24 as initially fully hardened, but in this condition its hardness was 43½ R_c.

as-slack-quenched condition. The impact properties of the slack-quenched nonboron steels were practically always improved by tempering. Whether or not the slack-quenched boron steels were improved by tempering depended on the differential between the hardness as slack quenched and as slack quenched and tempered. When this differential was only a few points Rockwell C, tempering to 40 R_c actually caused a slight deterioration in the impact properties or, at best, no change. When, however, the differential was large, tempering to either 40 R_c or 30 R_c caused a definite improvement. Examples of this phenomenon can be seen in figures 24, 25, 26, and 27.

5. Summary and Conclusions

A method was developed and is described for heat-treating impact specimens so as to produce uniform and accurately controlled slack-quenched microstructures and hardnesses at the locations where the notches are to be placed. This technique, which should prove of considerable use in the study of steels, is a modified end-quench procedure.

A group of steels, based on the 81xx series, varying in carbon from 0.19 to 0.49 percent, and with the alloy content adjusted at a constant ratio so as to raise the hardenability of the lower carbon steels and lower the hardenability of the higher carbon steels, was melted and fabricated. Each heat was split during pouring and boron was added to one-half of the melt. Jominy hardenability tests were made on all steels and the distances from the quenched ends at which the hardenability curves of various pairs of steels intersected were determined. Impact tests were made on Charpy V-notch specimens of pairs of steels slack quenched to the hardness corresponding to the intersection of their respective Jominy curves, both as slack quenched and also as subsequently tempered. The impact properties of some of the slack-quenched steels were compared with their fully hardened and tempered counterparts.

On the basis of the data obtained, the following conclusions can be drawn:

1. When slack quenched at equal cooling rates to equal hardnesses and tested at those hardness levels, the impact properties of the higher carbon lower alloy steel of a pair were always inferior to those of the lower carbon higher alloy steel, regardless of whether or not boron was present. The greater the difference in carbon and alloy content, the greater was the difference in impact properties. Tempering generally reduced the difference between the impact properties and also raised the values.

2. The hardness level to which any individual steel was slack quenched influenced its impact properties markedly. As slack quenched only, the

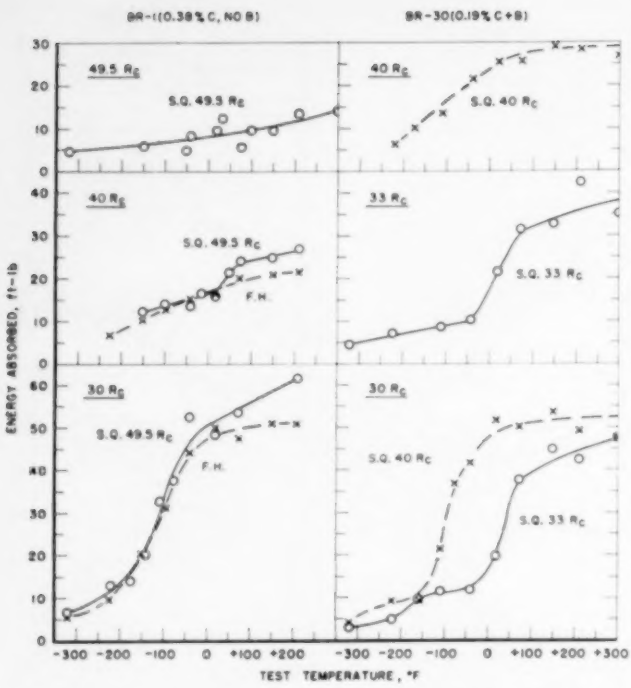

FIGURE 27. *Impact strengths of the two steels designated.*

The underlined hardness number in each block indicates the hardness of the steel. The hardness number on each curve indicates the original slack-quenched hardness. Where the underlined hardness is less than the slack-quenched hardness, the specimens have been tempered. S. Q. equals slack quenched. F. H. equals fully hardened. As fully hardened, BR-1 had an original hardness of 52 R_c. No tests were made on BR-30 as initially fully hardened, but in this condition its hardness was 43 R_c.

higher the hardness, the lower were the impact properties. Tempering, however, reversed this order in that the steels originally slack quenched to a higher hardness and then tempered to a lower hardness had impact properties superior to those of the same steels originally slack quenched to a lower hardness and then tempered.

3. The impact properties of the slack-quenched boron steels were improved by tempering to 40 R_c only when the differential between the hardness as slack quenched and as slack quenched and tempered was large. When this differential was small, tempering actually caused a slight deterioration in impact properties, or, at best, no change. The impact properties of all of the slack-quenched boron steels were improved upon tempering to 30 R_c.

4. The impact properties of all slack-quenched steels as tempered to 40 R_c were considerably improved when the steels were tempered to 30 R_c.

5. At equal hardness levels the impact properties of the slack-quenched steels, either tempered or untempered, were generally inferior to those of the fully hardened and tempered steels. The extent of the deterioration in impact properties caused by slack quenching depended on the differential between the hardness of the steel as fully hardened and as slack quenched. When the tempered slack-quenched steel had an initial hardness close to the maximum possible, the impact properties were but slightly affected. As the initial hardness of the tempered slack-quenched steel became lower, the deterioration in impact properties became more pronounced.

The investigation reported in this paper was sponsored by Watertown Arsenal. The authors are particularly grateful to Stuart V. Arnold, of Watertown Arsenal, whose advice and criticism aided so materially in the progress of the work. The authors also are deeply appreciative of the conscientious assistance of Thomas P. Royston throughout the entire course of the investigation and of Nesbit L. Carwile, who assisted materially in the latter phases of the work.

6. References

[1] John Vajda and Paul E. Busby, Transverse mechanical properties of slack-quenched and tempered wrought steel, Trans. Am. Soc. Metals **46**, 1,331 (1954).
[2] John Vajda and Paul E. Busby, Effect of composition on transverse properties of slack-quenched steel, Trans. Am. Soc. Metals **47**, 408 (1955).
[3] Metals Handbook, American Society for Metals, Cleveland, 500 (1948).
[4] Tentative method of end-quench test for hardenability of steel (A255–48T), Am. Soc. Testing Materials, Standards, 636 (1955).

WASHINGTON, April 8, 1957.

Journal of Research of the National Bureau of Standards Vol. 59, No. 4, October 1957 Research Paper 2800

Synthesis of C^{14}-Labeled L-Sorbose and L-Ascorbic Acid[1]

H. L. Frush and H. S. Isbell

A method is presented for preparing C^{14}-labeled L-ascorbic acid (vitamin C) from labeled barium D-gluconate or D-glucose. The process is adapted from the commercial synthesis of vitamin C through sorbitol, L-sorbose and potassium di-*O*-isopropylidene-2-*keto*-L-gulonate. In the cyanohydrin synthesis of labeled D-glucose, barium D-gluconate is used as an intermediate. For preparing labeled L-ascorbic acid, the gluconate is converted to the lactone. This is efficiently reduced, by means of sodium borohydride, directly to sorbitol, obviating the intermediate preparation of D-glucose.

If labeled D-glucose is more readily available than the corresponding gluconic acid (as for instance D-glucose-6-C^{14} or randomly labeled D-glucose), the sugar is reduced to sorbitol by the sodium borohydride method; the yield is nearly quantitative.

In a preparation of L-ascorbic acid-6-C^{14} from barium D-gluconate-1-C^{14} the yield was 41.5 percent, based on the gluconate, or 67.8 percent, based on the intermediate L-sorbose. A mixture of Methyl Cellosolve, ethylene dichloride, and hydrogen chloride was found to be effective in converting potassium di-*O*-isopropylidene-2-*keto*-L-gulonate to L-ascorbic acid.

1. Introduction

Carbon-14-labeled L-ascorbic acid (vitamin C) is a useful tool for studying many problems in biology and medicine. Before the present work, 1-labeled L-ascorbic acid had been prepared from L-xylosone through the addition of C^{14}-labeled cyanide [1],[2] and randomly labeled L-ascorbic acid had been prepared from randomly labeled D-glucose [2] by the process of Reichstein and Grüssner [3]. In the present commercial process for synthesizing L-ascorbic acid, the following substances are successively prepared from D-glucose: Sorbitol; L-sorbose; di-*O*-isopropylidene-L-sorbose; potassium di-*O*-isopropylidene-2-*keto*-L-gulonate; and finally L-ascorbic acid. The process differs from that of Reichstein and Grüssner chiefly in the manner of converting L-sorbose to diacetone L-sorbose, and potassium di-*O*-isopropylidene-2-*keto*-L-gulonate to L-ascorbic acid [4, 5]. Because D-glucose or D-gluconic acid labeled in position 1, 2, or 6 is now readily available, it is possible to prepare L-ascorbic acid labeled respectively in position 6, 5, or 1. This paper reports improved procedures, adapted from the commercial process, for preparing C^{14}-labeled L-ascorbic acid.

2. Discussion of Experimental Methods

The Bureau has developed efficient methods for converting barium carbonate-C^{14} to sodium cyanide-C^{14} [6]; for successively preparing, from sodium cyanide-C^{14}, C^{14}-labeled cyanohydrins, aldonic acids, and lactones [7]; for reducing lactones directly to glycitols [8]; and for preparing D-glucose-6-C^{14} [9].

The method reported here for preparing labeled L-ascorbic acid starts with labeled D-glucose, or barium D-gluconate (which is converted to D-glucono-δ-lactone). After reduction of the sugar,[3] or lactone, with sodium borohydride, the resulting crude sorbitol is not crystallized, but oxidized to L-sorbose with *Acetobacter suboxydans* [11, 12]. Preliminary study of this oxidation with nonradioactive sorbitol showed a maximum yield of L-sorbose of 95 percent in 40 hr. The yield obtained with crude sorbitol-6-C^{14}, however, was lower (69%), and the fermentation proceeded more slowly than that of nonradioactive sorbitol used as a control.

The next intermediate, 2,3-4,6-di-*O*-isopropylidene-L-sorbose-6-C^{14}, was prepared from L-sorbose-6-C^{14}, acetone, and sulfuric acid under conditions previously reported by Slobodin [4]. The di-*O*-isopropylidene-L-sorbose, when oxidized with potassium permanganate in alkaline solution [3], gave crude potassium di-*O*-isopropylidene-2-*keto*-L-gulonate in high yield. This intermediate, treated with a mixture of hydrochloric acid, methanol, and chloroform, under conditions similar to those described by Elger [5], yielded about 50 percent of L-ascorbic acid-6-C^{14}. However, the reaction mixture turned dark and formed a small amount of humuslike material. To improve the last step, other solvents and conditions were studied. It was found that mixtures of hydrochloric acid and Methyl Cellosolve (ethylene glycol monomethyl ether) considerably improve the yield of L-ascorbic acid, which crystallizes readily following the addition of ethylene dichloride.

[1] Part of a project on the development of methods for the synthesis of radioactive carbohydrates sponsored by the Division of Research, Atomic Energy Commission.

[2] Figures in brackets indicate the literature references at the end of this paper.

[3] Sodium borohydride reduces sugars almost quantitatively to glycitols in alkaline solution [10].

The accompanying diagram gives a summary of the steps in the synthesis. The over-all yield of L-ascorbic acid-6-C^{14} from barium D-gluconate-1-C^{14} was 41.5 percent, and from L-sorbose-6-C^{14}, 67.8 percent.

Barium D-gluconate-1-C^{14}
↓ (89.2%)
Sorbitol-6-C^{14} (in solution)
(D-Glucitol-1-C^{14})
↓ (68.7%)
L-Sorbose-6-C^{14}
↓ (84.9%)
Di-*O*-isopropylidene-L-sorbose-6-C^{14}
↓ (94.5%)
Potassium di-*O*-isopropylidene-2-*keto*-L-gulonate-6-C^{14}
↓ (84.5%)
L-Ascorbic acid-6-C^{14}
(over-all yield 41.5%)

3. Experimental Procedures

3.1. Sorbitol-6-C^{14} (or D-Glucitol-1-C^{14})

Sorbitol-6-C^{14} was obtained by sodium borohydride reduction of D-glucono-δ-lactone-1-C^{14} [8]. The process began with barium D-gluconate-1-C^{14} and was conducted in the following manner: A 1.38-g quantity of barium D-gluconate-1-C^{14} having an activity of 1,756 microcuries (μc) [4] was dissolved in water and passed through a column containing 20 ml of cation exchange resin.[5] The combined effluent and washings were concentrated under vacuum in a 100-ml flask to a thin sirup, which was lactonized by alternate addition of Methyl Cellosolve and evaporation in a current of air. After 8 or 10 evaporations over the course of three weeks, lactonization was complete and the product appeared to be entirely crystalline. The flask was then cooled in an ice bath, and 50 ml of 0.05-*M* aqueous boric acid and 10 ml of Amberlite IR 120 resin were added. With efficient mechanical stirring, 50 ml of freshly prepared 0.3-*M* sodium borohydride was added during 5 min. Stirring was continued for 30 min, and a second 50-ml portion of the borohydride solution was added as before. After an additional 30 min, 10 ml of 1-*N* sodium hydroxide was added, and the mixture was stored overnight at about 5° C. It was then passed through a column containing 100 ml of cation exchange resin. The effluent and washings were concentrated in a rotating vacuum still at 30° C to a volume of about 10 ml.

In order to remove boric acid as volatile methyl borate, 50 ml of methanol was added and the solution was evaporated under reduced pressure. This procedure was repeated, and after five additions of methanol, each followed by evaporation to a sirup, a test for boric acid with acidified turmeric paper was negative. The material was dissolved in water, and aqueous sodium hydroxide was added until a permanent pink color was obtained with phenolphthalein. The solution was then passed through a column containing 30 ml of mixed cation (see footnote 5) and anion [6] exchange resin. The effluent and wash liquor were concentrated in a vacuum to a volume of 20 ml. An assay of the solution by a direct count of a portion in formamide [13] showed 1,566 μc of activity. Hence, 89.2 percent of the barium D-gluconate-1-C^{14} had been reduced, after conversion to the lactone. The product, sorbitol-6-C^{14}, was not crystallized, but used directly for the preparation of L-sorbose-6-C^{14}.

3.2. L-Sorbose-6-C^{14}

To study the oxidation of sorbitol to L-sorbose, a solution was prepared from 3.64 g of nonradioactive sorbitol, 1.0 g of yeast extract, 0.6 g of potassium dihydrogen phosphate and 200 ml of water. Aliquots (25 ml) were placed in 125-ml Erlenmeyer flasks and sterilized for 15 min at a steam pressure of 15 lb. Each flask was then inoculated with 5 drops of a previously prepared inoculum of *Acetobacter suboxydans*, and incubated at 30° C. (The inoculum was prepared by growth, at 30° C for 45 hr, of a fresh culture of *Acetobacter suboxydans* on a medium containing 2 g of sorbitol, 0.2 g of yeast extract, and 40 ml of water.)

At intervals, one of the flasks was removed from the incubator, and the volume of solution was adjusted to 25 ml at 20° C; 0.2 g of Filtercel (diatomaceous earth) was added, and the mixture was filtered through a dry paper into a 2-dm saccharimeter tube. The optical rotation was measured, and the yield of sorbose was calculated from the specific rotation of L-sorbose (−43.4°). Calculated yields of 23.3, 95.7, 94.4, 92.1, 88.1, and 83.0 percent were obtained after incubation times of 20, 40, 45, 49, 66, and 94 hr, respectively. Thus, under the conditions used, L-sorbose reached a maximum in about 40 hr.

For the preparation of L-sorbose-6-C^{14}, the solution described in section 3.1, containing approximately 4.2 mM of sorbitol-6-C^{14}, and having an activity of 1,566 μc was divided into two equal parts. Each of these was transferred, with sufficient water to give a volume of 25 ml, to a 125-ml Erlenmeyer flask containing 125 mg of yeast extract and 75 mg of potassium dihydrogen phosphate. The mixture was sterilized at 15 lb of pressure for 15 min and then incubated at 30° C with five drops of a previously prepared inoculum of *Acetobacter suboxydans*. After 72 hr, the fermentation mixtures had approximately the same amount of turbidity as that observed for control experiments with nonradioactive sorbitol at the point of maximum sorbose content (40 hr). At this point the contents of the two flasks were combined and treated with 5 ml of 20-percent aqueous zinc sulfate, followed by sufficient aqueous barium hydroxide to give a blue color

[4] The work described in sections 3.1–3.2, 3.3, and 3.4–3.5, was carried out with materials having specific activities, respectively, of 370, 250, and 60 μc/mM.
[5] Amberlite IR 120–H, Rohm and Haas Co., Philadelphia, Pa.
[6] Duolite A4, Chemical Process Co., Redwood City, Calif.

with bromothymol blue. After the addition of 0.5 *g* of Filtercel, the solution was filtered, and the precipitate was washed thoroughly, and then discarded. The filtrate was passed slowly through a column containing 35 ml of a mixture of cation and anion exchange resin; a conductivity test of the combined solution and washings showed nearly complete absence of ionic impurities.[7] The product was concentrated under reduced pressure to a thick sirup, diluted with about 1 ml of methanol, and treated with 2-propanol to the point of incipient turbidity. It was then seeded with L-sorbose and allowed to stand for several days, after which a crop of crystalline L-sorbose-6-C^{14} was separated; the recrystallized product had an activity of 934 μc. An additional 142 μc of L-sorbose-6-C^{14} was separated from the mother liquor by use of a total of 500 mg of carrier L-sorbose in three portions. The total radioactivity, 1,076 μc, was 68.7 percent of that of the crude sorbitol-6-C^{14}.

3.3. Di-*O*-Isopropylidene-L-sorbose-6-C^{14}

One ml of concentrated sulfuric acid was added dropwise to 25 ml of dry acetone at 0° C. Twenty milliliters of this solution was placed in a 200-ml round-bottomed flask, together with 540 mg (3mM) of finely powdered L-sorbose-6-C^{14} having an activity of 777 μc (see footnote 4). The mixture was stoppered, and shaken mechanically until all of the L-sorbose had dissolved (1 to 2 hr). The pale yellow solution was placed first in a refrigerator at 0° C for 18 hr, and then in a freezer at −20° C for 24 hr. The cold material was diluted with a solution of 3 g of potassium carbonate in 25 ml of ice water, followed by 100 ml of acetone. Precipitated potassium sulfate was removed by filtration, washed with acetone, and discarded. The acetone solution was concentrated on a rotary vacuum still nearly to dryness, and the residue was carefully extracted in a hot water bath with successive 50-ml portions of heptane. The extracts were removed by a vacuum siphon arrangement to a 200-ml round-bottomed flask. Following the fourth extraction, the residue was dissolved in acetone, and the solvent was evaporated as completely as possible under vacuum. After one additional extraction of the residue, the combined heptane extracts were concentrated under vacuum to a sirup, which crystallized when seeded with di-*O*-isopropylidene-L-sorbose. The material, when recrystallized from hot heptane, had an activity of 611 μc. By use of 500 mg of nonradioactive di-*O*-isopropylidene-L-sorbose, material having an additional 49μc of activity was recovered from the mother liquor, to give a total radiochemical yield of 84.9 percent.

3.4. Potassium Di-*O*-isopropylidene-2-*keto*-L-gulonate-6-C^{14}

A solution containing 500 mg of di-*O*-isopropylidene-L-sorbose-6-C^{14} (having an activity of 128 μc, see footnote 4) and 0.225 g of potassium hydroxide in 5 ml of water was cooled to 0° C, and a solution of 0.43 g of potassium permanganate in 10 ml of water was added dropwise, with shaking, over the course of ½ hr. Then the mixture was mechanically shaken for 4 hr. At the end of this time it was heated to 50° C to coagulate the manganese dioxide, and 2 ml of ethanol was added to remove unreacted permanganate. The solution was filtered, and the residue washed with water and discarded; the filtrate was saturated with carbon dioxide and freeze-dried. To recover any remaining di-*O*-isopropylidene-L-sorbose, the dry residue was extracted 4 times with 10-ml portions of ether. However, the ether extract contained less than 1 μc, and hence was discarded. The main product, containing 121 μc of carbon-14, was used without purification for the production of ascorbic acid.

3.5. Conversion of Potassium Di-*O*-isopropylidene-2-*keto*-L-gulonate-6-C^{14} to L-Ascorbic Acid-6-C^{14} by Hydrogen Chloride in Methanol

The solution of crude potassium di-*O*-isopropylidene-2-*keto*-L-gulonate-6-C^{14} (2.0 mM having an activity of 121 μc) was passed through a column containing 10 ml of cation exchange resin. The effluent was concentrated under vacuum to a sirup, which was transferred with a little ethanol to a 10-ml glass ampoule. The sirup was then dehydrated by the repeated addition and evaporation of absolute ethanol, and finally was dissolved in 0.2 ml of methanol containing 20 percent of hydrogen chloride. After the addition of 2 ml of chloroform, the ampoule was sealed and stored at room temperature. In the course of 3 weeks, a crop of L-ascorbic acid-6-C^{14} crystallized from solution; the crystals were separated and washed with acetic acid. After recrystallization from glacial acetic acid with the addition of chloroform to the point of incipient turbidity, a crop of L-ascorbic acid-6-C^{14} having an activity of 71 μc was obtained. The dark-colored mother liquors were diluted with an equal volume of toluene and concentrated in a rotary vacuum still to a thick sirup. By use of 400 mg of L-ascorbic acid as carrier, and cocrystallization from acetic acid, material having an additional 20 μc of radioactivity was obtained, to give a radiochemical yield of 75.2 percent.

3.6. Conversion of Potassium Di-*O*-isopropylidene-2-*keto*-L-gulonate to L-Ascorbic Acid by Hydrogen Chloride in Methyl Cellosolve

To study the conversion step, 1-mM samples of potassium di-*O*-isopropylidene-2-*keto*-L-gulonate in Methyl Cellosolve-hydrogen chloride mixtures were stored at 40° C under nitrogen in sealed glass tubes, and the yield of L-ascorbic acid was determined by titration with iodine in acid solution. The results are reported in table 1. Relatively little color developed, and the yields of L-ascorbic acid were somewhat higher than those obtained in comparable experiments with the conventional methanol-hydrogen chloride mixtures.

[7] Test made with Barnstead Purity Meter, Barnstead Still and Sterilizer Co., Inc., Boston, Mass.

In view of the results given in table 1, the following procedure was selected for converting the *keto*-acid to L-ascorbic acid: A 2-mM sample of potassium di-*O*-isopropylidene-2-*keto*-L-gulonate in aqueous solution was passed through a column containing 10 ml of ice-cold cation exchange resin. The effluent was concentrated under vacuum to 10 ml and was then freeze-dried. The residue was dissolved in a mixture of 1 ml of concentrated hydrochloric acid and 7.5 ml of Methyl Cellosolve. The solution was diluted with 15 ml of Methyl Cellosolve and stored under nitrogen at 40° for 1 week. Then it was concentrated under vacuum to about 1 ml, diluted with 5 ml of Methyl Cellosolve, reconcentrated to 1 ml, and diluted with 5 ml of ethylene dichloride. In the course of 24 hr, a crop of crystalline L-ascorbic acid formed. The mother liquor was separated, and the product was washed with acetone. It was recrystallized by dissolving it in Methyl Cellosolve, concentrating the solution under vacuum to a low volume, and adding 5 ml of ethylene dichloride. The recrystallized product weighed 265 mg; titration with iodine showed the presence of 1.49 mM of L-ascorbic acid. The mother liquor contained 0.20 mM by analysis, making the total yield in the last step 1.69 mM, or 84.5 percent.

TABLE 1. *Yields of ascorbic acid from potassium di-O-isopropylidene-2-keto-L-gulonate in Methyl Cellosolve-hydrogen chloride mixtures*

Rearrangement mixture [a]		Temperature	Reaction time	Yield of ascorbic acid [b]
Methyl Cellosolve	Concentrated HCl			
ml	*ml*	*° C*	*hr*	*%*
4	0.4	40	140	54
			304	80
			520	82.8
4	1.2	40	67	71
			140	84
			304	82
8	0.4	40	140	48
			304	76
			520	79.2

[a] One millimole of potassium di-*O*-isopropylidene-2-*keto*-L-gulonate plus the materials listed below.
[b] Calculated from titration of the product with iodine in acid solution.

The authors are grateful to Galen Wampler for assistance in the experimental work.

4. References

[1] J. J. Burns and C. G. King, Science **111**, 257 (1950); L. L. Salomon, J. J. Burns, and C. G. King, J. Am. Chem. Soc. **74**, 5161 (1952).
[2] A. A. Bothner-By, M. Gibbs, and R. C. Anderson, Science **112,** 363 (1950).
[3] T. Reichstein and A. Grüssner, Helv. Chim. Acta **17,** 311 (1934).
[4] Ya. M. Slobodin, J. Gen. Chem. (U.S.S.R.), **17,** 485 (1947); C. A. **42,** 871 (1948).
[5] F. Elger, Festschr. Emil Barell **1936,** 229–37; C. A. **31,** 2585 (1937); U. S. Patent 2,129,317 (1938).
[6] J. D. Moyer and H. S. Isbell, Anal. Chem. **29,** 393 (1957).
[7] H. S. Isbell, U. S. Patent 2,606,918 (1952); H. S. Isbell, J. V. Karabinos, H. L. Frush, N. B. Holt, A. Schwebel, and T. T. Galkowski, J. Research NBS **48,** 163 (1952) RP2301; H. S. Isbell, H. L. Frush, and R. Schaffer, *ibid.* **54,** 201 (1955) RP2581.
[8] H. L. Frush and H. S. Isbell, J. Am. Chem. Soc. **78,** 2844 (1956).
[9] R. Schaffer and H. S. Isbell, J. Research NBS **56,** 191 (1956) RP2667.
[10] M. Abdel-Akher, J. K. Hamilton, and F. Smith, J. Am. Chem. Soc. **73,** 4691 (1951); B. Lindberg and A. Misiorny, Svensk Papperstidn. **55,** 13 (1952); C. A. **46,** 7942 (1952); P. S. Skell and J. G. Crist, Nature **173,** 401 (1954).
[11] P. A. Wells, J. J. Stubbs, L. B. Lockwood, and E. L. Roe, Ind. Eng. Chem. **29,** 1385 (1937).
[12] H. S. Isbell and J. V. Karabinos, J. Research NBS **48,** 438 (1952) RP2334.
[13] A. Schwebel, H. S. Isbell, and J. D. Moyer, J. Research NBS **53,** 221 (1954) RP2537.

WASHINGTON, April 18, 1957.

U. S. GOVERNMENT PRINTING OFFICE: 1957

THE NATIONAL BUREAU OF STANDARDS

The scope of activities of the National Bureau of Standards at its headquarters in Washington, D. C., and its major field laboratories in Boulder, Colorado, is suggested in the following listing of the divisions and sections engaged in technical work. In general, each section carries out specialized research, development, and engineering in the field indicated by its title. A brief description of the activities, and of the resultant publications, appears on the inside of the front cover.

WASHINGTON, D. C.

Electricity and Electronics. Resistance and Reactance. Electron Devices. Electrical Instruments. Magnetic Measurements. Dielectrics. Engineering Electronics. Electronic Instrumentation. Electrochemistry.

Optics and Metrology. Photometry and Colorimetry. Optical Instruments. Photographic Technology. Length. Engineering Metrology.

Heat. Temperature Physics. Thermodynamics. Cryogenic Physics. Rheology. Engine Fuels. Free Radicals Research.

Atomic and Radiation Physics. Spectroscopy. Radiometry. Mass Spectrometry. Solid State Physics. Electron Physics. Atomic Physics. Neutron Physics. Nuclear Physics. Radioactivity. X-rays. Betatron. Nucleonic Instrumentation. Radiological Equipment. AEC Radiation Instruments.

Chemistry. Organic Coatings. Surface Chemistry. Organic Chemistry. Analytical Chemistry. Inorganic Chemistry. Electrodeposition. Molecular Structure and Properties of Gases. Physical Chemistry. Thermochemistry. Spectrochemistry. Pure Substances.

Mechanics. Sound. Mechanical Instruments. Fluid Mechanics. Engineering Mechanics. Mass and Scale. Capacity, Density, and Fluid Meters. Combustion Controls.

Organic and Fibrous Materials. Rubber. Textiles. Paper. Leather. Testing and Specifications. Polymer Structure. Plastics. Dental Research.

Metallurgy. Thermal Metallurgy. Chemical Metallurgy. Mechanical Metallurgy. Corrosion. Metal Physics.

Mineral Products. Engineering Ceramics. Glass. Refractories. Enameled Metals. Concreting Materials. Constitution and Microstructure.

Building Technology. Structural Engineering. Fire Protection. Air Conditioning, Heating, and Refrigeration. Floor, Roof, and Wall Coverings. Codes and Specifications. Heat Transfer.

Applied Mathematics. Numerical Analysis. Computation. Statistical Engineering. Mathematical Physics.

Data Processing Systems. SEAC Engineering Group. Components and Techniques. Digital Circuitry. Digital Systems. Analog Systems. Application Engineering.

• Office of Basic Instrumentation.

• Office of Weights and Measures.

BOULDER, COLORADO

Cryogenic Engineering. Cryogenic Equipment. Cryogenic Processes. Properties of Materials. Gas Liquefaction.

Radio Propagation Physics. Upper Atmosphere Research. Ionospheric Research. Regular Propagation Services. Sun-Earth Relationships.

Radio Propagation Engineering. Data Reduction Instrumentation. Modulation Systems. Navigation Systems. Radio Noise. Tropospheric Measurements. Tropospheric Analysis. Radio Systems Application Engineering.

Radio Standards. High Frequency Electrical Standards. Radio Broadcast Service. High Frequency Impedance Standards. Calibration Center. Microwave Physics. Microwave Circuit Standards.

Recent Publications of the National Bureau of Standards

Journal of Research of the National Bureau of Standards. Volume 59, No. 2, August 1957 (RP2733 to RP2781 incl.). 60 cents. Annual subscription $4.00.

Technical News Bulletin, Volume 41, No. 8, August 1957. 10 cents. Annual subscription $1.00.

Basic Radio Propagation Predictions for November 1957. Three months in advance. CRPL-D 156. Issued August 1957. 10 cents. Annual subscription $1.00.

Building Materials and Structures Reports

BMS 142. Fifteen-year exposure test of porcelain enamels. 15 cents.

Circulars

C562-Supplement 1. Bibliography of research on deuterium and tritium compounds, 1953 and 1954. 25 cents.

Available from the Superintendent of Documents, U. S. Government Printing Office, Washington 25, D. C. (foreign postage, one-fourth additional).

UNITED STATES
GOVERNMENT PRINTING OFFICE
DIVISION OF PUBLIC DOCUMENTS
WASHINGTON 25, D. C.

OFFICIAL BUSINESS

PENALTY FOR PRIVATE USE TO AVOID PAYMENT OF POSTAGE, $300 (GPO)

Journal of Research of the National Bureau of Standards Vol. 59, No. 4 October 1957

Contents

		Page
Formulas for inverse osculatory interpolation in the complex plane. Herbert E. Salzer.	RP2792	233
An X-ray study of textural stresses in two-phase alloys. C. J. Newton and H. C. Vacher.	RP2793	239
Dissociation of 4-chloro-4′-aminodiphenylsulfone. Elizabeth E. Sager and Fleur C. Byers.	RP2794	245
Speed of sound in water by a direct method. Martin Greenspan and Carroll E. Tschiegg.	RP2795	249
Pattern of a flush-mounted microwave antenna. James R. Wait.	RP2796	255
Standards for *p*H measurements from 60° to 95° C. Vincent E. Bower and Roger G. Bates.	RP2797	261
A numerical study of Dedekind's cubic class number formula. Harvey Cohn.	RP2798	265
Impact properties of slack-quenched alloy steels. Melvin R. Meyerson and Samuel J. Rosenberg.	RP2799	273
Synthesis of C^{14}-labeled L-sorbose and L-ascorbic acid. H. L. Frush and H. S. Isbell.	RP2800	289

[A list of recent NBS publications is given on page 3 of the cover.]

For sale by the Superintendent of Documents, U. S. Government Printing Office, Washington 25, D. C. Price 60 cents (single copy). Subscription price: $4.00 a year; $1.25 additional for foreign mailing.

UNITED STATES GOVERNMENT PRINTING OFFICE, WASHINGTON : 1957